COMPUTATIONAL ELECTROMAGNETIC METHODS FOR TRANSCRANIAL MAGNETIC STIMULATION

by
Luis J. Gomez

A dissertation submitted in partial fulfillment
of the requirements for the degree of
Doctor of Philosophy
(Electrical Engineering)
in The University of Michigan
2015

Doctoral Committee:

Professor Eric Michielssen, Chair
Research Associate Professor Luis Hernandez-Garcia
Professor Kamal Sarabandi
Professor Stephan F. Taylor

To The O and The o,

ACKNOWLEDGMENTS

I would like to thank my parents and sister for putting up with me while growing up and encouraging me never to give up.

I would like to thank Professor Eric Michielssen for the guidance that he provided me throught my graduate career and for pushing me to do better work. I would like to thank Professors Luis Hernandez-Garcia, Kamal Sarabandi, and Steve Taylor for serving in my thesis committee and their contributions to this work. I would also like to thank all of my past teachers for contributing in my education. Specifically, I would like to thank Henry Zmuda and Tom Greene for encouraging me to pursue a PhD.

Thank you to my colleagues in Eric Michielssen's group: Abdulkadir Yucel, Frantishek Cajko, Pelumi Osoba, Felipe Valdez, Xi Lin, Hakan Bagci, Yang Liu and Han Guo for their friendship and help throught this time. I would also like to thank my friends and fellow students from Rad Lab: Gurkan Gok, Michael Thiel, Fikadu Dagefu, Mohammadreza F. Imani, Scott Rudolph, Victor Lee, Michael Benson, Hatim Bukhari, Waleed Alomar, Carl Pfeiffer, Sangjo Choi, Jungsuek Oh,…

During the past years at the University of Michigan I have made many friends, outside of Rad Lab, I would like to thank them all. I would also like to thank Jackie Vitaz for introducing me to yoga, it has helped me in become a more patient and focused person.

TABLE OF CONTENTS

DEDICATION ..... **ii**

ACKNOWLEDGMENTS ..... **iii**

LIST OF FIGURES ..... **vii**

LIST OF TABLES ..... **xii**

CHAPTER 1 Introduction **1**

1.1 Background 1

1.2 TMS Coil Designs 1

1.3 Uncertainty Quantification of TMS 2

1.4 Fast direct solver for TMS 3

1.5 New integral equation formulation for TMS 4

CHAPTER 2 Numerical Analysis and Design of Single-Source Multi-Coil TMS for Deep and Focused Brain Stimulation **6**

2.1 Formulation 9

2.1.1 Design of Pareto-Optimal Multi-Channel Arrays 9

2.1.1.1 Problem Definition 9

2.1.1.2 Genetic Algorithm for Finding $\mathbf{I}^{\mathrm{opt}}(d)$ 11

2.1.1.3 Fast Computation of Fields Due to Prescribed Coil Currents 13

2.1.2 Conversion of Multi-Channel Array to Single-Channel Array 15

2.2 Results 16

2.2.1 Multi-Channel Designs For Three-Sphere Head Model 18

2.2.2 Multi-Channel Designs For MRI-Derived Head Model 24

2.3 Conclusions 32

CHAPTER 3 Uncertainty Quantification in Transcranial Magnetic Stimulation via High Dimensional Model Representation Technique **34**

3.1 Introduction 34

3.2 Formulation 38

3.2.1 The HDMR Technique: 39

3.2.2 The Iterative HDMR Technique: 42
3.2.3 The Quasi-Static FD Simulator 44
3.3 Numerical results and discussion 44
3.3.1 Three-Sphere Head Model 45
3.3.2 MRI-Derived Realistic Head Model 48
3.4 Conclusion 59
CHAPTER 4 Fast Finite-Difference Direct Solver for Real-Time Simulation of Transcranial Magnetic Stimulation 62
4.1 Introduction 62
4.2 Formulation 64
4.2.1 Finite Difference (FD) Scheme 64
4.2.2 Multi Frontal Approach 66
4.2.2.1 Domain Decomposition 66
4.2.2.2 LU-Factorization 68
4.2.3 Compression by $\mathcal{H}$-matrices 74
4.2.4 Assymptotic Complexity estimates $\mathcal{H}$-matrices 76
4.2.5 Implementation Details 77
4.3 Application of the Fast Direct Solver to TMS 78
4.3.1 Benchmark Tests 78
4.3.2 TMS Simulation Example 83
4.3.3 Real Time Coil Positioning 86
4.3.4 Concluding Remarks 88
CHAPTER 5 Low-frequency Stable Internally Combined Volume-Surface Integral Equation for High-Contrast Scatterers 90
5.1 Introduction 90
5.2 Formulation 92
5.2.1 Background 92
5.2.2 Discrete Formulation 95
5.3 Results and Discussions 98
5.4 Conclusions 101
CHAPTER 6 3D Internally Combined Volume-Surface Integral Equation 102
6.1 Introduction 102
6.2 Formulation 102
6.2.1 Background 102
6.2.2 Discrete Formulation 105
6.3 Results and Discussions 107
6.3.1 High-Contrast/Low-Frequency Layered Sphere 107
6.3.2 MRI Derived Head Model 109
6.4 Conclusions 113

CHAPTER 7 Conclusions and Future Work 114
7.1 Summary 114
7.2 Future Work 115
7.3 Contributions 116
APPENDIX A Internally Combined Volume-Surface Integral Equation for Plasma Scatterers 119
A.1 Introduction 119
A.2 Formulation 120
A.3 Results and Discussions 121
A.4 Conclusions 126
REFERENCES 127

LIST OF FIGURES

Figure 2.1 Popular TMS coils: (a) Figure-8 coil, (b) Magstim BC-70 (commercial figure-8 coil), (c) Hesed-coil, and (d) Square Multi-channel array. 7

Figure 2.2 Conversion from a multi-channel array, driven with ...., to a single-channel array: (a) The initial multi-channel configuration. (b) New equivalent design consisting of multiple coils each containing multiple circular windings and an inner winding and with each element driven with an identical current . I_{sc} . (c) Final design with all the coil elements connected in series by a feed-network that during operation negligibly contributes to the stimulating field; this is done by placing elements, which have currents of opposing polarities close to each other. 9

Figure 2.3 Three-sphere head model. (a) The array is placed 10 mm above the scalp and centered about the target column (z-axis). (b) The vertex of the figure-8 coil is on the target column at a height that varies between the 10 mm to 30 mm above the head; to find $d_{F-8}^{\max}(v)$ we allow both the radius (r) and angle (θ) to vary between 15mm to 30 mm and 0 to 180 degrees. Three-sphere head model. (a) The array is placed 10 mm above the scalp and centered about the target column (z-axis). (b) The vertex of the figure-8 coil is on the target column at a height that varies between the 10 mm to 30 mm above the head; to find $d_{F-8}^{\max}(v)$ we allow both the radius (r) and angle (θ) to vary between 15mm to 30 mm and 0 to 180 degrees. 17

Figure 2.4 Largest depth that can be reached for a given excitation volume by multi-channel arrays ($d^{\max}(v)$) and figure-8 coils ($d_{F-8}^{\max}(v)$). (a-f) Each have individual curves for each array with different number of coils N_c and each individual panel has results for arrays with coils of radius $r = 4,\ 6,\ 8,\ 10,\ 14,\ \text{and}\ 18\ \text{mm}$, respectively. 19

Figure 2.5 Largest depth that can be reached for a given excitation volume by multi-channel arrays ($d^{\max}(v)$) and figure-8 coils ($d_{F-8}^{\max}(v)$). (a-f) Each have individual curves for each array with different N_c and r but the same A and each individual has arrays with $A = 48^2,\ 64^2,\ 80^2,\ 96^2,\ 120^2,\ \text{and}\ 160^2\ \text{mm}^2$, respectively. 20

Figure 2.6 (a) The magnitude of the electric field $|\mathbf{E}(\mathbf{r})|$ produced inside the stimulated volume by a coil array with 100 coils of 10 mm radius and driven with currents optimized for a penetration depth of 24 mm (i.e., driven with $\mathbf{I}^{\text{opt}}(d = 24\,\text{mm})$). (b) The magnitude

of the electric field $|\mathbf{E}(\mathbf{r})|$ produced inside the stimulated volume by a figure-8 coil of 25 mm radius also optimized for a penetration depth of 24 mm. 21

Figure 2.7 Total current required by each array driven with currents optimized for each penetration depth $\mathbf{I}^{\text{opt}}(d)$ penetration depth (i.e., $\|\mathbf{I}^{\text{opt}}(d)\|$), (a-f) Each have individual curves for each array with different number of coils N_c and each individual panel has results for arrays with coils of radius $r = 4,\ 6,\ 8,\ 10,\ 14,\ \text{and}\ 18\ \text{mm}$, respectively. 23

Figure 2.8 Conductivity model of the head derived from an MRI image. The field of view was $231 \times 261 \times 219\ \text{mm}$. The conductivity of tissue ranged from 3.9×10^{-3} to 1.67 S/m. The array was placed 10 mm above the head. 25

Figure 2.9 Penetration depth achieved as a function of excitation volume ($d(v)$) by the multi-channel arrays and figure-8 coils for targeting inside the three-sphere head. (a) Results obtained for targeting inside the MRI-derived head. (b) Results obtained for targeting inside free-space region. Note that in both cases, achieving a penetration depth beyond 27 and 21 mm, respectively, required exceeding the safety threshold. 26

Figure 2.10 Largest depth that can be reached for a given excitation volume by multi-channel arrays ($d^{\max}(v)$) and figure-8 coils ($d_{F-8}^{\max}(v)$). (a-f) Each have individual curves for each array with different number of coils N_c and each individual panel has results for arrays with coils of radius $r = 4,\ 6,\ 8,\ 10,\ 14,\ \text{and}\ 18\ \text{mm}$, respectively. 27

Figure 2.11 Largest depth that can be reached for a given excitation volume by multi-channel arrays ($d^{\max}(v)$) and figure-8 coils ($d_{F-8}^{\max}(v)$). (a-f) Each have individual curves for each array with different N_c and r but the same A and each individual has arrays with $A = 48^2,\ 64^2,\ 80^2,\ 96^2,\ 120^2,\ \text{and}\ 160^2\ \text{mm}^2$, respectively. 28

Figure 2.12 Total current required by each array driven with currents optimized for each penetration depth $\mathbf{I}^{\text{opt}}(d)$ penetration depth (i.e., $\|\mathbf{I}^{\text{opt}}(d)\|$), (a-f) Each have individual curves for each array with different number of coils N_c and each individual panel has results for arrays with coils of radius $r = 4,\ 6,\ 8,\ 10,\ 14,\ \text{and}\ 18\ \text{mm}$, respectively.Single Channel Conversion 30

Figure 2.13 Largest depth that can be reached for a given excitation volume by multi-channel arrays ($d^{\max}(v)$), single-channel arrays ($d_{sc}(v)$) and figure-8 coils ($d_{F-8}^{\max}(v)$) 31

Figure 2.14 Largest depth that can be reached for a given excitation volume by multi-channel arrays ($d^{\max}(v)$), single-cannel arrays without inner loop ($d_{sc}(v)$) and figure-8 coils ($d_{F-8}^{\max}(v)$) 32

Figure 3.1 (a) Three-sphere head model with the Figure-8 coil positioned 1 cm above the head and centered about the z-axis. (b) The statistics of E-fields' magnitudes are obtained on a Cartesian grid (indicated with red points on a green square plane in top view). 46

Figure 3.2 The statistical moments of the E-fields' magnitudes on points selected on a Cartesian grid: (a) the means and (b) standard deviations of $V_n(\mathbf{x})$, (c) the means and (d) standard deviations of $V_n(\dot{\mathbf{x}})$, and (e) the means and (f) standard deviations of $V_n(\ddot{\mathbf{x}})$. .. 47

Figure 3.3 Realistic head model generation procedure: (i) Conductivity values are assigned to the segmented images of the skin (green) CSF (yellow), skull (gray), WM (red), and GM (blue). (ii) The WM and GM are shrunk and the displaced volume is replaced with CSF. (iii) The images are combined to generate an MRI-derived head model..... 50

Figure 3.4 The configuration of Medtronic MC-B70 Figure-8 coil (P/N 9790). 50

Figure 3.5 The coil is positioned along x' and y' directions defined along $\hat{\mathbf{x}}'$ and $\hat{\mathbf{y}}'$ unit vectors in local coordinate system. The coil is rotated with θ angle defined between the line connecting the centers of wings (indicated with dotted red line) and $\hat{\mathbf{x}}'$ unit vector. 51

Figure 3.6 The statistics of E-fields' magnitudes are obtained at centers of voxels inside a targeted hexahedral region (indicated as the red region in an MRI-derived head model); each voxel has GM inside. The red dot on targeted region indicates targeted point. 52

Figure 3.7 The statistical moments of the E-fields' magnitudes at centers of voxels: (a) the means and (b) standard deviations of $V_n(\mathbf{x})$, (c) the means and (d) standard deviations of $V_n(\dot{\mathbf{x}})$, and (e) the means and (f) standard deviations of $V_n(\ddot{\mathbf{x}})$. The red dot indicates the targeted point..... 53

Figure 3.8 The standard deviations of (a) $V_n(\dot{\mathbf{x}})$, (b) $V_n(\ddot{\mathbf{x}})$, (c) $V_n(\dddot{\mathbf{x}})$, and (d) $V_n(\ddddot{\mathbf{x}})$. The red dot indicates the targeted point. 55

Figure 3.9 (a) The coronal slice (depicted by the purple transparent plane) passing through the cortical region. The standard deviations of (b) $V_n(\dot{\mathbf{x}})$, (c) $V_n(\ddot{\mathbf{x}})$, and (d) $V_n(\dddot{\mathbf{x}})$..... 57

Figure 3.10 The E-field distribution on stimulated region when (a) $C_x = -1.0\,\text{cm}$, (b) $C_x = 1.0\,\text{cm}$, (c) $C_y = -1.0\,\text{cm}$, (d) $C_y = 1.0\,\text{cm}$, (e) $\theta = 0°$, (f) $\theta = 90°$,(g) $sf = 0.0$, and (h) $sf = 0.1$. The red dot indicates the targeted point..... 58

Figure 4.1 Domain decomposition of a $2P \times 2P \times 2P$ domain by geometric bisections. 67

Figure 4.2 Tree representation $T(\Omega)$ of the domain decomposition of a $2P \times 2P \times 2P$. There is a vertex for each subdomain and edges represent inheritance relations. At the k-th level there are $nd(k) = 2^k$ vertices and the depth is $K+1 = 4$. 67

Figure 4.3 Depiction of a generic cluster Γ_j^K. The inner and boundary nodes of a cluster lie on the red and blue regions, respectively. 68

Figure 4.4 Clusters for a $2P \times 2P \times 2P$ domain. The inner and boundary nodes of a cluster lie on the red and blue regions, respectively. 72

Figure 4.5 Storage memory for the factorized matrix..... 79

Figure 4.6 Performance of the fast direct solver on a single CPU. Factorization time (squares) and solution time (triangles). Lines show the expected asymptotic behavior... 80

Figure 4.7 Compression ratio of the factorized LU decomposition as a function of the domain size. 81

Figure 4.8 (a) Compression ratio and (b) rank distribution of matrix A_{ii}^{-1} of the node T_{10} for the air-filled domain of size 128x64x64, P=4 and threshold 10^{-6}. The largest rank is 24. The red blocks in the rank distribution represent matrices in the full format..... 81

Figure 4.9 Relative residual error and solution error. 83

Figure 4.10 Localization and orientation of the figure-8 coil above the head. Coil diameter, coil separation and distance from the head displayed. The dashed line shows position of the axial plane in the results..... 84

Figure 4.11 Convergence of the iterative solver with a block-diagonal preconditioner... 85

Figure 4.12 Conductivity: (a) transverse plane (b) coronal plane (c) sagittal plane. Magnitude of the total electric field inside the head normalized with respect to the highest value in the head: (d) transverse plane (e) coronal plane (f) sagittal plane. Absolute error of the total electric field inside the head: (g) transverse plane (h) coronal plane (i) sagittal plane..... 86

Figure 4.13 Electric field distribution in the axial plane crossing the target point (31 mm below the top of the head). The white circles represent a projection of the figure-8 coil into the plane..... 87

Figure 4.14 Distance between the electric field maxima and the single target for different coil locations. The local directions are defined in Fig. 4.10. 88

Figure 5.1 (a) Inhomogeneous dielectric body $\mathbf{\Omega}$ with electric permittivity $\epsilon(\boldsymbol{\rho})$, surrounded by a medium with electrical permittivity ϵ_b, and illuminated a time-harmonic electric field $\mathbf{E}^{\mathbf{inc}}(\boldsymbol{\rho})$. (b) Equivalent scenario where the whole space is replaced by surface currents $\mathbf{J}^{\mathbf{s}}(\boldsymbol{\rho})$ and $\mathbf{M}^{\mathbf{s}}(\boldsymbol{\rho})$ propagating in a medium with electric permittivity ε_b. (c) Equivalent scenario where the inhomogeneous dielectric body $\mathbf{\Omega}$ is replaced by polarization volumetric current density $\mathbf{J}^{\mathbf{v}}(\boldsymbol{\rho})$, and the background permittivity is artificially raised to ε_{eff} by introducing surface currents $-\mathbf{J}^{\mathbf{s}}(\boldsymbol{\rho})$ and $-\mathbf{M}^{\mathbf{s}}(\boldsymbol{\rho})$..... 92

Figure 5.2 (a) Condition number of systems of equations as a function of electrical size (b) number of iterations for TFQMR procedure to reach a RRE of 10^{-5} as a function of electrical size (c) The relative L^2 norm error of the electric field inside the scatterer as a function of electrical size. 99

Figure 5.3 (a) Condition number of systems of equations as a function of maximum electric permittivity (b) number of iterations for TFQMR procedure to reach a RRE of 10^{-5} as a function of maximum electric permittivity (c) The relative L^2 norm error of the electric field inside the scatterer as a function of maximum electric permittivity. 100

Figure 6.1 (a) Scattering scenario (b) equivalent exterior scenario (c) equivalent interior scenario. 103

Figure 6.2 Electric field along lines crossing the center of the four layer sphere: (a) $\varepsilon_{\max} = 10\varepsilon_0$ (b) $\varepsilon_{\max} = 10^4\varepsilon_0$ (c) $\varepsilon_{\max} = 10^7\varepsilon_0$ 108

Figure 6.3 Condition number as a function of maximum electric permittivity. 109

Figure 6.4 TMS setup 109

Figure 6.5 Relative Residual history for the VIE and ICVSIE 110

Figure 6.6 Electric field (V/m) generated during TMS scenario on various planes: (a) incident field on the scalp (b) total field on the scalp (c) incident field on a coronal plane crossing the center of the coil (d) total field on a coronal plane crossing the center of the coil (e) incident field on a sagittal plane crossing the center of the coil (f) total field on a sagittal plane crossing the center of the coil 111

Figure 6.7 TMS setup: (a) side view (b) front view (c) top view 112

Figure 6.8 Relative Residual history for the VIE and ICVSIE 112

Figure 6.9 Electric field generated during TMS on various planes: (a) transverse plane (b) coronal plane (c) sagittal plane 113

Figure A.1 Analysis with different mesh densities. Number of iterations versus RREs of (a) ICVSIE, (b) Muller VSIE-D, and (c) VIE systems' solutions to reach to 10^{-8}. 123

Figure A.2 Analysis with different cylinder diameters. Number of iterations versus RREs of (a) ICVSIE, (b) Muller VSIE-D, and (c) VIE systems' solutions. 124

Figure A.3 Analysis with different cylinder diameters. The bistatic RCS of the cylinder with (a) $d=\lambda_0/4$, (b) $d=\lambda_0/2$, (c) $d=\lambda_0$, (d) $d=2\lambda_0$, and (e) $d=4\lambda_0$ obtained by Bessel series (Exact) solution, ICVSIE, Muller VSIE-D, and VIE systems' solutions. 125

Figure A.4 Analysis with different numbers of layers. Number of iterations versus RREs of (a) ICVSIE, (b) Muller VSIE-D, and (c) VIE systems' solutions. 126

LIST OF TABLES

Table 2.1 Smallest volume $v^{\min}(d)$ of all array configurations considered and $v_{F-8}^{\min}(d)$ for three-sphere head 19

Table 2.2 Tissue Conductivity values 24

Table 2.3 $v^{\min}(d)$ of all array configurations considered and $v_{F-8}^{\min}(d)$ for MRI-derived head 28

Table 3.1 The Values of a^i, b^i, and $\bar{x}^i$, $i=1,\ldots,5$ (for the Three-Sphere Head Model Scenario) 47

Table 3.2 The Values of a^i, b^i, and $\bar{x}^i$, $i=1,\ldots,9$ (for the MRI-Derived Head Model Scenario) 52

Table 3.3 The Random Variables, Their Descriptions, and the Ratios of the Standard Deviations of Induced E-fields to the Means of Induced E-fields in Three Cases. 53

Table 3.4 The Random Variables, Their Descriptions, and the Ratios of the Standard Deviations of Induced E-fields to the Means of Induced E-fields in Four Cases. 55

Table 4.1 Performance of the fast direct solver in dependence on the level of accuracy for a domain of size 64x64x64. 79

Table 4.2 Performance comparison between the sparse direct solver Pardiso and the fast direct solver (threshold 1E-6). 82

Table 5.1 Integral equation Formulations 97

Table A.1 L^2 Norm errors of quantities obtained by ICVSIE system 122

Table A.2 Number of iterations required for RRE of systems' solution to reach to 10^{-3} while the mesh density changes 123

Table A.3 Number of iterations required for RRE of systems' solution to reach to 10^{-3} while the diameter of cylinder changes 124

Table A.4 Number of iterations required for RRE of systems' solution to reach to 10^{-3} while the number of layers changes 126

CHAPTER 1
Introduction

1.1 Background

Transcranial magnetic stimulation (TMS) is a method that is used for the treatment of neurological disorders and to study brain function that involves the stimulation of neuronal tissue. In TMS, one or more coils placed near the scalp produce magnetic fields that induce electric fields and eddy-currents in the conductive brain tissue. When the spatial gradient of the electric field aligns with a nerve fiber, an action potential is generated [1, 2]. As a result, TMS enables neuroscientists to create causal links between stimulated cortical regions and observable behaviors. Furthermore, TMS is used by clinicians to activate regions of the brain for depression therapy. In this work, we have come up with new TMS coil designs and developed computational electromagnetic (CEM) tools for better analyzing the fields generated during TMS. More specifically, a framework for uncertainty quantification of TMS, real-time analysis of fields induced during TMS and a new volume-surface integral equation formulation for determining electric fields generated during TMS have been developed. Furthermore, it will be shown that the new volume-surface integral equation is not only applicable to TMS but it can also be used for analysis of fields generated inside negative permittivity scatterers.

1.2 TMS Coil Designs

Electric fields generated by current TMS coils decay and diffuse rapidly as they penetrate into the brain. As a result, they stimulate relatively large regions of tissue near

the brain's surface. Many TMS applications require stimulation of specific target regions deep in the brain while minimizing stimulation elsewhere. Creating TMS coils that produce electric fields that are both sharply focused and stimulate regions deep inside the brain has been a constant research goal [3-15].

Recently, multi-channel TMS arrays composed of many independently driven coils have been shown to deliver a more concentrated and deeply penetrating field than single coils. In chapter 2, we propose a systematic, genetic algorithm-based technique for synthesizing multi-channel arrays that minimize the volume of the excited region required to achieve a prescribed penetration depth. Numerical results show that the performance of the arrays designed via the proposed technique is vastly superior to that of existing TMS coil designs. Because multi-channel arrays are costly to build, we also propose a method to convert the multi-channel arrays into single-channel ones that can be driven by a one current source, without materially deteriorating performance.

1.3 Uncertainty Quantification of TMS

The electric field distribution generated during TMS is highly sensitive to uncertainty in the TMS setup (e.g. location and orientation of the coil relative to targeted cortical site) and uncertainty related to patient-to-patient differences (e.g. size and conductivity of individual tissue layers of the head). To ensure that the electric field distribution inside a targeted cortical region is above a given threshold, the dependency between electric fields and uncertainty in the TMS procedure should be accurately quantified.

In chapter 3, a computational framework for statistically characterizing the region stimulated by TMS is presented. For example, given probability density functions (pdfs) of the above uncertain parameters, the framework can be used to compute both the probability that a cortical region of interest is being stimulated and pdfs for the depth and volume of the stimulated region. To collect this information efficiently, the framework uses a high dimensional model representation (HDMR) technique that generates parameterized surrogate models for the electric field. Next, these surrogate models are

used in lieu of a more computationally expensive quasi-static Finite-difference electromagnetic simulator while gathering statistics of the stimulated region using a traditional Monte-Carlo method. The HDMR technique generates the surrogate models using a series of iteratively constructed component functions. The component functions pertinent to the most strongly interacting uncertain parameters are approximated via/using a multi-element probabilistic collocation method. The accuracy of proposed framework is demonstrated through the statistical characterization of the stimulated region for a TMS treatment of depression on concentric spheres and MRI-derived human head models.

1.4 Fast direct solver for TMS

Many TMS applications require precise target identification and coil placement. Modern 'neuro-navigated' stereotactic TMS systems use structural MRI images and cameras to identify the optimum coil position for TMS treatment [16, 17]. Coil positioning systems identify the location on the scalp directly over the targeted cortical site as the optimum coil placement site because commercial TMS coils (i.e. Magstim BC-70) in the absence of the head generate electric fields, or equivalently primary fields, that are strongly concentrated near the coil center. Unfortunately, the primary electric fields generated by the coil induce charges on boundaries between tissue layers. These charges generate significant "secondary" electric fields inside the head, and thus, potentially change the optimum coil placement site [18-20]. Given a model of the coil, a conductive head model and the position where the coil is located relative to the head, the total electric field generated (i.e. primary plus secondary electric field) can be accurately determined by using the finite difference (FD) [21-23] method. In FD, partial differential equations of electromagnetism are approximated by finite-differences to generate a sparse linear systems of equations in field-related quantities [22]. The solution of these systems of equations via iterative or direct solution techniques currently used require minutes, and thus, are virtually ruled out for real-time applications.

By leveraging the multifrontal approach, geometric bisection, and compressibility using hierarchical matrices, we constructed a fast direct solver for sparse matrices derived from a quasi-static finite-difference model of the fields induced during TMS. After a single factorization step, the solver is able to compute the solution of the electric field inside the head in seconds. It is thus more effective than iterative solvers, which are typically used, in frameworks that require solutions for multiple excitations. More importantly, the fast-direct solver can be used for real-time applications. We describe implementation of the solver and compare its performance when analyzing fields inside a realistic MRI derived human head model with other techniques in chapter 4.

1.5 New integral equation formulation for TMS

The human head is highly heterogenous, and at the range of frequencies of TMS (1-10KHz), it has conductivities between 0.01-1.8 S/m that result in an effective permitivities as large as 10^7 times the free space permittivity. As a result, integral equation-based tools for analyzing TMS fields must be able to analyze fields inside highly-heterogenous media having arbitrarily high permitivities, and be low-frequency stable. Existing integral equation methods (i.e. Volume integral equations (VIEs), and volume-surface integral equations (VSIEs)) for analysis of fields generated inside highly-heterogenous objects suffer from one or both of the following:

high-contrast (HC) breakdown: when applied to scatterers with electric permittivities that are vastly different from those of the surrounding medium their discretization results in ill-conditioned systems of equations [24].

low-frequency (LF) breakdown: when the mesh that discretizes the scatterer contains elements with dimensions that are much smaller than the wavelength, discretization of the VSIE again results in ill-conditioned systems of equations. Ill-conditioned systems are ill-suited for solution by iterative methods as they converge slowly.

Consequently, integral equation-based tools cannot be used for TMS. In chapter 5, a new set of internally combined VSIEs (ICVSIEs) that do not exhibit either of the two ill-

conditioning phenomena, thus, enabling their use for TMS, is introduced. In Chapter 6, numerical examples demonstrating the usefulness of the ICVSIE for modeling TMS phenomena and analysis of other 3D objects are shown. The ICVSIE is not only applicable to high-contrast objects, but it is also useful for analysis of negative permittivity media. In Appendix A, results demonstrating its usefulness for analysis of scattering by highly-heterogenous plasmas is demonstrated.

CHAPTER 2
Numerical Analysis and Design of Single-Source Multi-Coil TMS for Deep and Focused Brain Stimulation

Many TMS applications call for large electric fields that are sharply focused on target regions deep in the brain [15, 25]. Unfortunately, present TMS coils generate rather diffuse fields that decay rapidly with distance from the scalp; these fields often excite tissue well outside the target region and/or fail to reach it altogether [26]. This chapter proposes a methodology for designing a new class of single-feed TMS coil arrays that significantly outperform present coils.

TMS coils capable of producing sharply focused fields that deeply penetrate the brain have been a long elusive research goal. To produce more focused excitations than achievable with a single circular loop [27], Ueno proposed the 'Figure-8' coil, which consists of two co-planar circular coils with currents flowing in opposite directions (Figs. 2.1(a-b)) [3]. Others enhanced his design by varying the loop radii, the loop inclination angle, and the number and orientation of the windings [4-6, 14, 15]. When compared to a single circular coil, the Figure-8 coil generates fields that are strongly concentrated near the coil center and thus produces a more compact excitation. Unfortunately, when using a Figure-8 coil to excite matter deep in the brain, large electric fields normal to the scalp are generated. These fields lead to charge buildup on the scalp surface and often cause painful muscle contractions [7]. To penetrate the brain more deeply than achievable with a Figure-8 coil, Roth et al. proposed the 'H-coil', which consists of a closed network of wires that run tangential to the scalp with feedback paths removed from the head (Fig. 2.1c) [8]. In contrast to a circular or Figure-8 coil, the H-coil induces electric fields that are mostly tangential to the scalp; hence it minimizes charge buildup on the air-scalp

interface and can be used to drive fields deeper into the brain. Unfortunately, the H-coil produces a rather uniform field across the scalp and results in little or no improvement in field focus over a Figure-8 coil. The literature abounds with studies of single-channel coils that represent various degrees of compromise between the Figure-8 and H-coils in terms of focus and penetration depth [9-15].

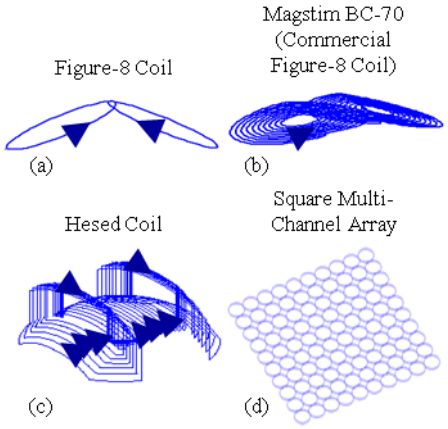

Figure 2.1 Popular TMS coils: (a) Figure-8 coil, (b) Magstim BC-70 (commercial figure-8 coil), (c) Hesed-coil, and (d) Square Multi-channel array.

To bypass the limitations of single-channel coils, array configurations are called for. Multi-channel TMS arrays composed of many independently driven coils have been shown to deliver a more concentrated and deeply penetrating field than single coils (Fig. 2.1d) [28]. That said, multi-channel arrays have never enjoyed the popularity of single-channel coils. We attribute this to two factors:

Lack of robust array optimizers: The total field induced in the head by a non-uniformly fed coil array is the superposition of the fields produced by the individual coils. As the latter are linearly proportional to their driving currents, the design of a multichannel coil array invariably involves a search for combinations of coil currents that result in electric fields that "optimally" stimulate the brain. To find optimal driving currents, Ruohonen et al. [28] suggested a technique that minimizes the difference between the total field and a desired field distribution. In [29], a Genetic Algorithm (GA),

viz. a robust search scheme that mimics natural evolution, was used to minimize total power dissipated in the head while maximizing the magnetic field at a target point and minimizing it at nearby locations. Other studies evaluated fields due to a small set of predetermined currents and ranked coil designs accordingly [30]. All these methods explicitly or implicitly require specification of a desired ideal field distribution that may be unrealizable, are somewhat limited in their ability to incorporate supplementary design constraints, and oftentimes assume idealized head models. For the use of coil arrays for TMS to become more widespread there needs to be a procedure that, given an array topology and a realistic model of the human head, can automatically and robustly find driving currents that achieve optimal trade-offs between penetration depth and compactness of excitation.

Difficulty of realizing multi-channel feeds: In previous studies, numerous planar and conformal array configurations have been considered. Planar arrays consisted of circular coils arranged on a rectangular or hexagonal grid [29]. Han et al [31] proposed using two parallel but mutually shifted arrays. They showed that the use of shifted arrays can improve field focus without decreasing coil radii, which is beneficial since arrays with elements with larger radii are easier to build. Conformal arrays have been designed by tilting the outer coils of a flat hexagonal arrangement [29] and by using loosely packed elements [30]. Unfortunately, each coil of the arrays requires an independent and expensive driver. The complexity and cost of present multi-channel feeds restricts the use of TMS coil arrays among researchers and clinicians.

Here, we suggest a two-pronged approach at eliminating the weaknesses of present methods for designing and implementing TMS coil arrays. First, we propose a GA-based optimization strategy that, for a given array configuration, robustly determines sets of driving currents that achieve Pareto-optimal trade-offs between field penetration depth and volume of excitation. The scheme seeks optimal combinations of fields produced by individual coils that are evaluated using a finite difference technique suited for modeling both idealized and realistic head models. Second, we propose a simple but effective scheme for converting a multi-channel array produced by the above optimizer into a single-channel configuration that performs (nearly) as well as the multi-channel design from which it originates. The transformation from multi- to single-channel arrays

is achieved by interconnecting and scaling the individual coils that make up the original multi-channel array. We demonstrate the above two-pronged approach by synthesizing single-channel rectangular arrays consisting of variable-radius circular coils (Figs. 2.2(b-c)) capable of producing highly focused fields. For example, the optimized single-channel array produces fields that penetrate 2.4 cm into the head while exciting 2.6 times less volume than a Figure-8 coil. When exciting 0.3% of the head's volume, the optimized array's fields reach 2.7 cm into the head while those of the Figure-8 coil do not penetrate deeper than 1.5 cm.

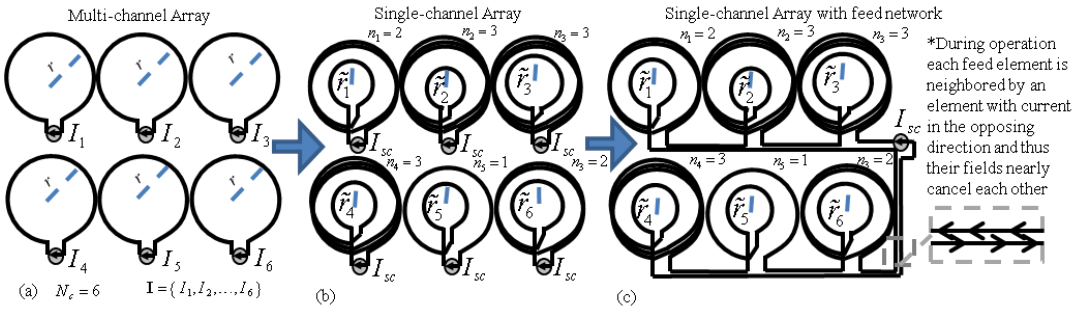

Figure 2.2 Conversion from a multi-channel array, driven with ...., to a single-channel array: (a) The initial multi-channel configuration. (b) New equivalent design consisting of multiple coils each containing multiple circular windings and an inner winding and with each element driven with an identical current . I_{sc} . (c) Final design with all the coil elements connected in series by a feed-network that during operation negligibly contributes to the stimulating field; this is done by placing elements, which have currents of opposing polarities close to each other.

2.1 Formulation

2.1.1 Design of Pareto-Optimal Multi-Channel Arrays

2.1.1.1 Problem Definition

We consider a multi-channel array composed of N_c . single-turn coils with fixed orientation, shape, dimension, and position relative to the head *H*. We assume that the

coils are driven by currents $\mathbf{I}(t)=\mathbf{I}\,p(t)$. where $\mathbf{I}=\{I_1,I_2,\ldots,I_{N_c}\}$ is a vector of current amplitudes and $p(t)$ is a known unit pulse, i.e. $|p(t)|_{\max}=1$. The head *H* is defined by its electric conductivity specified on a dense Cartesian grid. We develop a procedure for finding sets of driving currents $\mathbf{I}=\{I_1,I_2,\ldots,I_{N_c}\}$. that realize "Pareto-optimal trade-offs" between field penetration depth and excited volume. We first explain this concept.

The effects of TMS fields on the brain are complex, and highly dependent on the magnitude and timing of the TMS pulse [4]. Although small fields can potentially cause neurons to depolarize, we assume that neuronal activity occurs when the electric field magnitude exceeds an excitation threshold E_T. Throughout this chapter, we use $E_T=150\,\text{V/m}$[32]; we note that all procedures however remain valid for other threshold values as well. To characterize a current vector $\mathbf{I}$ in terms of its effectiveness at stimulating a target located d below the scalp surface, we define

$$B(\mathbf{I},d)=\begin{cases}\text{True} & |\mathbf{E}(d\,\hat{\mathbf{z}},\mathbf{I})|\geq E_T\\ \text{False} & |\mathbf{E}(d\,\hat{\mathbf{z}},\mathbf{I})|<E_T\end{cases}, \tag{2.1}$$

$$v(\mathbf{I})=\iiint\limits_{\mathbf{r}\in H\ \wedge\ |\mathbf{E}(\mathbf{r},\mathbf{I})|\geq E_T} 1\,d\mathbf{r}\,. \tag{2.2}$$

The Boolean penetration $B(\mathbf{I},d)$ indicates whether the target is excited and $v(\mathbf{I})$ is the volume of excited tissue. Here $|\mathbf{E}(\mathbf{r},\mathbf{I})|$ is the maximum of the magnitude of the electric field produced at $\mathbf{r}\in H$ for the duration of $p(t)$, and $\mathbf{r}=\boldsymbol{\rho}+z\hat{\mathbf{z}}$; $\hat{\mathbf{z}}$ is the unit vector along the z-axis and $\boldsymbol{\rho}\,\hat{\boldsymbol{\rho}}$ is a vector perpendicular to the z-axis, which is kept constant. This axis runs normal to the scalp surface; $z=0$ on the scalp surface and $z>0$ inside *H*. The location of the $z=0$ point on the scalp surface is application dependent. Next, we define $\mathbf{I}^{\text{opt}}(d)$ as

$$\begin{aligned}&\mathbf{I}^{\text{opt}}(d)=\arg\min_{\mathbf{I}\in\mathbb{R}^{N_c}} v(\mathbf{I})\\ &\text{subject to:}\qquad\qquad .\\ &\begin{cases} B\left(\mathbf{I}^{\text{opt}}(d),\,d\,\hat{\mathbf{z}}\right)=\text{True},\ \text{and}\\ |\mathbf{E}(\mathbf{r},\mathbf{I}^{\text{opt}}(d))|\leq E_M\ \ \forall\mathbf{r}\in H.\end{cases}\end{aligned} \tag{2.3}$$

Among all currents that generate fields that penetrate a distance *d* below the scalp surface, $\mathbf{I}^{\text{opt}}(d)$ excites the smallest volume. The second of the constraints ensures that field magnitudes never exceed E_M, a threshold beyond which painful muscle twitching may occur; we often use $E_M = 450\ \text{V/m}$ [7]. To find $\mathbf{I}^{\text{opt}}(d)$, we carry out an optimization procedure (detailed below) that starts from $d = 0$, and slowly increments d until $d = d_{\max}$. where (2.3) has no solution, meaning that no currents can be found that produce a large enough field d below the scalp surface without exceeding the maximum magnitude E_M elsewhere in *H*. The (Pareto) function $v\left(\mathbf{I}^{\text{opt}}(d)\right) = v^{\min}(d),\ 0 \le d < d_{\max}$ provides the smallest excitation volume possible for a given target depth *d*; its inverse $d^{\max}(v)$ yields the largest depth that can be reached for a given excitation volume. The set of currents $\mathbf{I}^{\text{opt}}(d)$ is termed Pareto-optimal, as they represent excitations that optimally trade-off penetration depth versus excitation volume.

Sections 3.2.1.2 and 3.2.1.3 below describe methods for solving optimization problem (2.3) for a given *d*, and for rapidly evaluating $|\mathbf{E}(\mathbf{r},\mathbf{I})|$.

2.1.1.2 Genetic Algorithm for Finding $\mathbf{I}^{\text{opt}}(d)$

To find $\mathbf{I}^{\text{opt}}(d)$, we execute a simple, single-objective GA made out of various functions from Matlab's GA toolbox [33]. Briefly, GAs generate solutions to optimization problems by mimicking natural evolution [34]. When compared to gradient-based optimization schemes, they are well-suited for solving optimization problems involving highly multimodal cost functions. Our experience indicates that (2.3) falls in this category. To this end, GAs consider not one, but successive "populations of candidate designs" that, on average, exhibit improved characteristics. In our problem, the optimization parameters are scaled currents $\tilde{I}_i,\ i = 1,...,N_c$ assigned integer values between -999 and 999. These scaled currents or "genes" are arranged in a "chromosome" describing a scaled candidate design as $\tilde{\mathbf{I}} = \left\{\tilde{I}_1, \tilde{I}_2, \ldots, \tilde{I}_{N_c}\right\}$. An initial population of N_{pop} candidate designs $\left\{\tilde{\mathbf{I}}^1, \tilde{\mathbf{I}}^2, ..., \tilde{\mathbf{I}}^{N_{\text{pop}}}\right\}$ is assembled by randomly selecting the value of each gene in every chromosome uniformly from the above range. Next, the (maximum in

time) magnitudes of the field $\mathbf{E}(\hat{\mathbf{z}}d,\tilde{\mathbf{I}}^j)$ is computed for all candidate designs, and unscaled currents are computed as

$$\mathbf{I}^j = \frac{\tilde{\mathbf{I}}^j E_T}{|\mathbf{E}(\hat{\mathbf{z}}d,\tilde{\mathbf{I}}^j)|}, \tag{2.4}$$

thereby guaranteeing that the fields of the unscaled candidate design reach the target depth *d*, i.e. $|\mathbf{E}(\hat{\mathbf{z}}d,\mathbf{I}^j)|= E_T$. Next, for each member of the population, we compute the cost function

$$C(j) = \begin{cases} v(\mathbf{I}^j) & \text{if } \max_{\mathbf{r}\in H}\left|\mathbf{E}(\mathbf{r},\mathbf{I}^j)\right| \le E_M \\ \iiint_{\mathbf{r}\in H} 1\, d\mathbf{r} & \text{if } \max_{\mathbf{r}\in H}\left|\mathbf{E}(\mathbf{r},\mathbf{I}^j)\right| > E_M \end{cases}, \tag{2.5}$$

and rank all candidate designs according to their cost function value. Finally, a new generation of candidate designs is generated by executing three operations. First, the $N_{\text{elite}} < N_{\text{pop}}$ candidate designs with the lowest cost function values are automatically carried over to the next generation. Next, $N_{\text{pop}} - N_{\text{elite}}$ additional designs are generated by mating old candidate designs by recombining their genes. The participation of old candidate designs in the mating process is governed by a process known as roulette wheel selection, designed to ensure that the "fittest" among the old candidates designs produce more offspring than average candidate designs. Assuming that old candidate designs $\tilde{\mathbf{I}}^i$ and $\tilde{\mathbf{I}}^j$ are selected for mating, their offspring is $\tilde{\mathbf{I}}^{child} = \lfloor (1-\beta)\tilde{\mathbf{I}}^i + \beta\tilde{\mathbf{I}}^j \rfloor$; β is randomly selected in the range $0<\beta<1$ and $\lfloor . \rfloor$ rounds to the nearest integer. Finally, all chromosomes representing new candidate designs are subject to mutation, that is, small perturbations designed to maintain genetic diversity.

The process of generating new populations from old ones is repeated until no appreciable improvements in the lowest value of the cost function recorded are made. The unscaled candidate design with the lowest cost value encountered during the GA run is returned as $\mathbf{I}^{\text{opt}}(d)$.

2.1.1.3 Fast Computation of Fields Due to Prescribed Coil Currents

Execution of the GA often requires hundreds of thousands of evaluations of electric fields $\mathbf{E}(\mathbf{r},\mathbf{I})$ throughout H excited by magnetic fields produced by prescribed coil currents $\mathbf{I}$. This section therefore describes a technique for computing these fields rapidly.

Let $\mathbf{E}_i(\mathbf{r},t)$ denote the electric field at position $\mathbf{r} \in H$ when coil i supports current $p(t)$; all other coils are assumed inactive. For typical $p(t)$, see [35]. All fields $\mathbf{E}_i(\mathbf{r},t),\ i=1,...,N_c$ are computed prior to starting the optimization process using the quasi-static finite difference method for typical TMS pulses with maximum frequency in the 1-10 kHz range proposed by Cerri [36]. The method assumes that inductive coupling involving eddy-currents generated inside the brain can be neglected; it also neglects displacement currents because inside brain tissue they are much smaller than the conduction currents generated by typical TMS pulses. Using this method we first calculate the magnetic field $\mathbf{B}_i(\mathbf{r},t)$ using the Biot-Savart law as

$$\mathbf{B}_i(\mathbf{r}) = p(t)\mathbf{L}_i(\mathbf{r}), \tag{2.6}$$

where

$$\mathbf{L}_i(\mathbf{r}) = \frac{\mu_0}{4\pi} \oint_{\text{Coil i}} \hat{\mathbf{t}}_i(s) \times \frac{\mathbf{r}-\mathbf{r}_i(s)}{\left|\mathbf{r}-\mathbf{r}_i(s)\right|^3}\, \mathrm{d}s. \tag{2.7}$$

Here μ_0 is the free-space permeability, s is a length coordinate that varies in the interval $0 \le s < C_i$ with C_i the circumference of coil i, $\mathbf{r}_i(s)$ denotes a position vector on coil i, and $\hat{\mathbf{t}}_i(s)$ is the unit vector tangential to coil i at $\mathbf{r}_i(s)$. Throughout the head H and its surroundings, the electric field $\mathbf{E}_i(\mathbf{r},t)$ satisfies

$$\oint_{\mathrm{C}} \mathbf{E}_i(\mathbf{r},t)\cdot \mathrm{d}\mathbf{l} = -\frac{\mathrm{d}}{\mathrm{d}t}\iint_{\mathrm{S}} \mathbf{B}_i(\mathbf{r},t)\cdot \mathrm{d}\mathbf{s} = -\frac{\mathrm{dp(t)}}{\mathrm{d}t}\iint_{\mathrm{S}} \mathbf{L}_i(\mathbf{r})\cdot \mathrm{d}\mathbf{s}, \tag{2.8}$$

$$\iint_{\mathrm{S_c}} \sigma(\mathbf{r})\mathbf{E}_i(\mathbf{r},,t)\cdot \mathrm{d}\mathbf{s} = 0, \tag{2.9}$$

where $\sigma(\mathbf{r})$ denotes the conductivity at $\mathbf{r}$, C is an arbitrary contour enclosing a surface S, and S_c is an arbitrary closed surface. Jumps in the electric field across boundaries (enforced by (9)) result in charges and hence they are (implicitly) accounted for by the model. To solve eqns. (2.7)-(2.9) for $\mathbf{E}_i(\mathbf{r},t)$, we again follow Cerri [36] and use a quadrature rule to calculate the magnetic field $\mathbf{B}_i(\mathbf{r},t)$ throughout a rectangular domain that contains the coil and head. Then, we solve for the electric field by approximating the brain by a collection of homogenous (i.e. constant $\sigma(\mathbf{r})$) conductive cubic cells. We consider as unknowns the components of $.\mathbf{E}_i(\mathbf{r},t)$. normal to, and sampled at, the centers of cell facets. To solve for these unknowns, we apply (2.8) on cell faces and use magnetic fields computed using (2.8) to evaluate its right hand side. Eqn. (2.9) is applied on a cubic volume centered about each node. The resulting sparse system of equations for the sampled component values of $\mathbf{E}_i(\mathbf{r},t)$ is solved by an iterative least squares (LSQR) procedure [37]. The LSQR procedure is terminated when the sampled component field values result in a relative residual norm error that is less than $.10^{-6}$ ..

Let $\mathbf{E}(\mathbf{r},t,\mathbf{I})$ denote the total electric field due to currents $\mathbf{I}(t)$. Clearly, $\mathbf{E}(\mathbf{r},t,\mathbf{I})$ can be computed by linear superposition of the fields $\mathbf{E}_i(\mathbf{r},t)$ as

$$\mathbf{E}(\mathbf{r},t,\mathbf{I}) = \sum_{i=1}^{N_c} I_i \, \mathbf{E}_i(\mathbf{r},t) \,. \tag{2.10}$$

In what follows, let $\mathbf{E}_i(\mathbf{r}) = \mathbf{E}_i(\mathbf{r},t_{\max})$ denote $\mathbf{E}_i(\mathbf{r},t_{\max})$, where $t_{\max}$ maximizes $|\partial p(t)/\partial t|$ for the duration of the TMS pulse. As each coil is excited by the same pulse shape, $t_{\max}$ does not depend on *i*. The well-defined field $\mathbf{E}(\mathbf{r},\mathbf{I}) = \mathbf{E}_i(\mathbf{r},t_{\max},\mathbf{I})$ therefore can be computed as

$$\mathbf{E}(\mathbf{r},\mathbf{I}) = \sum_{i=1}^{N_c} I_i \, \mathbf{E}_i(\mathbf{r}) \,. \tag{2.11}$$

Since the fields $\mathbf{E}_i(\mathbf{r})$ are precomputed prior to executing the GA, (2.11) can be evaluated for many different $\mathbf{I}$ at minimal computational cost.

2.1.2 Conversion of Multi-Channel Array to Single-Channel Array

The above procedure yields a set of Pareto-optimal driving currents $\mathbf{I}^{\text{opt}}(d) = \{I_1^{\text{opt}}(d), I_2^{\text{opt}}(d), ..., I_{N_c}^{\text{opt}}(d)\}$ for penetration depths $0 < d \le d_{\max}$. In principle, these currents can be stored in a look-up table and fed into the array's N_c coils by means of separate tunable drivers (Fig. 2.2a). While costly and bulky, such a feed would permit on-the-fly array reconfiguration to reach varying targets using Pareto-optimal, minimum volume excitations.

If no reconfiguration is required, that is, if the array targets a fixed penetration depth d^*, then the multi-channel array can be converted into a single-channel (sc) array that is much cheaper to construct. The single-channel array is fed a current $I_{sc} = \alpha \max\{|I_i^*|, i = 1, ..., N_c\} > 0$ where $I_i^* = I_i^{\text{opt}}(d^*)$ and α is typically chosen in the range $0.05 < \alpha < 0.2$ (See Section 3.3.3). To simplify the discussion, we assume that the single-turn coils in the multi-channel array are circular with radius r; the proposed procedure is easily generalized to other coil shapes as well. The conversion procedure involves two steps.

First, each single-turn coil in the multi-channel array is replaced by a multi-turn coil (Fig. 2.2b). Specifically, single-turn coil *i* is replaced by a multi-turn coil with $n_i + 1$ windings: n_i windings of the original coil and a single, concentrically positioned coil of radius $\tilde{r}_i < r$, with

$$n_i = \left\lfloor \left| \frac{I_i^*}{I_{sc}} \right| \right\rfloor, \tag{2.12}$$

$$\tilde{r}_i = \sqrt{r^2 |I_i^*/I_{sc}| - n_i r^2}\,. \tag{2.13}$$

The large and small coils are connected and their windings have identical polarity. The total magnetic dipole moment of a single-turn coil traversed by current I_i^* is identical to that of composite coil *i* traversed by I_{sc}. Beyond a certain distance from the coil, the fields generated by a composite coil therefore will closely match those of its single-turn counterpart; hence, the composite coils will stimulate a region closely matching that of its parent design.

Second, all multi-turn coils connected in series using a carefully designed feed-network that negligibly contributes to the stimulating field (Fig. 2.2c). This is achieved by arranging the feed in such a way that each current introduced by the feed network during operation is neighbored by a current of opposing polarity to allow feed network field cancellation.

2.2 Results

Even though the proposed technique can be applied to any multi-channel array configuration, here we limit ourselves to planar and densely packed square arrays of $\sqrt{N_c} \times \sqrt{N_c}$ circular coils with radius r and array area $A = 4r^2 N_c$ positioned symmetrically w.r.t. and 1 cm removed from the head (Fig. 2.3a). Each time we consider one of 24 arrays resulting from all the possible combinations of $N_c = 16,\ 36,\ 64,\ \text{and}\ 100$, and $r = 4,\ 6,\ 8,\ 10,\ \ 14,\ \text{and}\ 18\ \text{mm}$. The $d^{\max}(v)$ Pareto curves for each design are compared to a similar '$d_{F8}^{\max}(v)$' Pareto curves for the Figure-8 coil. The $d_{F8}^{\max}(v)$ curve and its inverse $v_{F8}^{\min}(d)$ where generated by brute-force search, that is by varying a Figure-8's loop current and radii (allowed range: 15 to 30 mm), the angle between its loops (allowed range: 0 to 180 degrees), and the height of its vertex above the head (allowed range: 1 to 3 cm) (Fig. 2.3b). Note that to generate $d_{F8}^{\max}(v)$ Pareto curves, we analyzed Figure-8 coils with different sizes and shapes, and positioned at various positions relative to the head; in contrast, to generate $d^{\max}(v)$ Pareto curves for multi-channel designs we only vary the amplitudes of the driving currents fed into the coils.

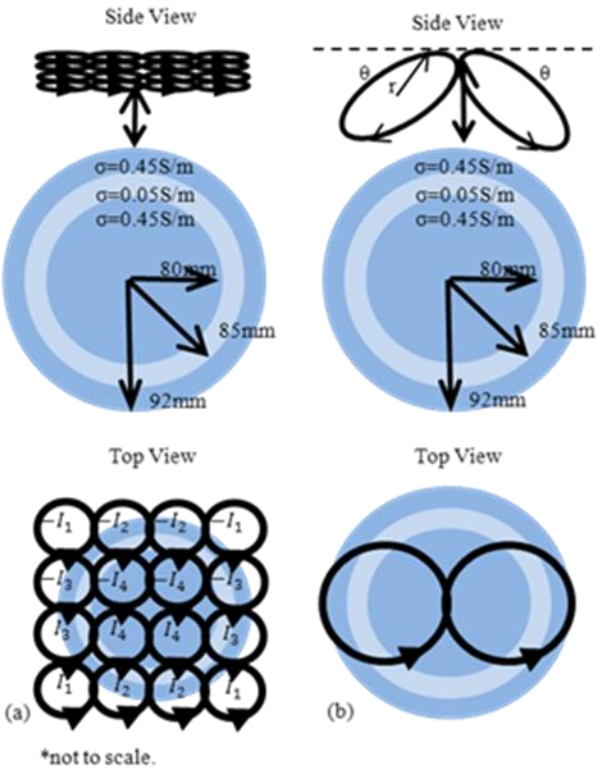

Figure 2.3 Three-sphere head model. (a) The array is placed 10 mm above the scalp and centered about the target column (z-axis). (b) The vertex of the figure-8 coil is on the target column at a height that varies between the 10 mm to 30 mm above the head; to find $d_{F-8}^{\max}(v)$ we allow both the radius (r) and angle (θ) to vary between 15mm to 30 mm and 0 to 180 degrees. Three-sphere head model. (a) The array is placed 10 mm above the scalp and centered about the target column (z-axis). (b) The vertex of the figure-8 coil is on the target column at a height that varies between the 10 mm to 30 mm above the head; to find $d_{F-8}^{\max}(v)$ we allow both the radius (r) and angle (θ) to vary between 15mm to 30 mm and 0 to 180 degrees.

Sections 2.3.1 and 2.3.2 demonstrate the applicability of the proposed method to the design of multi-channel arrays residing above a three (concentric) spherical head model [38] and a model constructed by segmentation of in vivo MRI data [14].

2.2.1 Multi-Channel Designs For Three-Sphere Head Model

We consider the 'Three-sphere' conductive model for the head proposed by Rush and Driscoll [38], commonly used to benchmark TMS coils. The model is defined by 3 concentric spheres with radii of 80, 85, and 92 mm. The inner sphere and the two shells that cover it model brain, skull, and skin tissue (Figs. 2.3(a-b)) and have conductivities of 0.45 S/m, 0.05, and 0.45 S/m. We approximate the Three-sphere head by $62 \times 62 \times 62$ homogenous cubic voxels each having an edge length of 3mm; each voxel is assigned a conductivity corresponding to that of the Three-sphere head at the voxel center.

Figs. 3.4(a-f) show $d^{\max}(v)$ for $r = 4,\ 6,\ 8,\ 10,\ 14,$ and 18 mm together with $d_{F-8}^{\max}(v)$; each subplot shows Pareto curves for $N_c = 16,\ 36,\ 64,$ and 100. The optimized multi-channel arrays always outperform optimized Figure-8 coils, that is, all $d^{\max}(v)$ curves reside above the $d_{F-8}^{\max}(v)$ curve. This means that for a given excitation volume, multi-channel arrays always produce fields that reach deeper into the head than those of the Figure-8 coil. Equivalently, for a given penetration depth, the multi-channel arrays excite less volume. (Note: for two of twenty-four arrays ($N_c = 16$; $r = 4,\ 6$ mm), the safety limit of $E_M = 450$ V/m is encountered when the penetration depth is less than 30 mm, a depth achievable by the Figure-8 coils) Table 2.1 lists the minimum $v^{\min}(d = 15,\ 18,\ldots,\ 30\ \text{mm})$ for all (N_c, r) combinations considered, along with $v_{F-8}^{\min}(d)$. Fig. 2.4 and Table 2.1 reveal that multi-channel arrays can significantly outperform Figure-8 coils. For example, fields produced by an array consisting of $N_c = 64$ coils with $r = 14$ mm can penetrate $d = 30$ mm deep into the head while exciting four times less volume than a Figure-8 coil.

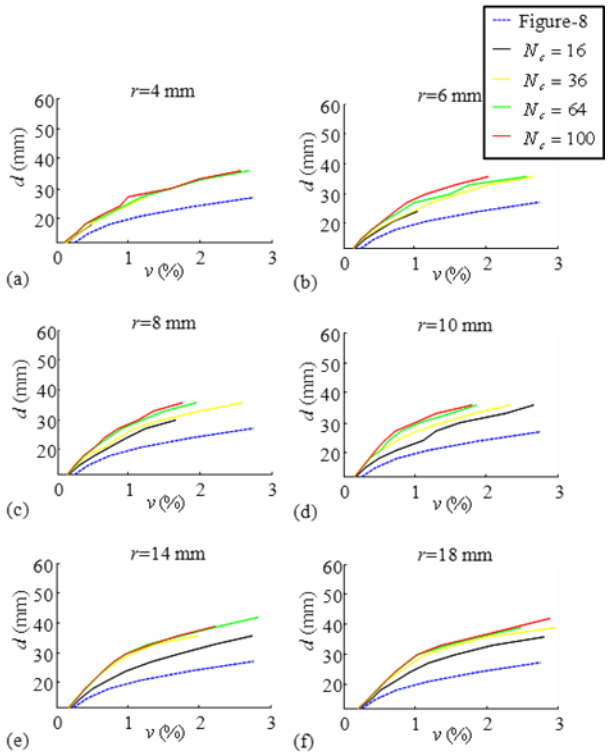

Figure 2.4 Largest depth that can be reached for a given excitation volume by multi-channel arrays ($d^{\max}(v)$) and figure-8 coils ($d_{F-8}^{\max}(v)$). (a-f) Each have individual curves for each array with different number of coils N_c and each individual panel has results for arrays with coils of radius $r = 4,\ 6,\ 8,\ 10,\ 14,$ and 18 mm, respectively.

Array				Figure 8	
r	N_c	Depth	Excited Volume	Depth	Excited Volume
6mm	100	15mm	0.25%	15mm	0.44%
8mm	100	18mm	0.37%	18mm	0.74%
10mm	100	21mm	0. 45%	21mm	1.17%
10mm	100	24mm	0. 58%	24mm	1.88%
10mm	100	27mm	0. 73%	27mm	2.75%
14mm	64	30mm	0. 98%	30mm	3. 97%

Table 2.1 Smallest volume $v^{\min}(d)$ of all array configurations considered and $v_{F-8}^{\min}(d)$ for three-sphere head

Figs. 2.4(a-f) also show that for given v, $d^{\max}$ increases with N_c while keeping r fixed, and (mostly) with r while keeping N_c constant. Note that increasing N_c and r also increases A. Thus, it is unclear from Fig. 2.4, which of these parameters was the

most responsible for these gains. In order to elucidate this question, figs. 2.5(a-f) show Pareto curves for arrays with different r and N_c but the same A for each subplot. Specifically, they show $d^{\max}(v)$ for arrays with $A = 48^2$, 64^2, 80^2, 96^2, 120^2, and 160^2 mm^2 together with $d_{F-8}^{\max}(v)$; The plots indicate that increasing A greatly increases $d^{\max}(v)$, whereas decreasing r and increasing N_c while keeping A constant only marginally increases $d^{\max}(v)$. In general, a bigger array is able to reach deeper into the head than a smaller one. Note: $d^{\max}(v)$ for array $(N_c = 36, r = 14mm)$ and $(N_c = 100, r = 14mm)$ are almost identical, and thus, increasing A beyond a size comparable to the head surface seems to have marginal effects on $d^{\max}(v)$; this is because as A increases some of the coils are far away from the head and hence do not generate strong enough fields to greatly affect the stimulated region.

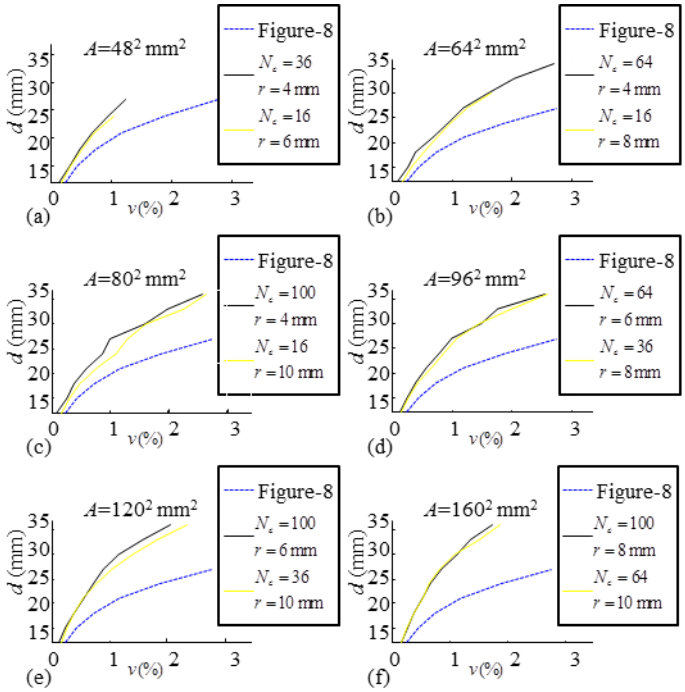

Figure 2.5 Largest depth that can be reached for a given excitation volume by multi-channel arrays ($d^{\max}(v)$) and figure-8 coils ($d_{F-8}^{\max}(v)$). (a-f) Each have individual curves for each array with different N_c and r but the same A and each individual has arrays with $A = 48^2$, 64^2, 80^2, 96^2, 120^2, and 160^2 mm^2, respectively.

To aid in the visualization of how the use of array coils is beneficial, fig. 2.6 shows the magnitude of the electric field distribution maps $|\mathbf{E}(\mathbf{r},\mathbf{I}^{\text{opt}}(d=24\,\text{mm}))|$ for an array (with $N_c=100$ and $r=10\,\text{mm}$) compared to the electric fields generated by the optimal Figure-8 coil along the coronal and medial planes (orthogonal longitudinal planes intersecting on the $z=0$ axis). As evidenced by fig 2.6, the electric fields generated by the multi-channel array produce a far more compact excitation than the Figure-8 coil; in fact, for this particular case, the excited volume $v^{\min}$ for the array was 3.24 times smaller than $v_{F-8}^{\min}$.

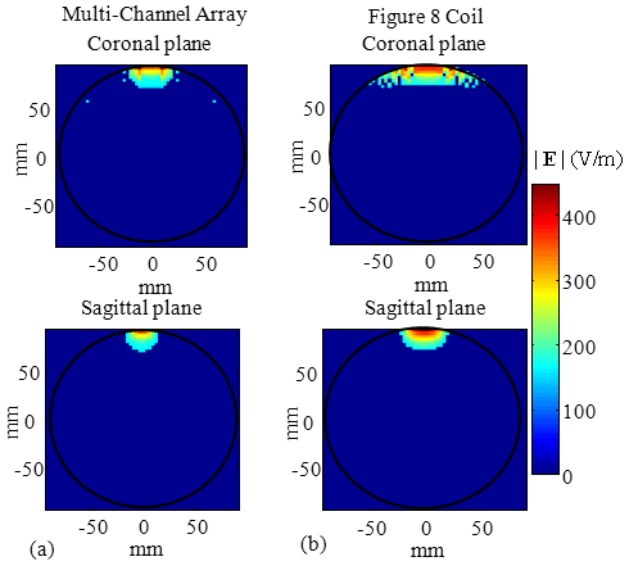

Figure 2.6 (a) The magnitude of the electric field $|\mathbf{E}(\mathbf{r})|$ produced inside the stimulated volume by a coil array with 100 coils of 10 mm radius and driven with currents optimized for a penetration depth of 24 mm (i.e., driven with $\mathbf{I}^{\text{opt}}(d=24\,\text{mm})$). (b) The magnitude of the electric field $|\mathbf{E}(\mathbf{r})|$ produced inside the stimulated volume by a figure-8 coil of 25 mm radius also optimized for a penetration depth of 24 mm.

We next focus on the currents $\mathbf{I}^{\text{opt}}(d)$ required by multi-channel arrays for varying (N_c, r). Specifically, we study the norm of the driving current $\left\|\hat{\mathbf{I}}^{\text{opt}}(d)\right\|$ and the average current I_{avg} defined as

$$\left\|\hat{\mathbf{I}}^{\text{opt}}(d)\right\| = \sum_{I_i \in \mathbf{I}} \left| \frac{dp(t_{\max})}{dt} I_i^{\text{opt}}(d) \right|. \tag{2.14}$$

$$\hat{I}_{avg} = \frac{\left\|\hat{\mathbf{I}}^{\text{opt}}(d)\right\|}{N_c}. \tag{2.15}$$

Figs. 2.7(a-f) show $\left\|\mathbf{I}^{\text{opt}}(d)\right\|$ for $r = 4,\ 6,\ 8,\ 10,\ 14,$ and 18 mm; each subplot shows curves for $N_c = 16,\ 36,\ 64,$ and 100. Commercial TMS Figure-8 coils typically consist of two coils side by side each with $8-12$ windings, and require currents of 0.342 kA/μs [39] to induce electric fields of about 300 V/m in the cortex. As expected, $\left\|\mathbf{I}^{\text{opt}}(d)\right\|$ increases with N_c. However, this increase is only marginal and in most cases accompanied by a reduction in I_{avg}. For example, an array with $N_c = 36$ and $r = 10$ mm requires $\left\|\mathbf{I}^{\text{opt}}(d = 24\text{ mm})\right\| = 80$ kA/μs while one with $N_c = 100$ and $r = 10$ mm requires $\left\|\mathbf{I}^{\text{opt}}(d = 24\text{ mm})\right\| = 150$ kA/μs, less than a two-fold increase, but I_{avg} was reduced by a factor of 0.68. In addition, $\left\|\mathbf{I}^{\text{opt}}(d)\right\|$ greatly decreases with r. For example, an array with $N_c = 36$ and $r = 4$ mm requires $\left\|\mathbf{I}^{\text{opt}}(d = 24\text{ mm})\right\| = 670$ kA/μs while an array with $N_c = 36$ and $r = 6$ mm requires $\left\|\mathbf{I}^{\text{opt}}(d = 24\text{ mm})\right\| = 110$ kA/μs. This is a six-fold decrease in $\left\|\mathbf{I}^{\text{opt}}(d)\right\|$ and since N_c is the same for both arrays there is also a six-fold decrease in I_{avg}. Increasing A increases $d^{\max}(v)$ while (almost always) decreasing $\left\|\mathbf{I}^{\text{opt}}(d)\right\|$ and I_{avg}.

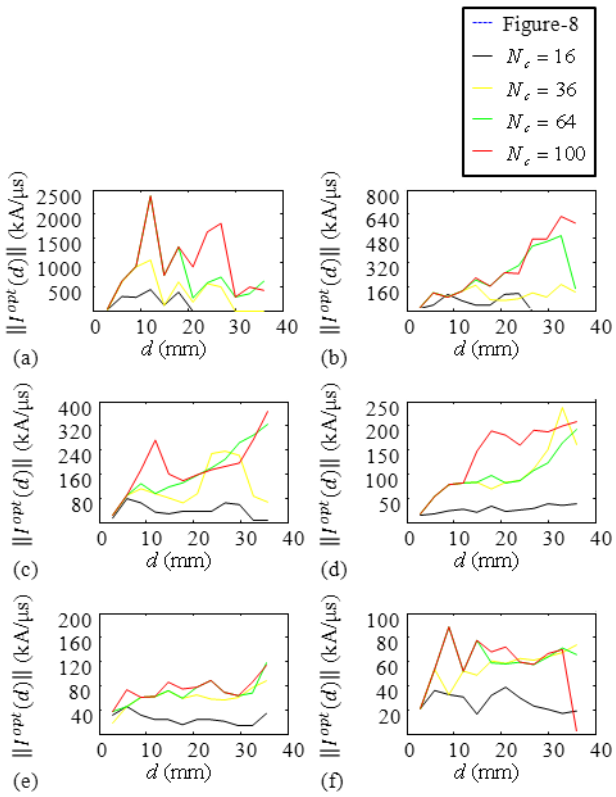

Figure 2.7 Total current required by each array driven with currents optimized for each penetration depth $\mathbf{I}^{\text{opt}}(d)$ penetration depth (i.e., $\left\|\mathbf{I}^{\text{opt}}(d)\right\|$), (a-f) Each have individual curves for each array with different number of coils N_c and each individual panel has results for arrays with coils of radius $r = 4,\ 6,\ 8,\ 10,\ 14,$ and 18 mm, respectively.

We next address feasibility of the proposed designs. TMS coils having a radius of 12.5 mm driven by currents much greater than the ones we require have previously been fabricated [40]. We believe that using the same procedures as in [40], all of the arrays consisting of circular coils having $r = 10,\ 14,$ and 18 mm can be constructed; that said, building arrays consisting of coils having $r = 4,\ 6,$ and 8 mm remains a difficult proposition. If two arrays have the same area the one consisting of smaller coils only marginally outperforms the one with larger coils. In practice, this obviates the need to build coils of radius less than 10mm, which has been proven challenging in the past [40]. To analyze the mechanical robustness of the proposed designs, we used Comsol [41] to

compute the von Mises stresses [42] in all coils, and determined that they are lower than the tensile strength of N-10 gauge copper wire [43].

2.2.2 Multi-Channel Designs For MRI-Derived Head Model

We consider a 'MRI-derived' conductivity model of the human head (Figs. 2.8a-f) created by segmenting a high resolution MRI image and assigning electrical conductivity values to each tissue type using data from literature [44] and given in Table 2.2.

Tissue Type	Conductivity (S/m)
Scalp	0.33
Skull	0.0042
Cerebrospinal Fluid	1.79
Gray Matter	0.33
White Matter	0.14

Table 2.2 Tissue Conductivity values

The MRI image consists of $256\times256\times124$ homogenous cubic voxels each having an edge length of 1.2 mm and was obtained by scanning a single male subject in a 3T GE Signa scanner (Waukesha, WI) using an IR-prepped, 3D, SPGR pulse sequence (TR=9.03, TE = 1.84, TI = 500 ms, FOV = 24 cm, slice thickness = 1.2 mm). First, the image is segmented into gray matter, white matter, and ventricular CSF by the SPM5 segmentation toolbox (http://www.fil.ion.ucl.ac.uk/spm). Next, remaining unclassified tissue is further partitioned into another three types, namely bone, muscle, and CSF, by FAST, a component of FSL's image analysis package (http://www.fmrib.ox.ac.uk/fsl/). Each voxel is assigned a single conductivity corresponding to the average of the conductivities inside it. The resulting conductivity maps are sub-sampled to $128\times128\times62$ voxels with an edge length of 2.4 mm by averaging the conductivity values of each $2\times2\times2$ block of voxels of the original image. The subsampling speeds up the computation of the optimum driving currents via the GA without deteriorating the quality of the final results. As shown in Figs. 2.8 (a-f), the coil is positioned such that its normal at the center of the coil crosses through the motor cortex.

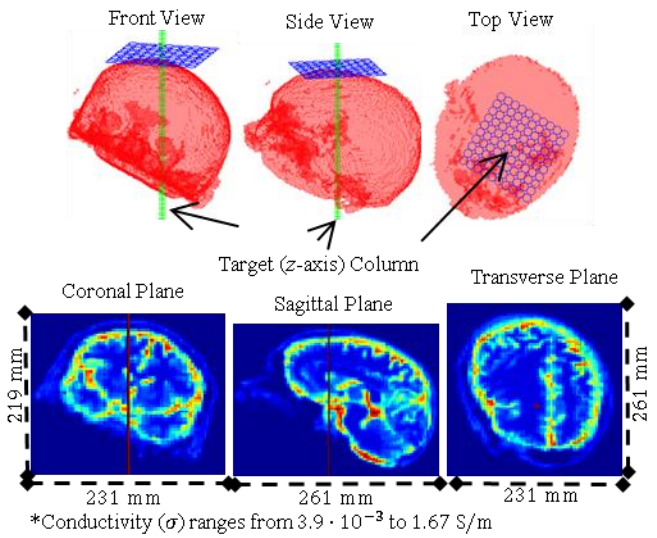

Figure 2.8 Conductivity model of the head derived from an MRI image. The field of view was $231 \times 261 \times 219$ mm. The conductivity of tissue ranged from 3.9×10^{-3} to 1.67 S/m. The array was placed 10 mm above the head.

First, we investigate the fields generated by the arrays, when driven with the $\mathbf{I}^{\text{opt}}(d)$ obtained for the Three-sphere head, inside the MRI-derived head. Specifically, we consider the arrays that can excite each depth d into the head while exciting a $v^{\min}$ volume that is smaller than all other (N_c, r) configurations. We analyzed the fields generated by each array inside the MRI-derived model, while exciting it's respective d, and generate a $d(v)$ curves. Figs. 2.9(a-b) show $d(v)$ and the same curve for the figure-8 coils $d_{F-8}^{\max}(v)$. For completeness, we also show the $d(v)$ curve that results when using the same $\mathbf{I}^{\text{opt}}(d)$ currents in arrays operating in free-space. (Note: that the $d_{F-8}^{\max}(v)$ curve becomes flat at depth of 27 mm for the MRI-derived head, and 21 mm for free-space, this is because the safety limit of 450 V/m is encountered and this is the maximum depth achievable by the Figure-8 coils.) Although the multi-channel arrays optimized for operation near a Three-sphere head model continue to outperform Figure-8 coils when operating near the MRI-derived head, the gains are significantly reduced. The same observation holds true when the coils operate in free-space. This is not surprising because the excited region inside the MRI-derived head is known to significantly differ from that of the Three-sphere head

even if the same TMS coil is used [44]. The multi-channel arrays optimized for operation near a Three-sphere head thus are suboptimal for targeting inside a realistic head model.

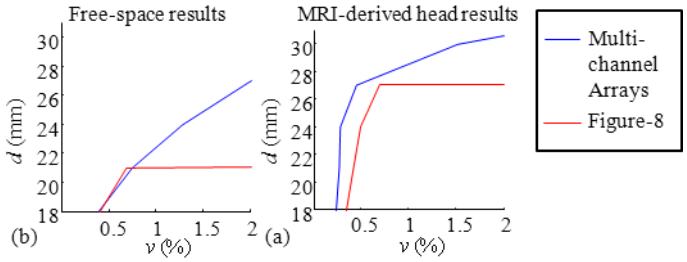

Figure 2.9 Penetration depth achieved as a function of excitation volume ($d(v)$) by the multi-channel arrays and figure-8 coils for targeting inside the three-sphere head. (a) Results obtained for targeting inside the MRI-derived head. (b) Results obtained for targeting inside free-space region. Note that in both cases, achieving a penetration depth beyond 27 and 21 mm, respectively, required exceeding the safety threshold.

We therefore derived a new set of $\mathbf{I}^{\text{opt}}(d)$ for each of the arrays assuming they operate near the MRI-derived head model. Figs. 2.10(a-f) and 2.11(a-f) show $d^{\max}(v)$ for $r = 4,\ 6,\ 8,\ 10,\ 14,\ \text{and}\ 18\ \text{mm}$, together with $d_{F-8}^{\max}(v)$, for the MRI-derived head in the same way as Figs. 2.4(a-f) and 3.5(a-f). Again, the optimized multi-channel arrays always outperform optimized Figure-8 coils. Notably, the realized gains greatly exceed those observed when the arrays driven by the Three-sphere head $\mathbf{I}^{\text{opt}}(d)$ where used inside the MRI-derived head. Table 2.3 lists the minimum $v^{\min}(d = 15,\ 18,\ldots,\ \ 30\ \text{mm})$ for all (N_c, r) combinations considered, along with $v_{F-8}^{\min}(d)$. Table 2.2 reveals that multi-channel arrays can significantly outperform Figure-8 coils at targeting inside the MRI-derived head. For example, fields produced by an array consisting of $N_c = 100$ coils with $r = 8\ \text{mm}$ can penetrate 24 mm into the head while exciting 3.0 times less volume than a Figure-8 coil. Also, when exciting 0.3% of the head's volume the optimized array's fields reach 2.7 cm into the head while those of the Figure-8 coil do not penetrate deeper than 1.5 cm.

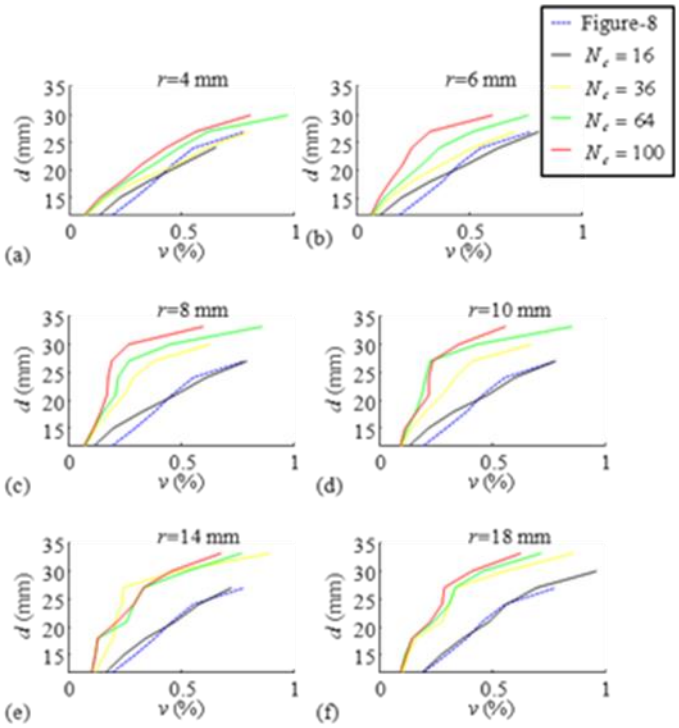

Figure 2.10 Largest depth that can be reached for a given excitation volume by multi-channel arrays ($d^{\max}(v)$) and figure-8 coils ($d_{F-8}^{\max}(v)$). (a-f) Each have individual curves for each array with different number of coils N_c and each individual panel has results for arrays with coils of radius $r = 4,\ 6,\ 8,\ 10,\ 14,$ and 18 mm, respectively.

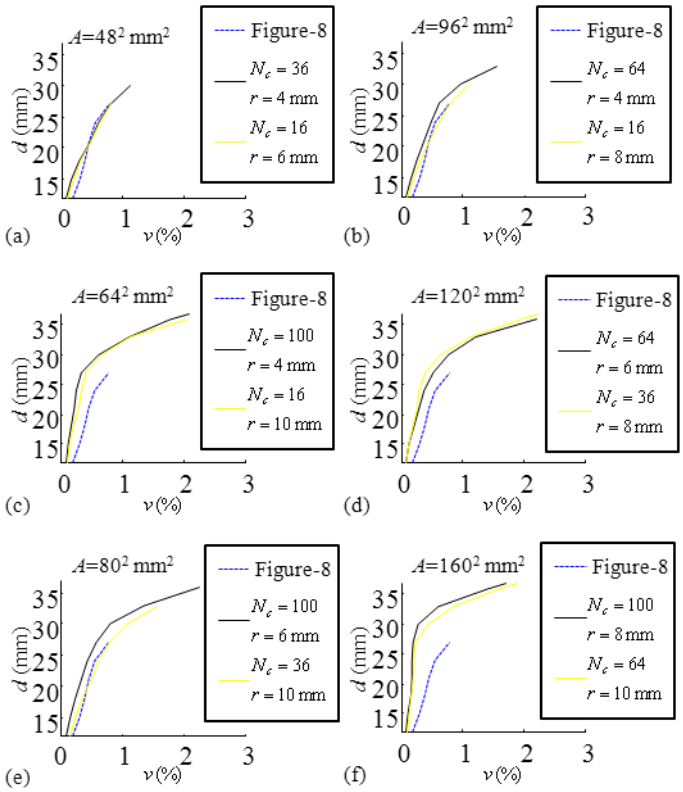

Figure 2.11 Largest depth that can be reached for a given excitation volume by multi-channel arrays ($d^{\max}(v)$) and figure-8 coils ($d_{F-8}^{\max}(v)$). (a-f) Each have individual curves for each array with different N_c and r but the same A and each individual has arrays with $A = 48^2$, 64^2, 80^2, 96^2, 120^2, and 160^2 mm^2, respectively.

Array				Figure 8	
r	N_c	Depth	Excited Volume	Depth	Excited Volume
14mm	100	15mm	0.10%	15mm	0. 30%
8mm	64	18mm	0. 13%	18mm	0. 38%
8mm	100	21mm	0. 17%	21mm	0. 46%
8mm	100	24mm	0. 18%	24mm	0.55%
8mm	100	27mm	0. 19%	27mm	0.78%
10mm	100	30mm	0.27%	30mm	--

Table 2.3 $v^{\min}(d)$ of all array configurations considered and $v_{F-8}^{\min}(d)$ for MRI-derived head

As was observed for the Three-sphere head, $d^{\max}(v)$ increases with N_c while keeping r fixed, and (mostly) with r while keeping N_c constant. Also, $d^{\max}(v)$ increases with A, whereas decreasing r and increasing N_c while keeping A constant only marginally increases $d^{\max}(v)$. Generally speaking, larger area arrays are capable of generating fields deeper into the head than smaller ones, and if two arrays have the same physical dimensions the one consisting of smaller coils marginally outperforms the one with larger ones.

Figs. 2.12(a-f) show $\left\|\mathbf{I}^{\text{opt}}(d)\right\|$ for $r = 4,\ 6,\ 8,\ 10,\ 14,\ \text{and}\ 18\ \text{mm}$ for multi-channel coils operating in the presence of the MRI-derived head in the same way as Figs. 2.7(a-f) for the Three-sphere head, each subplot showing the currents corresponding to the Pareto-optimal arrays for $N_c = 16,\ 36,\ 64,\ \text{and}\ 100$. Consistent with the results for the Three-sphere head, increasing N_c marginally increases $\left\|\mathbf{I}^{\text{opt}}(d)\right\|$ while reducing I_{avg}. For example, an array with $N_c = 36$ and $r = 10\ \text{mm}$ requires $\left\|\mathbf{I}^{\text{opt}}(d = 24\ \text{mm})\right\| = 70\ \text{kA/}\mu\text{s}$ while an array with $N_c = 100$ and $r = 10mm$ requires 1.6 times more current, or $\left\|\mathbf{I}^{\text{opt}}(d = 24\ \text{mm})\right\| = 110\ \text{kA/}\mu\text{s}$; however, I_{avg} was reduced by a factor of 0.56. $\left\|\mathbf{I}^{\text{opt}}(d)\right\|$ greatly decreases with r. For example, an array with $N_c = 36$ and $r = 4\ \text{mm}$ requires $\left\|\mathbf{I}^{\text{opt}}(d = 24\ \text{mm})\right\| = 390\ \text{kA/}\mu\text{s}$ while an array with $N_c = 36$ and $r = 8\ \text{mm}$ requires $\left\|\mathbf{I}^{\text{opt}}(d = 24\ \text{mm})\right\| = 70\ \text{kA/}\mu\text{s}$; this is times 5.57 less $\left\|\mathbf{I}^{\text{opt}}(d)\right\|$ and since N_c is the same for both arrays I_{avg} is also 5.57 less.

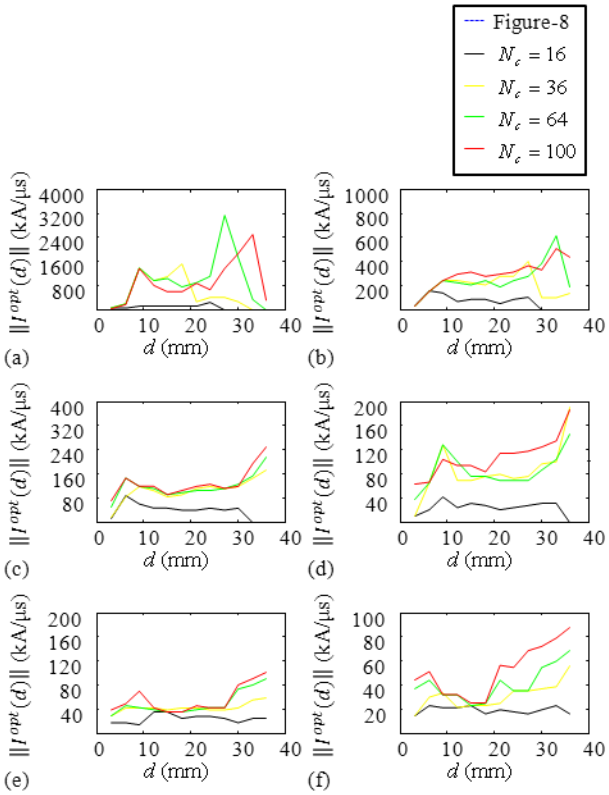

Figure 2.12 Total current required by each array driven with currents optimized for each penetration depth $\mathbf{I}^{\text{opt}}(d)$ penetration depth (i.e., $\left\|\mathbf{I}^{\text{opt}}(d)\right\|$), (a-f) Each have individual curves for each array with different number of coils N_c and each individual panel has results for arrays with coils of radius $r = 4,\ 6,\ 8,\ 10,\ 14,\ \text{and}\ 18\ \text{mm}$, respectively.Single Channel Conversion

Next, we investigate effects of converting multi-channel arrays designed for operation near the MRI-derived head into single-channel. We consider single-channel designs that are driven by an I_{sc} equal to α times the maximum of the coil driving currents of the initial multi-channel array. For all (N_c, r) combinations considered we convert multi-channel arrays along the Pareto curve $d^{\max}(v)$ for $\alpha = 3/40,\ 1/10,\ \text{and}\ 1/5$ (See Section 3.3.2).

Fig. 2.13 shows the $d_{sc}(v)$ relationship of the resulting single-channel arrays alongside the $d^{\max}(v)$ of the multi-channel arrays they derive from, and $d^{\max}_{F-8}(v)$. The $d_{sc}(v)$ and $d^{\max}(v)$ curves nearly overlap, implying that the single-channel conversion

does not deteriorate the array performance. For example, for the multi-channel array with $v^{\min}(d = 24\,\text{mm}) = 0.18\%$, the corresponding single-channel design with $\alpha = 1/10$ excites $v = 0.21\%$ or 2.62 times less volume than the optimized Figure-8 to reach the same depth.

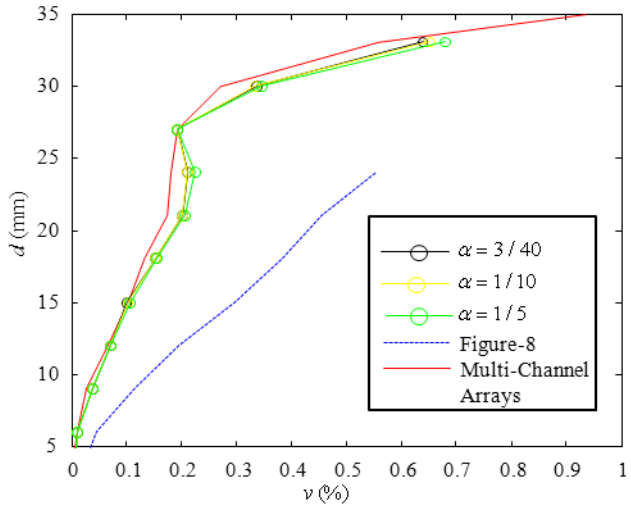

Figure 2.13 Largest depth that can be reached for a given excitation volume by multi-channel arrays ($d^{\max}(v)$), single-channel arrays ($d_{sc}(v)$) and figure-8 coils ($d_{F-8}^{\max}(v)$)

It would be advantageous to have a single-channel design that uses only a single sized loop. We therefore created a new set of designs with $\alpha = 1/100, 3/100,$ and $5/100$ and excluded the internal loop. Fig. 2.14 shows the resulting $d_{sc}(v)$ curves. As expected, the performance of these simplified single-channel arrays degrades with increasing α. However, only minor losses in performance are seen with α=3/100. For example we can reach $d = 24\,\text{mm}$ by exciting 0.265% of the head, still 2.08 times less volume than the Figure-8 coil excites to reach the same depth.

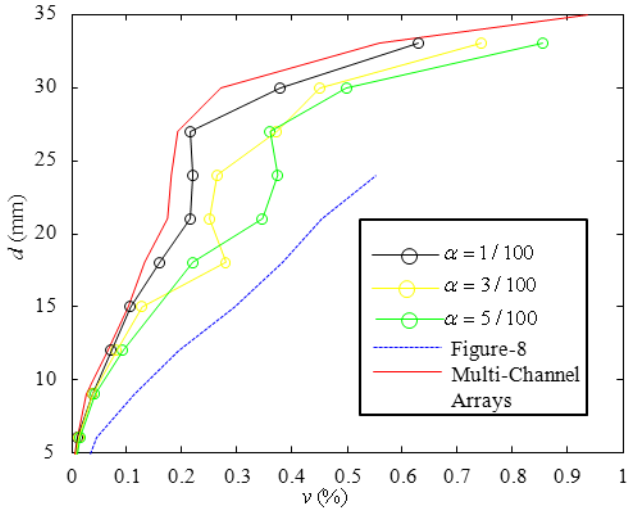

Figure 2.14 Largest depth that can be reached for a given excitation volume by multi-channel arrays ($d^{\max}(v)$), single-cannel arrays without inner loop ($d_{sc}(v)$) and figure-8 coils ($d_{F-8}^{\max}(v)$)

To verify the feasibility of the multi-channel arrays, we computed their resistances and inductances, and determined them to be comparable to those of typical commercial figure-8 coils.

2.3 Conclusions

We have presented and computationally verified a new approach for designing TMS coil arrays. First, we proposed a GA-based optimization strategy that leverages a finite difference solver to robustly determine sets of array driving currents that achieve Pareto-optimal trade-offs between field penetration depth and compactness of excitation. These multi-channel arrays can be reconfigured to stimulate a prescribed target in the brain while minimally exciting extraneous tissue. Second, we developed a simple procedure for converting multi-channel arrays into a single-channel configurations that are aimed at specific targets in the brain but otherwise operate very much like the multi-channel arrays from which they derive. The transformation from multi- to single-channel arrays is achieved by interconnecting and scaling the individual coils that make up the

original multi-channel array. Finally, we applied the proposed technique to the design of arrays composed of variable-radius circular coils that significantly outperform Figure-8 coils. The proposed technique yields TMS coil arrays that provide practitioners far greater control of the excited region than existing systems. Future designs that use spiral coils, which can be easily built on printed circuit boards, are under development.

CHAPTER 3
Uncertainty Quantification in Transcranial Magnetic Stimulation via High Dimensional Model Representation Technique

3.1 Introduction

During TMS, one or more coils located near the scalp are used to modulate brain function in targeted cortical regions. These coils produce magnetic (H) fields, electric (E) fields and eddy currents inside the conductive brain tissue. If the E-field inside a bent region of a neuron exceeds a threshold, the neuron will depolarize its membrane leading to an action potential, thus affecting brain function [1, 2]. To achieve this effect, TMS practitioners try to ensure that the E-field distribution inside a specific targeted cortical region exceeds this stimulation threshold. Although several procedures have been developed to optimally position the TMS coil over the desired cortical targets, these procedures all contain varying amounts of uncertainty, and the E-field distribution generated during TMS is highly sensitive to this uncertainty. To date, there are no adequate methods to estimate how the uncertainty in TMS setup (e.g. coil position and orientation) and the uncertainty due to individual differences in brain anatomy (e.g. conductive properties of underlying neural tissue and the size of brain) result in the uncertainty in the E-field. To ensure the E-field distribution inside a targeted cortical region above a given threshold, the dependency between E-fields and uncertainty should be accurately quantified by computational frameworks. These frameworks should be capable of providing the statistics of E-fields, given the uncertain quantities, as well as aiding the TMS practitioner to assess the sensitivity of E-fields to each uncertain

quantity. To this end, an efficient computational framework possessing these capabilities is proposed in this study.

Uncertain quantities in the TMS setup include the position [45] and the orientation [20] of TMS coils relative to targeted cortical region. TMS practitioners aim to position the coils on the scalp directly above the targeted cortical regions as the coils generate E-fields that are strongly concentrated along the centers of coils. That said, TMS coils oftentimes are not aligned just above the targeted cortical regions. For example, in depression therapy, the coils are typically placed 5-5.5 cm anterior of the location on the scalp where the coils induce a motor response in the hand ('5 cm rule') [46, 47]. However, MRI experiments have shown that when the coils are situated at the fixed location, they are not positioned directly above the targeted cortical region in 32 out of 100 instances [16]. In other TMS procedures, the practitioners often place the coils using international ten twenty electrode system [48], by which the locations on the scalp directly above cortical regions are determined using a number of cranial landmarks. Again, MRI experiments have shown that the coils are not positioned directly above the targeted cortical region in 10 out of 100 instances [49]. Aside from the errors in positioning coils due to the misidentification of the ideal coil position, TMS practitioners are known to have a precision in coil placement of 5mm [50, 51]. Therefore, a total of $2\,\mathrm{cm}$ deviation from the ideal position of the coil is expected during TMS [50, 51].

Variability in individual brain anatomy is another source of uncertainty. During TMS, the TMS coils are often oriented in such a way that the E-fields generated directly under the center of the coils point nearly perpendicular to the gyral folding patterns of the boundary between cerebrospinal fluid (CSF) and gray matter (GM) [52]. However, the specific gyral folding patterns at the targeted cortical regions vary between patients. Consequently, optimum orientation of TMS coils cannot be determined unless the practitioner has the MRI images that clearly depict the gyral structure directly under the coil. Thus, the orientation of coils relative to the underlying tissue is not prescribed for most TMS procedures and varies between TMS practitioners [50]. Note that the uncertainty in position and the orientation of TMS coils can be significantly reduced using novel 'neuro-navigated' TMS coil positioning systems that use MRI images of the

brain and robotic arms [53, 54]. However, such systems are costly and are not employed outside of research settings.

Other sources of brain anatomy differences include brain size [55] and the values of tissue conductivities [56]. There exists a 10% variation of brain size between individuals [57] and this results in a variation of the scalp-to-cortex distance [58]. For each millimeter increment of scalp-to-cortex distance, the TMS coil current has to be increased by three percent to induce the same level of brain stimulation [59]. Individual brain tissues are highly inhomogeneous and the values of tissue conductivities within the tissues can exhibit variations from 10% to 25% around their average values [60]. Unlike the uncertainty in position and orientation of coils (i.e. TMS setup), the uncertainty in brain size and the values of tissue conductivities cannot be reduced by procedural refinements.

Traditionally, the uncertainties –hereafter called random variables– in electromagnetic (EM) simulations are often quantified through Monte Carlo (MC) methods. The MC methods require the evaluation of observables (e.g. E-fields induced inside targeted cortical regions in TMS simulations) using deterministic EM simulators for many random realizations of EM system and its excitation (i.e. random values of tissue conductivities, random positions of coils in TMS simulations). These random realizations are assigned through the assumed/known probability density functions (pdfs) of random variables. The classical MC methods can be quite simply implemented and can easily provide the statistics (e.g. mean and standard deviation) of observables. However, as they usually converge very slowly [61], and only provide reasonably accurate statistical data of observables upon the execution of *a large number* of deterministic EM simulations, which is often impractical as each deterministic simulation requires significant CPU time. Recently, the classical MC method was applied to uncertainty quantification in TMS [56]; the researchers have quantified the effects of uncertainty in values of tissue conductivities on E-fields and currents induced on a MRI-derived head model. However, the accuracy of the statistics of E-fields and currents presented in paper could be improved by using more deterministic EM simulations.

To tackle with the abovementioned limitation of the MC methods, the methods leveraging generalized polynomial chaos (gPC) expansions, especially the ones based on

probabilistic collocation (PC), have been rapidly gaining traction within computational EM community. The PC methods (and related stochastic collocation methods) have recently been applied to uncertainty quantification in electromagnetic compatibility and interference [62-64], channel modeling [65-68], periodic structure [69], and EM dosimetry [70] simulations. Using the entire-domain orthogonal polynomials, the PC methods generate approximate but accurate surrogate models of observables, which are then used to obtain the means and standard deviations of observables or probed via classical MC methods to extract their pdfs. The PC methods obtain the coefficients of gPC expansions via efficient multidimensional integration rules. They are non-intrusive; they can use existing deterministic EM simulators to obtain the observable values at collocation/integration points dictated by the multidimensional integration rules. These methods converge rapidly for the observables that vary smoothly across the domain of random variables, i.e. random domain [71]. However, they tend to be inefficient and inaccurate for the observables that vary rapidly throughout the random domain [72]. To address this shortcoming, a multi-element probabilistic collocation (ME-PC) method has been developed as an *h*-adaptive refinement extension to PC methods [72]. This method achieves its accuracy and efficiency by adaptively and recursively dividing the random domain into subdomains and generating separate local gPC expansion for each subdomain. That said, the ME-PC generated surrogate models often lack accuracy when the number of random variables is large [73]. To address this concern, the ME-PC method has been used in conjunction with high dimensional model representation (HDMR) expansions for surrogate model generation [73].

This chapter elucidates a computational framework for uncertainty quantification in TMS simulations. The computational framework leverages the HDMR expansions to generate the surrogate models of observables via finite sums of component functions that represent individual and combined contributions of random variables to the observables [74]. The HDMR expansions are constructed iteratively by including the component functions pertinent to the "most important" random variables, reducing the cost of surrogate model generation dramatically [75-83]. The component functions included in HDMR expansions are approximated by the ME-PC method, which effectively tailors the collocation/integration points used for polynomial approximations to the component

functions. The observable values at collocation/integration points identified by the ME-PC method are computed using a quasi-static finite difference (FD) solver. Upon the generation of accurate surrogate models, the classical MC method is used to compute the statistics of observables while accounting for the pdfs of random variables. The accuracy and efficiency of the proposed computational framework are demonstrated via its applications to statistical characterization of E-fields induced inside a three-sphere head model and a cortical region of a MRI-derived head model targeted during TMS therapy.

3.2 Formulation

Let $\mathbf{x}=\left[x^1,x^2,...,x^{N_{\text{dof}}-1},x^{N_{\text{dof}}}\right]$ denote an N_{dof}-dimensional random vector defined over a random domain $D=\prod_{i=1}^{N_{\text{dof}}}D^i$; each element of $\mathbf{x}$, i.e. x^i, $i=1,\ldots,N_{\text{dof}}$, is a random variable that parameterizes one uncertain quantity in the TMS setup or one uncertain quantity related to patient-to-patient differences. Each random variable, x^i, $i=1,\ldots,N_{\text{dof}}$, is assumed to be mutually independent and distributed with a known/assumed pdf, $w^i(\cdot)$, across a finite one dimensional random domain $D^i=\left[a^i,b^i\right]$. Let $V(\mathbf{x})$ represent an observable (e.g., the E-field on a single point in targeted cortical region) which is typically a complicated function of $\mathbf{x}$ and can only be evaluated by a deterministic simulator.

The proposed computational framework leverages the HDMR technique to obtain statistics of $V(\mathbf{x})$. Specifically, the HDMR technique is used to generate approximate but accurate surrogate model of $V(\mathbf{x})$. To do that, the technique decomposes N_{dof}-variate observable, $V(\mathbf{x})$, into lower dimensional component functions and approximates each component function via the ME-PC method described in [72, 84, 85]. While iteratively constructing the HDMR expansion, the technique automatically selects the component functions pertinent to most significant random variables and thereby reduces the cost of surrogate model generation substantially [75-83]. Upon the generation of an accurate

surrogate model, the MC method that accounts for the distributions $w^i(\cdot)$, $i=1,\ldots,N_{\text{dof}}$, is used to probe the surrogate model and to obtain the statistics of $V(\mathbf{x})$.

3.2.1 The HDMR Technique:

The HDMR expansion approximates to $V(\mathbf{x})$ in terms of component functions as

$$V(\mathbf{x}) = \sum_{\mathbf{u}\subseteq\Omega} V_{\mathbf{u}}\left(\mathbf{x}^{\mathbf{u}}\right), \tag{3.1}$$

where $\Omega=\{1,\ldots,N_{\text{dof}}\}$ is the set of random variable indices, $\mathbf{u}$ is a subset of Ω, i.e. $\mathbf{u}\subseteq\Omega$, and $|\mathbf{u}|$ denotes the cardinality of subset $\mathbf{u}$. $\mathbf{x}^{\mathbf{u}}$ is a $|\mathbf{u}|$-dimensional random vector and $V_{\mathbf{u}}\left(\mathbf{x}^{\mathbf{u}}\right)$ represents the component functions defined over D. For example, for $\mathbf{u}=\varnothing$, $V_{\mathbf{u}}\left(\mathbf{x}^{\mathbf{u}}\right)=V_{\varnothing}\left(x^{\varnothing}\right)=V_0$ is the zeroth-order component function which is constant over D. For $\mathbf{u}=\{1\}$, $V_{\mathbf{u}}\left(\mathbf{x}^{\mathbf{u}}\right)=V_1\left(x^1\right)$ is the first-order component function that represents the individual contribution of x^1 to $V(\mathbf{x})$, and for $\mathbf{u}=\{1,2,4\}$, $V_{\mathbf{u}}\left(\mathbf{x}^{\mathbf{u}}\right)=V_{124}\left(x^1,x^2,x^4\right)$ is the third-order component function that describes the combined contribution of x^1, x^2, and x^4 to $V(\mathbf{x})$. The HDMR expansion in (3.1) can be perhaps best described by an example. Assume that $N_{\text{dof}}=3$ and $\Omega=\{1,2,3\}$. All possible subsets of Ω, $\mathbf{u}$, their cardinalities $|\mathbf{u}|$, and all component functions $V_{\mathbf{u}}\left(\mathbf{x}^{\mathbf{u}}\right)$ corresponding to these possible subsets are

$$\begin{array}{lll}
\mathbf{u}=\varnothing, & |\mathbf{u}|=0, & V_0 \\
\mathbf{u}=\{1\}, & |\mathbf{u}|=1, & V_1(x^1) \\
\mathbf{u}=\{2\}, & |\mathbf{u}|=1, & V_2(x^2) \\
\mathbf{u}=\{3\}, & |\mathbf{u}|=1, & V_3(x^3) \\
\mathbf{u}=\{1,2\}, & |\mathbf{u}|=2, & V_{12}(x^1,x^2) \\
\mathbf{u}=\{1,3\}, & |\mathbf{u}|=2, & V_{13}(x^1,x^3) \\
\mathbf{u}=\{2,3\}, & |\mathbf{u}|=2, & V_{23}(x^2,x^3) \\
\mathbf{u}=\{1,2,3\}, & |\mathbf{u}|=3, & V_{123}(x^1,x^2,x^3).
\end{array} \tag{3.2}$$

Using the component functions in (3.2), the HDMR expansion can be constructed as

$$V(\mathbf{x}) = V_0 + V_1\left(x^1\right) + V_2\left(x^2\right) + V_3\left(x^3\right) + V_{12}\left(x^1, x^2\right) + V_{13}\left(x^1, x^3\right) + V_{23}\left(x^2, x^3\right) + V_{123}\left(x^1, x^2, x^3\right). \tag{3.3}$$

The advantage of such construction can be illustrated by selecting an observable that consists of a constant term and monomials, i.e., $V(\mathbf{x}) = 1 + \left(x^1\right)^2 + \left(x^2\right)^2 + \left(x^3\right)^2$ (Note: the indices of random variables are written inside the parentheses while their powers are intentionally left outside the parentheses to avoid confusion). The component functions V_0, $V_1\left(x^1\right)$, $V_2\left(x^2\right)$, and $V_3\left(x^3\right)$ in (3.3) are equally significant and needed to approximate $V(\mathbf{x})$ while the remaining ones in (3.3) are redundant. Just like in this example, many physical observables in real-world can be approximated by low order component functions [73]. And this fact renders the HDMR expansion highly suitable for surrogate model generation of $V(\mathbf{x})$ in high-dimensional random domains as only the surrogate models in low dimensional random domains are constructed. Depending on the way of obtaining component functions $V_{\mathbf{u}}\left(\mathbf{x}^{\mathbf{u}}\right)$, $\mathbf{u} \subseteq \Omega$, two different types of HDMR techniques are proposed in literature: the analysis of variance HDMR and CUT-HDMR. The former is not suitable for surrogate model generation in high-dimensional random domains (see the discussion in [75]) and hence is out of the scope of this paper. The latter, CUT-HDMR technique, obtains $V_{\mathbf{u}}\left(\mathbf{x}^{\mathbf{u}}\right)$, $\mathbf{u} \subseteq \Omega$, using the observable values on lines, planes, and hyperplanes, i.e. cuts, passing through a reference point, $\bar{\mathbf{x}}$, in D, i.e.

$$V_{\mathbf{u}}\left(\mathbf{x}^{\mathbf{u}}\right) = V\left(\mathbf{x}^{\mathbf{u}}\right)\Big|_{\mathbf{x}=\bar{\mathbf{x}}\setminus\mathbf{x}^{\mathbf{u}}} - \sum_{\mathbf{v}\subset\mathbf{u}} V_{\mathbf{v}}\left(\mathbf{x}^{\mathbf{v}}\right), \tag{3.4}$$

where $\mathbf{x} = \bar{\mathbf{x}} \setminus \mathbf{x}^{\mathbf{u}}$ indicates that the random variables with indices that do not belong to subset $\mathbf{u}$ are set to their corresponding values at reference point $\bar{\mathbf{x}}$. Typically, $\bar{\mathbf{x}}$ is set to the mass center of D, i.e., $\bar{\mathbf{x}} = [\bar{x}^1, \ldots, \bar{x}^{N_{\text{dof}}}] = [(a^1 + b^1)/2, \ldots, (a^{N_{\text{dof}}} + b^{N_{\text{dof}}})/2]$. For the above given example, $V_{\mathbf{u}}\left(\mathbf{x}^{\mathbf{u}}\right)$, $\mathbf{u} \subseteq \Omega$, obtained by CUT-HDMR technique are

$$
\begin{aligned}
&\mathbf{u}=\varnothing, && V_0 = V\left(\bar{\mathbf{x}}\right)\\
&\mathbf{u}=\{1\}, && V_1\left(x^1\right) = V\left(x^1,\bar{x}^2,\bar{x}^3\right) - V_0\\
&\mathbf{u}=\{2\}, && V_2\left(x^2\right) = V\left(\bar{x}^1,x^2,\bar{x}^3\right) - V_0\\
&\mathbf{u}=\{3\}, && V_3\left(x^3\right) = V\left(\bar{x}^1,\bar{x}^2,x^3\right) - V_0\\
&\mathbf{u}=\{1,2\}, && V_{12}\left(x^1,x^2\right) = V\left(x^1,x^2,\bar{x}^3\right) - V_0 - V_1\left(x^1\right) - V_2\left(x^2\right)\\
&\mathbf{u}=\{1,3\}, && V_{13}\left(x^1,x^3\right) = V\left(x^1,\bar{x}^2,x^3\right) - V_0 - V_1\left(x^1\right) - V_3\left(x^3\right)\\
&\mathbf{u}=\{2,3\}, && V_{23}\left(x^2,x^3\right) = V\left(\bar{x}^1,x^2,x^3\right) - V_0 - V_2\left(x^2\right) - V_3\left(x^3\right)\\
&\mathbf{u}=\{1,2,3\}, && V_{123}\left(x^1,x^2,x^3\right) = V\left(x^1,x^2,x^3\right) - V_{12}\left(x^1,x^2\right) - V_{13}\left(x^1,x^3\right) - V_{23}\left(x^2,x^3\right)\\
& && \qquad - V_1\left(x^1\right) - V_2\left(x^2\right) - V_3\left(x^3\right) - V_0.
\end{aligned}
\tag{3.5}
$$

In CUT-HDMR technique, the surrogate model of $V(\mathbf{x})$ can be generated by interpolating $V_{\mathbf{u}}\left(\mathbf{x}^{\mathbf{u}}\right)$, $\mathbf{u}\subseteq\Omega$, either directly from the component function with the highest cardinality or recursively starting from the component function with the lowest cardinality. The former strategy is efficient if significant/redundant component functions are known a priori. However, as that information is not available for many physical observables, the latter strategy is often employed. In latter strategy, the observable value on reference point $\bar{\mathbf{x}}$ (for $|\mathbf{u}|=0$) is computed first and then the observable values on lines (for $|\mathbf{u}|=1$), planes (for $|\mathbf{u}|=2$), and hyperplanes (for $|\mathbf{u}|\geq 3$) passing through $\bar{\mathbf{x}}$ are interpolated consecutively using the ME-PC method. While in principle any multivariate interpolator could be used to interpolate observable values, the ME-PC method is especially useful as it effectively tailors the polynomial bases on cuts by adaptively and recursively dividing the cut into small elements and generating separate low order gPC polynomial approximation to $V(\mathbf{x})$ on each small element. While obtaining the coefficients of each low order gPC expansion on each small element, the method uses the quasi-static FD simulator to obtain $V(\mathbf{x})$ on collocation/integration points dictated by the selected multidimensional integration rule. The reader is referred to [72, 84, 85] for details of the ME-PC method.

3.2.2 The Iterative HDMR Technique:

The efficiency of HDMR technique directly depends on the number of component functions in HDMR expansion as the total number of possible component functions scales with $\sum_{j=0}^{|\mathbf{u}|} N_{\text{dof}}!/(j!(N_{\text{dof}}-j)!)$ (i.e. increases rapidly with increasing N_{dof}). This high cost of HDMR technique for large N_{dof} is substantially reduced by integrating an iterative scheme to the technique, which automatically selects random variables that significantly contribute to $V(\mathbf{x})$ and iteratively includes the higher-order component functions pertinent to these variables in the HDMR expansion. The iterative scheme starts by computing the weights associated with the first-order component functions as [75]

$$\zeta_{\mathbf{u}} = \left| E\left[V_{\mathbf{u}}\left(\mathbf{x}^{\mathbf{u}}\right)\right] / V_0 \right|; \quad |\mathbf{u}| = 1. \tag{3.6}$$

The weights $\zeta_{\mathbf{u}}$ are measures of the contributions of first-order component functions' means, i.e. $E[V_{\mathbf{u}}(\mathbf{x}^{\mathbf{u}})] = \int V_{\mathbf{u}}(\mathbf{x}^{\mathbf{u}}) d\mathbf{x}^{\mathbf{u}}$, to the mean of $V(\mathbf{x})$ computed via constant zeroth-order component function (Note: in case V_0 is equal to zero, the weights are directly set to $E[V_{\mathbf{u}}(\mathbf{x}^{\mathbf{u}})]$). If $\zeta_{\mathbf{u}}$ is larger than a prescribed tolerance ε_1, then the component function is assumed to contribute significantly to $V(\mathbf{x})$. The indices of random variables pertinent to these significant component functions are stored in the index set Ω. The second-order component functions involving these significant random variables are marked as candidates for constructing the HDMR expansion at the second level; they are only added to the expansion if their weights are larger than ε_1. This scheme is repeated in an iterative manner for all levels. For example, assume that the indices of the significant random variables are found to be $\{1,2,4\}$. Then, the second-order component functions with indices $\{1,2\}$, $\{1,4\}$, and $\{2,4\}$ are considered to be included in the HDMR expansion at the second level. At the end of second level, assume that *any* of second-order component functions with indices $\{1,2\}$, $\{1,4\}$, and $\{2,4\}$ is found to be insignificant. Then none of third order component functions is considered to be included in the HDMR expansion since *all* second order component functions with indices that are the subsets of the index set of a candidate third-order component function should be identified as significant. On

the other hand, assume that second-order component functions with indices $\{1,2\}$, $\{1,4\}$, and $\{2,4\}$ are *all* found to be significant. Then, the third order component function with index $\{1,2,4\}$ is considered to be included in the HDMR expansion at the third level. Note that at the higher levels, the weights of the component functions $V_{\mathbf{u}}\left(x^{\mathbf{u}}\right)$, $|\mathbf{u}|\geq 2$ are computed by [75]

$$\zeta_{\mathbf{u}}=\left|E\left[\ V_{\mathbf{u}}\left(\mathbf{x}^{\mathbf{u}}\right)\right]\right|\Big/\left|\sum_{|\mathbf{v}|<|\mathbf{u}|-1}E\left[\ V_{\mathbf{v}}\left(\mathbf{x}^{\mathbf{v}}\right)\right]\right|;\ \ |\mathbf{u}|\geq 2\,. \tag{3.7}$$

To provide an additional stopping criterion, the decay rate of relative difference between observable means computed at two consecutive levels is defined as [75]

$$\kappa=\left|\sum_{|\mathbf{v}|<|\mathbf{u}|}E\left[\ V_{\mathbf{v}}\left(\mathbf{x}^{\mathbf{v}}\right)\right]-\sum_{|\mathbf{v}|<|\mathbf{u}|-1}E\left[\ V_{\mathbf{v}}\left(\mathbf{x}^{\mathbf{v}}\right)\right]\right|\Big/\left|\sum_{|\mathbf{v}|<|\mathbf{u}|-1}E\left[\ V_{\mathbf{v}}\left(\mathbf{x}^{\mathbf{v}}\right)\right]\right|. \tag{3.8}$$

If κ is smaller than a prescribed tolerance ε_2, then the HDMR expansion is assumed to have converged. Once the iterative construction is completed, the component functions identified as insignificant are also included in the expansion to increase the accuracy of surrogate model since they are already computed during iterative procedure. Upon accurate generation of surrogate model of $V(\mathbf{x})$, the statistical moments of surrogate model of $V(\mathbf{x})$, an approximation to those of $V(\mathbf{x})$, can be obtained from its MC samples. In addition, when $w^i(\cdot)$, $i=1,\ldots,N_{\text{dof}}$, represent uniform distributions, the mean of $V(\mathbf{x})$ can directly be computed by [75]

$$E\left[V(\mathbf{x})\right]=\sum_{\mathbf{u}\subseteq\Omega}E\left[\ V_{\mathbf{u}}\left(\mathbf{x}^{\mathbf{u}}\right)\right]. \tag{3.9}$$

Similarly, the variance of $V(\mathbf{x})$ can be calculated using [75]

$$\text{var}\left[V(\mathbf{x})\right]=\sum_{\mathbf{u}\subseteq\Omega}\text{var}\left[\ V_{\mathbf{u}}\left(\mathbf{x}^{\mathbf{u}}\right)\right], \tag{3.10}$$

where $\text{var}[V_{\mathbf{u}}(\mathbf{x}^{\mathbf{u}})]=E[(V_{\mathbf{u}}(\mathbf{x}^{\mathbf{u}}))^2]-(E[V_{\mathbf{u}}(\mathbf{x}^{\mathbf{u}})])^2$.

3.2.3 The Quasi-Static FD Simulator

To approximate each component function, the observable values at integration/collocation points required by the ME-PC method are computed using a quasi-static FD simulator. This simulator outputs the magnitudes of E-fields induced at N_{obs} points $\mathbf{r}_n$, $n=1,\ldots,N_{\text{obs}}$, selected on the head model (i.e. $E(\mathbf{r}_n)=\sqrt{E_x(\mathbf{r}_n)^2+E_y(\mathbf{r}_n)^2+E_z(\mathbf{r}_n)^2}$). The E-fields are generated by TMS coils driven with a time varying current $p(t)$ with maximum frequency in the 1-10 kHz range. Therefore, the electric and magnetic fields induced at $\mathbf{r}_n$ are actually time varying. However, because of the frequency range of $p(t)$, the following quasi-static assumptions are valid: (i) inductive coupling involving Eddy and displacement currents generated inside the brain are neglected, and (ii) the time variation of B- and E- fields is proportional to the current pulse and its time derivative, respectively, i.e. $\mathbf{B}(\mathbf{r}_n,t)=\mathbf{B}(\mathbf{r}_n)\,p(t)$, and $\mathbf{E}(\mathbf{r}_n,t)=\mathbf{E}(\mathbf{r}_n)\,dp(t)/dt$. Consequently, the quasi-static FD simulator determines the E-field per unit $dp(t)/dt$ (i.e. $\mathbf{E}(\mathbf{r}_n)$) generated during TMS (see [36] for more information about quasi-static FD simulator).

3.3 Numerical results and discussion

This section illustrates the application of the proposed computational framework to the calculation of means and standard deviations of TMS-induced E-fields inside three-sphere and realistic MRI-derived head models. Unless specified otherwise, an iterative HDMR technique with $\varepsilon_1=10^{-4}$ and $\varepsilon_2=10^{-16}$ is used to construct the HDMR expansions that define $V(\mathbf{x})$'s surrogate models. Also, the random variables are assumed uniformly distributed within specified ranges and the means and standard deviations (i.e., square roots of the variance) of $V(\mathbf{x})$ are computed using (3.9) and (3.10). The observables are the magnitudes of E-fields, $V_n(\mathbf{x})=E(\mathbf{r}_n,\mathbf{x})$, $n=1,\ldots,N_{\text{obs}}$, computed at N_{obs} points selected in the head models. The average error in the surrogate models of the E-fields' magnitudes is computed using

$$err = \frac{1}{N_{\text{obs}}} \sum_{n=1}^{N_{\text{obs}}} \sqrt{\sum_{i=1}^{160} \left(V_n^{\text{s}}\left(\mathbf{x}_i\right) - V_n\left(\mathbf{x}_i\right) \right)^2 \Big/ \sum_{i=1}^{160} V_n\left(\mathbf{x}_i\right)^2} \tag{3.11}$$

where $\mathbf{x}_i$ is the randomly chosen evaluation point and $V_n^{\text{s}}\left(\mathbf{x}_i\right)$ is the approximate observable value at $\mathbf{x}_i$ probed from the surrogate model of the E-field's magnitude at the n^{th} point selected in the head model. In what follows, $\mathbf{x}$ with dot(s) represents a random vector of random variables with indices belonging to $\mathbf{u} \subsetneq \Omega = \{1, \ldots, N_{\text{dof}}\}$; the random variables with indices not belonging to $\mathbf{u}$ are set to their corresponding mean values.

3.3.1 Three-Sphere Head Model

The proposed method is applied to statistically characterize E-field magnitudes inside a three-sphere head model formed by three concentric spheres with radii of 8.0, 8.5, and $9.2\,\text{cm}$ and centered about the origin of global coordinate system Fig. 3.1(a). From innermost to outermost, the layers in head model represent the brain, the skull, and the skin tissues Fig. 3.1(a). The head model is excited by a Figure-8 coil [3] centered at $(0, 0, 10.2)\,\text{cm}$ that consists of two filamentary circular loops with radii of $2.3\,\text{cm}$; each loop is positioned perpendicular to the z- axis and driven with a current varying at a rate of $1.368\,\text{A/ns}$.

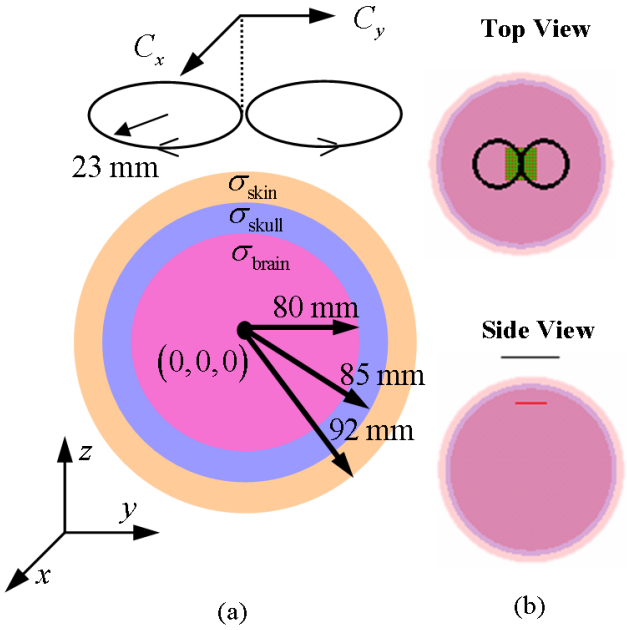

Figure 3.1 (a) Three-sphere head model with the Figure-8 coil positioned 1 cm above the head and centered about the z-axis. (b) The statistics of E-fields' magnitudes are obtained on a Cartesian grid (indicated with red points on a green square plane in top view).

Five parameters characterize the uncertainty in the head model and TMS setup ($N_{\text{dof}}=5$): the conductivity of the brain σ_{brain}, the conductivity of the skull σ_{skull}, the conductivity of the skin σ_{skin}, the position of Figure-8 coil along the x-direction C_x, and the position of the Figure-8 coil along the y-direction C_y (i.e., $\mathbf{x}=\left[\sigma_{\text{brain}},\sigma_{\text{skull}},\sigma_{\text{skin}},C_x,C_y\right]$). All five random variables are assumed to be uniformly distributed in ranges $\left[a^i,b^i\right]$, $i=1,\ldots,5$; a^i and b^i are given in Table 3.1. (Note: the means of the random variables pertinent to the tissues' conductivities in Table 3.1, i.e. $\bar{x}^i$, $i=1,\ldots,3$, correspond to the values of tissues' conductivities of the three-sphere model in [38]). The observables are the magnitudes of E-fields computed at 121 points ($N_{\text{obs}}=121$) selected on a Cartesian grid that is centered at $(0,0,0.65)$ and positioned perpendicular to the z-axis; the points are situated $0.3\,\text{cm}$ apart from each other [Fig. 3.1(b)]. Surrogate models of all observables $V_n^s(\mathbf{x})$, $n=1,\ldots,121$ are obtained using the proposed method, requiring 680 deterministic FD simulations and $err=2.16\times10^{-4}$. Using

the surrogate models, the means and standard deviations of $V_n(\mathbf{x})$, $n=1,\ldots,121$, are computed [Figs. 3.2 (a)-(b)]. To separately assess the sensitivity of the E-field magnitudes to uncertain quantities in TMS setup and uncertain quantities related to brain anatomy, two types of data are extracted from the surrogate models. First, the random variables are restricted to the coil parameters, i.e. $\dot{\mathbf{x}}=\left[C_x, C_y\right]$, and the means and standard deviations of $V_n(\dot{\mathbf{x}})$ are computed [Figs. 3.2 (c)-(d)]. Second, the random variables are limited to the tissue conductivities, i.e. $\ddot{\mathbf{x}}=\left[\sigma_{\text{brain}}, \sigma_{\text{skull}}, \sigma_{\text{skin}}\right]$, and the means and standard deviations of $V_n(\ddot{\mathbf{x}})$ are computed [Figs. 3.2(e)-(f)].

	a^i	b^i	$\bar{x}^i$
$i=1$, σ_{brain} (S/m)	0.3825	0.5175	0.4500
$i=2$, σ_{skull} (S/m)	0.0425	0.0575	0.0500
$i=3$, σ_{skin} (S/m)	0.3825	0.5175	0.4500
$i=4$, C_x (cm)	–1.0	1.0	0.0
$i=5$, C_y (cm)	–1.0	1.0	0.0

Table 3.1 The Values of a^i, b^i, and $\bar{x}^i$, $i=1,\ldots,5$ (for the Three-Sphere Head Model Scenario)

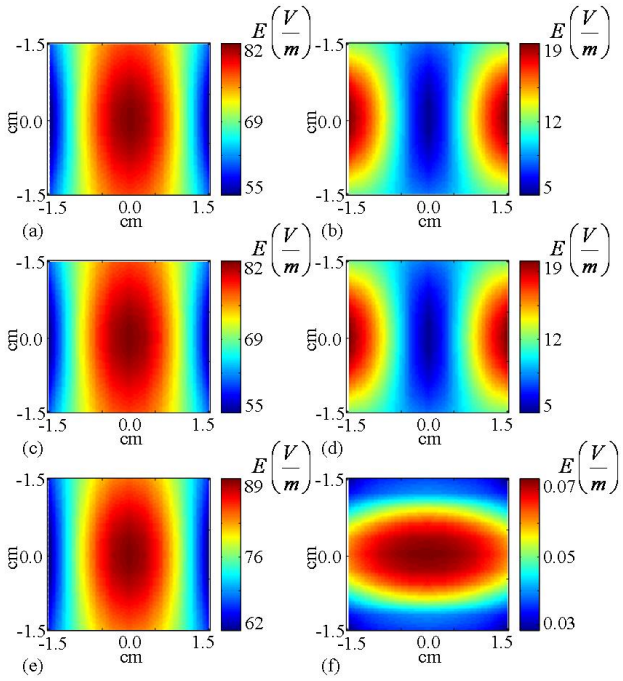

Figure 3.2 The statistical moments of the E-fields' magnitudes on points selected on a Cartesian grid: (a) the means and (b) standard deviations of $V_n(\mathbf{x})$, (c) the means and

(d) standard deviations of $V_n(\dot{\mathbf{x}})$, and (e) the means and (f) standard deviations of $V_n(\ddot{\mathbf{x}})$.

Several observations about the results in Figs. 3.2(a)-(f) are in order:

The results in Figs. 3.2(a)-(b) appear very similar to those in Figs. 3.2(b)-(d), respectively. This implies that uncertainty in the coil position significantly affects the induced E-fields.

In Figs. 3.2(a) and (c), the means of the E-fields on points near the center of the grid, i.e. right below the coil, are larger than those on points near to the (left and right) edges of the grid. This is not surprising since points right below the coil are closer to the coil than the points near the edges of grid. In Figs. 3.2(b) and (d), the standard deviations of the E-fields on points near the (left and right) edges of the grid are larger than those on points closer to the center since the distance from the center of the coil to the edges of the grid exhibits a larger variation than that of points near the center of the grid.

The maximum standard deviation of $V_n(\ddot{\mathbf{x}})$ [Fig. 3.2(f)] is 80 times smaller than the minimum standard deviation of $V_n(\mathbf{x})$ [Fig. 3.2(b)]. Hence, it is concluded that uncertainty in values of tissue conductivities do not significantly affect the induced E-fields.

3.3.2 MRI-Derived Realistic Head Model

Next, the proposed computational framework is used to estimate the statistics of E-field magnitudes induced inside MRI-derived realistic head models, each of which contains skin, skull, CSF, GM, and white matter (WM) tissues [Fig. 3.3]. The head models were derived from an MRI image of a male subject's head obtained using a 3T GE Signa scanner (Waukesha, WI) that generated an IR-prepped, 3D, SPGR pulse sequence (TR=9.03, TE = 1.84, TI = 500 ms, FOV = 24 cm, slice thickness = 1.2 mm, number of voxels = $256\times256\times124$). The MRI image was segmented into GM, WM, and ventricular CSF using the SPM5 segmentation toolbox available in [49]. The remaining unclassified tissue was further partitioned into bone, muscle, and CSF, using FAST component of the image analysis package available in [50] [Fig. 3.3]. The head models are obtained by (i) shrinking the GM and WM tissues in size by a shrink factor sf, (ii)

adding CSF to the displaced volume, (iii) assigning conductivities to the segmented images of skin σ_{skin}, skull σ_{skull}, CSF σ_{CSF}, GM σ_{GM}, and WM σ_{WM}, respectively, (iv) and assigning a conductivity to each voxel equal to the average conductivities of tissues inside it [Fig. 3.3]. For each head model, a global Talairach coordinate system is defined [86]. The model is excited by a (simulated) Medtronic MC-B70 Figure-8 coil (P/N 9790) [45] [Fig. 3.4] consisting of two spiral wings, each of which has 10 wire turns and inner/outer radii of $12\,\text{mm}/54\,\text{mm}$, and is driven by a current varying at a rate of $0.171\,\text{A/ns}$. The left and right windings are bent by angles of 18.5° and 16°, respectively, and positioned $5\,\text{mm}$ away from one another (measured at the center of the coil) [Fig. 3.4]. The coil is centered at $\mathbf{r}_{\text{coil}} = C_x\hat{\mathbf{x}}' + C_y\hat{\mathbf{y}}' + \mathbf{r}_{\text{cen}}$, where C_x and C_y represent the coil position along x'- and y'- directions defined along orthonormal vectors $\hat{\mathbf{x}}'$ and $\hat{\mathbf{y}}'$, respectively; $\mathbf{r}_{\text{cen}}$ is defined as the origin of the local coordinate system (i.e., the nominal position of the coil center in the global Talairach coordinate system) [Fig. 3.5]. The coil is rotated by angle θ defined between the line joining the centers of the wings and the $\hat{\mathbf{x}}'$ unit vector [Fig. 5]; the line joining the centers of the wings is parallel to the $\hat{\mathbf{x}}'$ and $\hat{\mathbf{y}}'$ unit vectors when $\theta = 0°$ and $\theta = 90°$, respectively [Fig. 3.5]. (Note: parameters for variations of specific gyral folding patterns between individuals' brains are not available and, thus, the effects of uncertainty in the gyral folds on the TMS-induced E-fields are not quantified in this study.)

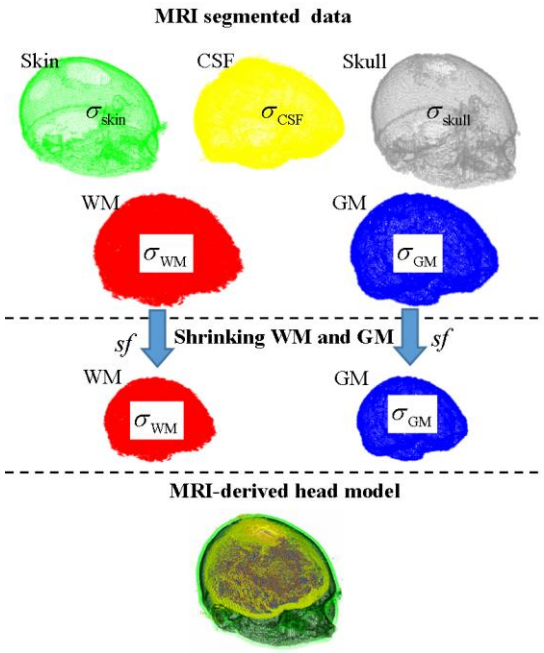

Figure 3.3 Realistic head model generation procedure: (i) Conductivity values are assigned to the segmented images of the skin (green) CSF (yellow), skull (gray), WM (red), and GM (blue). (ii) The WM and GM are shrunk and the displaced volume is replaced with CSF. (iii) The images are combined to generate an MRI-derived head model.

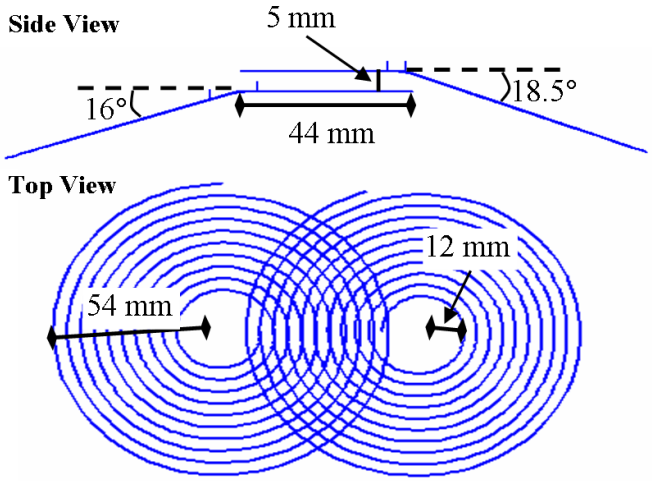

Figure 3.4 The configuration of Medtronic MC-B70 Figure-8 coil (P/N 9790).

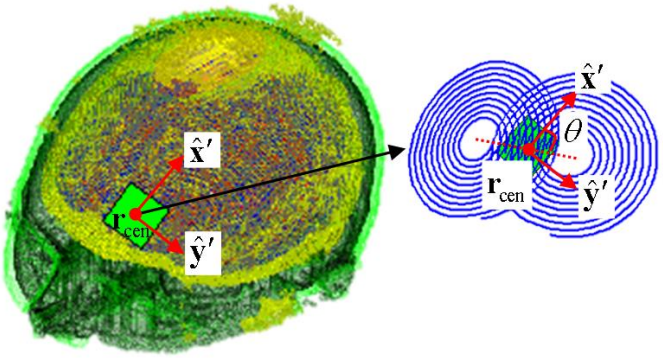

Figure 3.5 The coil is positioned along x' and y' directions defined along $\hat{\mathbf{x}}'$ and $\hat{\mathbf{y}}'$ unit vectors in local coordinate system. The coil is rotated with θ angle defined between the line connecting the centers of wings (indicated with dotted red line) and $\hat{\mathbf{x}}'$ unit vector.

Nine parameters characterize the uncertainty in the head model and TMS setup ($N_{\text{dof}}=9$): $\mathbf{x}=\left[\sigma_{\text{skin}},\sigma_{\text{skull}},\sigma_{\text{CSF}},\sigma_{\text{WM}},\sigma_{\text{GM}},sf,C_x,C_y,\theta\right]$. All random variables are assumed uniformly distributed in ranges $\left[a^i,b^i\right]$, $i=1,\ldots,9$; a^i and b^i are given in Table 3.2. (Note: the means of random variables pertinent to the tissues' conductivities in Table 3.2, i.e. $\bar{x}^i$, $i=1,\ldots,5$, correspond to the values of these tissues' conductivities in [18].) The observables are the magnitudes of the E-fields at the centers of voxels which have GM inside and are inside a hexahedral region (with dimensions of $4.56\times5.16\times8.28\,\text{cm}$) centered at $(-3.66,3.72,0.9)\,\text{cm}$ (in the Talairach coordinate system) [Fig. 3.6]. The total number of voxels inside the hexahedral region that sit in the GM is $N_{\text{obs}}=24{,}642$. The surrogate models of all observables $V_n^s(\mathbf{x})$, $n=1,\ldots,24{,}642$ are obtained using the proposed method, required $1{,}416$ deterministic simulations and $err=3.32\times10^{-2}$. Using the surrogate models, the means and standard deviations of $V_n(\mathbf{x})$, $n=1,\ldots,24{,}642$ are computed [Figs. 3.7(a)-(b)].

	a^i	b^i	$\bar{x}^i$
$i=1$, σ_{skin} (S/m)	0.3952	0.5348	0.4650
$i=2$, σ_{skull} (S/m)	0.0085	0.0115	0.0100
$i=3$, σ_{CSF} (S/m)	1.3073	1.7687	1.5380

$i=4$, σ_{WM} (S/m)	0.1131	0.1530	0.1331
$i=5$, σ_{GM} (S/m)	0.3400	0.4600	0.4000
$i=6$, sf	0.0	0.1	0.05
$i=7$, C_x (cm)	–1.0	1.0	0.0
$i=8$, C_y (cm)	–1.0	1.0	0.0
$i=9$, θ (°)	0	90	45

Table 3.2 The Values of a^i, b^i, and $\bar{x}^i$, $i=1,\ldots,9$ (for the MRI-Derived Head Model Scenario)

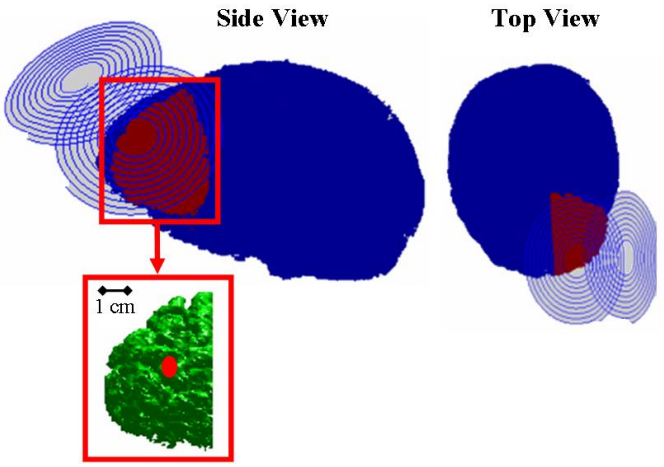

Figure 3.6 The statistics of E-fields' magnitudes are obtained at centers of voxels inside a targeted hexahedral region (indicated as the red region in an MRI-derived head model); each voxel has GM inside. The red dot on targeted region indicates targeted point.

1) Combined Effects of Uncertain Quantities to the E-fields: To separately observe the combined effects of random variables pertinent to the TMS setup and the combined effects of random variables related to brain anatomy on E-fields' magnitudes, two types of data are extracted from the surrogate models. First, the random variables are restricted to the coil parameters, i.e. $\dot{\mathbf{x}}=\left[C_x, C_y, \theta\right]$, and the means and standard deviations of $V_n(\dot{\mathbf{x}})$ are computed [Figs. 3.7(c)-(d)]. Second, the random variables are limited to the quantities related to brain anatomy, i.e. $\ddot{\mathbf{x}}=\left[\sigma_{\text{skin}}, \sigma_{\text{skull}}, \sigma_{\text{CSF}}, \sigma_{\text{WM}}, \sigma_{\text{GM}}, sf\right]$, and the means and standard deviations of $V_n(\ddot{\mathbf{x}})$ are computed [Figs. 3.7(e)-(f)]. (Note: the random variables in each case are indicated in Table 3.3).

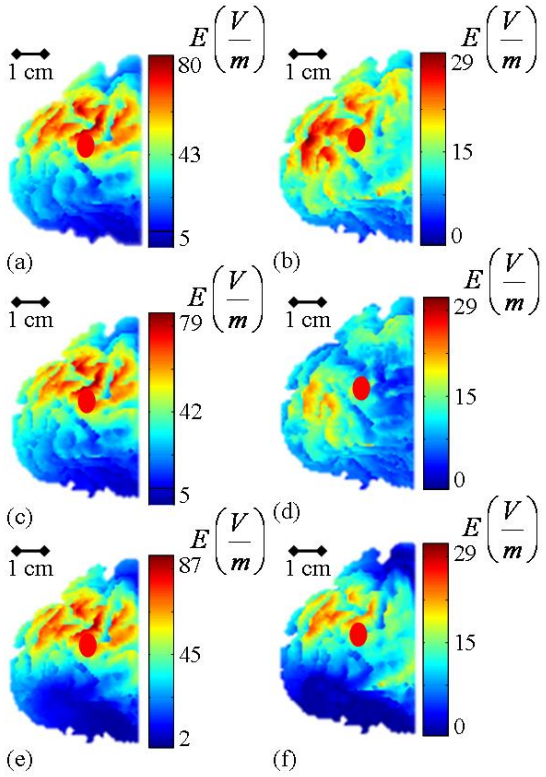

Figure 3.7 The statistical moments of the E-fields' magnitudes at centers of voxels: (a) the means and (b) standard deviations of $V_n(\mathbf{x})$, (c) the means and (d) standard deviations of $V_n(\dot{\mathbf{x}})$, and (e) the means and (f) standard deviations of $V_n(\ddot{\mathbf{x}})$. The red dot indicates the targeted point.

	Description	Ratio
$\mathbf{x}=[\sigma_{\text{skin}},\sigma_{\text{skull}},\sigma_{\text{CSF}},\sigma_{\text{WM}},\sigma_{\text{GM}},sf,C_x,C_y,\theta]$	All parameters	0.40
$\dot{\mathbf{x}}=[C_x,C_y,\theta]$	Coil parameters	0.27
$\ddot{\mathbf{x}}=[\sigma_{\text{skin}},\sigma_{\text{skull}},\sigma_{\text{CSF}},\sigma_{\text{WM}},\sigma_{\text{GM}},sf]$	Head parameters	0.29

Table 3.3 The Random Variables, Their Descriptions, and the Ratios of the Standard Deviations of Induced E-fields to the Means of Induced E-fields in Three Cases.

Several observations about the results in Fig. 3.7 are in order:

1. In Figs. 3.7(a), (c), and (e), the maxima of the means of the induced E-fields occur directly under the coil wings. The means of $V_n(\ddot{\mathbf{x}})$ diffuse rapidly [Fig. 3.7(e)]. On the other hand, as the changes in coil parameters directly affect the location and bounds of the stimulated region, the means of $V_n(\mathbf{x})$ and $V_n(\dot{\mathbf{x}})$ [Figs. 3.7(a) and (c)] diffuse slowly compared those of $V_n(\ddot{\mathbf{x}})$ [Fig. 3.7(e)]. In other words, the E-

field plot in Fig. 3.7(e) has a sharper color gradient from red to dark blue compared to the plots in Figs. 3.7 (a) and (c).

In Figs. 3.7(b), (d), and (f), the maxima of the standard deviations of $V_n(\mathbf{x})$, $V_n(\dot{\mathbf{x}})$, and $V_n(\ddot{\mathbf{x}})$ are $29\,\text{V/m}$, $22\,\text{V/m}$, and $22\,\text{V/m}$, respectively. Therefore, the induced E-fields appear sensitive to uncertain quantities in the TMS setup and uncertain quantities related to brain anatomy.

To separately and quantitatively assess the combined effects of all random variables, $\mathbf{x}$, the random variables pertinent to the TMS setup, $\dot{\mathbf{x}}$, and the random variables related to brain anatomy, $\ddot{\mathbf{x}}$, on the magnitude of E-field at the targeted point (indicated in Fig. 3.7), the ratios of the standard deviations of E-fields to their means are computed for these three cases and presented in Table 3.3. Needless to say, the uncertainty in TMS setup and the uncertainty related to brain anatomy have equal impact on the E-fields induced on targeted point. And uncertainty in TMS setup and uncertainty related to brain anatomy collectively change the E-field at the targeted point by 40%.

2) Individual and Combined Effects of Uncertain Quantities to the E-fields: To observe the individual and combined effects of uncertain quantities in TMS setup and uncertain quantities related to brain anatomy on the induced E-fields, four types of data are extracted from the surrogate models. The random variables are restricted to the positions of coil along x'- and y'- directions, i.e. $\dot{\mathbf{x}} = \left[C_x, C_y\right]$, orientation of coil, i.e. $\ddot{\mathbf{x}} = \left[\theta\right]$, the shrink factor, i.e. $\dddot{\mathbf{x}} = \left[sf\right]$, and the tissue conductivities, i.e. $\ddddot{\mathbf{x}} = \left[\sigma_{\text{skin}}, \sigma_{\text{skull}}, \sigma_{\text{CSF}}, \sigma_{\text{WM}}, \sigma_{\text{GM}}\right]$, and the standard deviations of $V_n(\dot{\mathbf{x}})$ [Fig. 3.8(a)], $V_n(\ddot{\mathbf{x}})$ [Fig. 3.8(b)], $V_n(\dddot{\mathbf{x}})$ [Fig. 3.8(c)], and $V_n(\ddddot{\mathbf{x}})$ [Fig. 3.8(d)], are computed, respectively. (Note: the random variables in each case are indicated in Table 3.4).

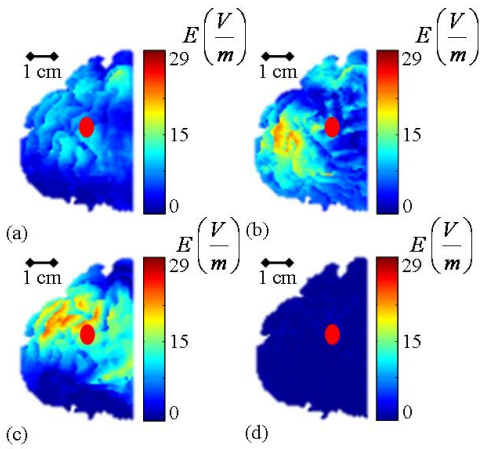

Figure 3.8 The standard deviations of (a) $V_n(\dot{\mathbf{x}})$, (b) $V_n(\ddot{\mathbf{x}})$, (c) $V_n(\dddot{\mathbf{x}})$, and (d) $V_n(\ddddot{\mathbf{x}})$. The red dot indicates the targeted point.

Random Vector	Description	Ratio
$\dot{\mathbf{x}} = [C_x, C_y]$	Coil position	0.13
$\ddot{\mathbf{x}} = [\theta]$	Coil orientation	0.22
$\dddot{\mathbf{x}} = [sf]$	Shrink factor	0.28
$\ddddot{\mathbf{x}} = [\sigma_{\text{skin}}, \sigma_{\text{skull}}, \sigma_{\text{CSF}}, \sigma_{\text{WM}}, \sigma_{\text{GM}}]$	Tissue conductivities	0.01

Table 3.4 The Random Variables, Their Descriptions, and the Ratios of the Standard Deviations of Induced E-fields to the Means of Induced E-fields in Four Cases.

Several observations about the results in Fig. 3.8 are in order:

1. In Fig. 8(a), the standard deviations of E-fields induced on the region right below the center of the coil (i.e. the region around the targeted point) are smaller than the standard deviations of those induced in other regions. This is because the proximity of this region to the coil doesn't change significantly compared to those of nearby regions when the position of the coil is changed (just like in three-sphere head model). In Fig. 3.8(b), the standard deviations of the E-fields induced on the targeted point do not change much because this point is the center of rotation of the coil. On the other hand, as expected, the standard deviations of E-fields induced on regions surrounding this point change significantly. Note that the standard deviations of $V_n(\ddot{\mathbf{x}})$ on the regions surrounding the targeted point [Fig. 3.8(b)] are considerably larger than those of $V_n(\dot{\mathbf{x}})$ on the same regions [Fig. 3.8(a)].

In Fig. 3.8(c), the standard deviations of induced E-fields at the targeted point and its surrounding region are large. This is not surprising as the magnitudes of induced E-fields directly under the coil decrease significantly when the brain is shrunk, i.e. the scalp-to-cortex distance is increased. Like in the three-sphere head model example, it is apparent from Fig. 3.8(d) that uncertainty in the values of tissue conductivities does not significantly affect the induced E-fields

To quantitatively and separately assess the combined effect of the random variables pertinent to positions of coils, $\dot{\mathbf{x}}$, the individual effect of random variable related to orientation of coil, $\ddot{\mathbf{x}}$, the individual effect of random variable related to shrink factor, $\dddot{\mathbf{x}}$, and the combined effect of random variables related to tissue conductivities, $\ddddot{\mathbf{x}}$, on the magnitude of E-field at the targeted point (indicated in Fig3..8), the ratios of the standard deviations of E-fields to the means of E-fields are computed for these four cases and presented in Table IV. Apparently, the uncertainty in coil orientation and the uncertainty in the scalp-to-cortex distance have significant impact on the E-fields induced on targeted point.

Fig. 3.8 showed the statistics of the induced E-fields on the surface of targeted cortical region. To observe the statistics of induced E-fields inside cortical region, a coronal slice passing through the cortical region is selected [Fig. 3.9(a)]. The standard deviations of $V_n(\dot{\mathbf{x}})$ [Fig. 3.9(b)], $V_n(\ddot{\mathbf{x}})$ [Fig. 3.9(c)], and $V_n(\dddot{\mathbf{x}})$ [Fig. 3.9(d)] on the coronal slice are computed. Not surprisingly, the standard deviations of induced E-fields on the surface of cortical region are larger than those inside the cortical region [Figs. 3.9(b)-(d)].

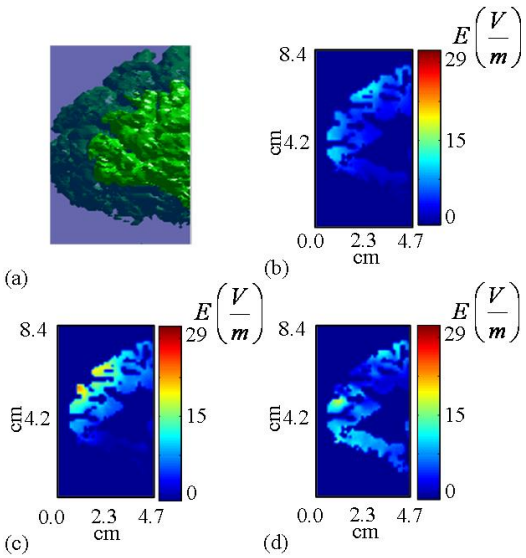

Figure 3.9 (a) The coronal slice (depicted by the purple transparent plane) passing through the cortical region. The standard deviations of (b) $V_n(\dot{\mathbf{x}})$, (c) $V_n(\ddot{\mathbf{x}})$, and (d) $V_n(\dddot{\mathbf{x}})$.

In addition, E-field distributions in the stimulated region, assumed to be the region inside which the magnitudes of E-fields are larger than half of the maximum E-field's magnitude, are observed when each of the random variables C_x, C_y, θ, and sf is set to end points on its corresponding one dimensional random domain while all remaining random variables are set to their mean values [Figs. 3.10(a)-(h)]. Specifically, the E-field distribution in the stimulated region are shown for $C_x = -1.0\,\text{cm}$ [Fig. 3.10(a)], $C_x = 1.0\,\text{cm}$ [Fig. 3.10(b)], $C_y = -1.0\,\text{cm}$ [Fig. 3.10(c)], $C_y = 1.0\,\text{cm}$ [Fig. 3.10(d)], $\theta = 0°$ [Fig. 3.10(e)], $\theta = 90°$ [Fig. 3.10(f)], $sf = 0.0$ [Fig. 3.10(g)], and $sf = 0.1$ [Fig. 3.10(h)].

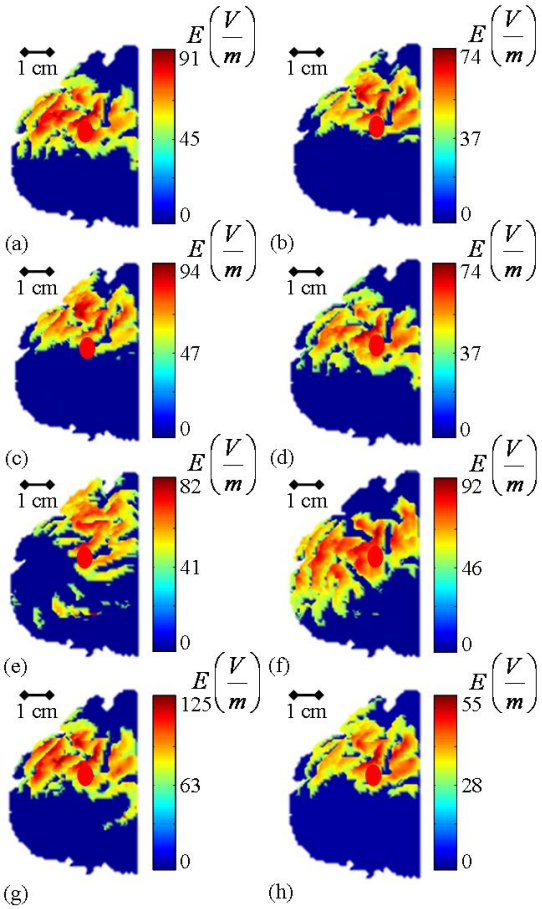

Figure 3.10 The E-field distribution on stimulated region when (a) $C_x = -1.0\,\text{cm}$, (b) $C_x = 1.0\,\text{cm}$, (c) $C_y = -1.0\,\text{cm}$, (d) $C_y = 1.0\,\text{cm}$, (e) $\theta = 0°$, (f) $\theta = 90°$,(g) $sf = 0.0$, and (h) $sf = 0.1$. The red dot indicates the targeted point.

Several observations about the results in Fig. 3.10 are in order:

1. Figs. 3.10(a)-(d) show that a change in coil position results in a shift of the location of the stimulated region.
2. Figs. 3.10(e)-(f) demonstrate that a change in the orientation of the coil results in a rotation of the elliptical stimulated region around the targeted point.
3. Figs. 3.10(g)-(h) show that the maximum E-field magnitude is reduced by a factor of 2.28 when the scalp-to-cortex distance increases, yet the shape and location of the stimulated region remains nearly the same. For that reason, a TMS practitioner should adjust the driver currents of the coil for different brain sizes as pointed out in [59].

4. Although the target point is stimulated in all cases, the stimulated region surrounding the target point changes significantly from case to case [Figs. 10(a)-(h)].

3.4 Conclusion

A computational framework is proposed for uncertainty quantification in TMS. The framework leverages surrogate models of E-fields induced during TMS by iteratively constructing HDMR component functions pertinent to the most significant random variables. Each component function in the HDMR expansions is approximated by the ME-PC method, which effectively tailors the polynomial bases on the support of the component function. The observable values on integration/collocation points identified by the ME-PC method are computed via a quasi-static FD solver. The proposed computational framework is highly efficient and accurate compared to traditional MC methods.

The application of the proposed framework to realistic MRI-derived head models showed that differences in tissue conductivities have a small effect on E-field magnitudes, while the coil position and orientation, and brain size have significant effects on the magnitude of the E-field. Quantitatively, $2\,\text{cm}$ uncertainty in the positions of a coil along the x' and y' directions results in 13% change in the induced E-fields at the targeted point while $90°$ uncertainty in the coil orientation results in 22% change in the induced E-fields at the targeted point. In addition, an uncertainty of 10% of the brain volume results in a 28% change in the induced. E-fields at the targeted point. It has been recognized that an increasing scalp-to-cortex distance reduces the strength of the E-field at the cortex [58, 59], and the results presented here show how this effect extends across the underlying cortex. Assuming that the electric field is oriented along the axon on a bend [1], the results clearly show the significant advantage of stimulation at gyral crests compared to sulci. Thus, when MRI-guided neuronavigation is available [87], practitioners consider the potential advantage derived from stimulating at the crest of a gyrus to obtain maximal stimulation. In standard clinical use without neuronavigation,

referenced either to scalp-based landmarks or motor cortex, variations in induced E-fields due to the gyral anatomy may affect treatment response. This effect may be somewhat mitigated by the spread of the E-field, with a full width half maximum in the range of 2 – 3 cm, but with gyral dimensions in a similar size range, individual differences in gyral anatomy will affect the strength of the neural response.

Significant amounts of deviation were found in the E-field magnitude associated with coil placement, evaluating the effects over 2 cm in each direction of a two-dimensional plane of TMS coil. This may be considered a conservative estimate of the range of difference between scalp location and intended cortical target, and the results demonstrate the wide extent of cortex which might be affected with this level of uncertainty in positioning, covering the better part of the dorsal-lateral prefrontal cortex. Certainly, it is possible to reduce this uncertainty within an individual patient by developing reliable coil placement procedures combined with neuronavigation. However, with current estimates of inaccuracy between the scalp location and desired cortical target, the simulations give a precise quantification of the effect of this inaccuracy on cortical targeting. The quantified inaccuracy may reduce the response rates of the therapy.

The present work has developed an efficient computational framework enabling the accurate estimation of uncertainty in the E-field strength with TMS as commonly practiced for neuropsychiatric treatment. However, the computational framework should have other implications for the field of TMS research and practice. For instance, practitioners often need to adjust coil position to minimize painful scalp stimulation. A precise derivation of the range in which acceptable levels of stimulation occur would permit adjustment of coil position without sacrificing potential therapeutic effects. A relatively simple extension of the technique can incorporate the effect of the level of TMS intensity, as this variable is often altered during treatment without a good understanding of how the underlying E-field is affected. The specific network architecture of the patient probably influences the response rates of TMS therapy. In the future, uncertainty quantification techniques could be applied to analyze how uncertainty in the topology of a neuronal network results in uncertainty in the outcome of the TMS

procedure. Furthermore, experimental setups can use this framework to incorporate observed error in coil placement into the estimate of E-field strength at the cortex.

CHAPTER 4
Fast Finite-Difference Direct Solver for Real-Time Simulation of Transcranial Magnetic Stimulation

4.1 Introduction

Many TMS applications require precise target identification and coil placement. Modern 'neuro-navigated' stereotactic TMS systems use structural MRI images and cameras to identify the optimum coil position for TMS [16, 17]. The optimum coil position is assumed to be on the scalp directly over the targeted cortical site because commercial TMS coils (i.e. Magstim BC-70) in the absence of the head generate electric fields, i.e. Primary fields that are strongly concentrated near the coil center. Unfortunately, the primary electric fields generated by the coil induce charges on boundaries between tissue layers. These charges generate significant "secondary" electric fields inside the head [88]2, and thus, potentially change the optimum coil placement site [18-20].

Fortunately, if an MRI derived conductivity model of the patient's head and a model for the coil is available, the total electric field generated (i.e. primary plus secondary electric field) can be accurately determined by using the finite difference (FD) [21-23] method. In FD, partial differential equations of electromagnetism are approximated by finite-differences to generate a sparse linear systems of equations in field-related quantities [22]. The solution of these systems of equations via iterative or direct solution techniques currently used require minutes and, thus, are virtually ruled out for real-time applications like stereotactic TMS systems. We have developed a fast-direct solver that can solve the FD system of equations in seconds and can be used for real-time applications.

Iterative solution techniques (e.g. conjugate-gradient or quasi-minimal residual techniques [22]) work by repeatedly refining an initial guess of an unknown vector quantity until convergence occurs. There is little computational overhead associated with these techniques and, thus, they are often used. For TMS specific FD equations these linear systems involve an excess of $N=10^7$ unknowns and using an optimized iterative solver it can take well over 2 minutes to compute the secondary fields. Moreover, the iterative procedure needs to be repeated for each different coil configuration considered.

In contrast, for direct solution methods the system of equations is first factored into a form that can be used to rapidly solve for the secondary fields for each coil configuration [89]. Unfortunately, the memory requirements for storing the factorized system of equations usually scales nonlinearly in the number of unknowns, and thus, direct solvers are not used to solve TMS specific FD equations [90].

In this chapter, we propose a fast-direct solver for TMS specific FD equations that exploits the hierarchal low-rank nature of judiciously chosen blocks of the inverse of the FD system matrix and scale (quasi-) linearly in both memory and time. The solver evaluates the secondary field for a given primary field roughly two orders of magnitude faster than preconditioned iterative solvers. Interestingly, the solver permits a rapid update of the inverse of the system matrix if the head model changes by a small number of voxels; this feature extends the use of the solver beyond real-time positioning and closed-loop optimization to studies that aim to investigate effects of brain lesions on TMS fields like [91]. The solver draws on the multifrontal approach of Duff and Reid [92] and on compression by hierarchical matrices [93]. Furthermore, it is conceptually similar to those in [94-97] but has been designed to emphasize versatility of the domain division technique (which serves the factorization, pre- and post-processing steps) and ease of implementation (without affecting asymptotic complexity).

The rest of this chapter is organized as follows. Section 4.2 describes a simple FD scheme for analyzing TMS phenomena and the proposed FD matrix factorization and solution processes. Section 4.3 describes numerical results that benchmark the proposed fast direct solver versus other solvers and illustrate how it can be used for coil placement. Section 4.4 summarizes our achievements and describes avenues for future research.

4.2 Formulation

This section details the proposed fast-direct solver for TMS. First, we outline a FD approach, which yields a linear system of equations:

$$\mathbf{Mx} = \mathbf{b}\,, \tag{4.1}$$

where the unknown vector $\mathbf{x}$ is the scalar potential (a quantity from, which the secondary field is easily determined) at selected points and $\mathbf{b}$ is constructed from the primary field. Then, we will describe the multifrontal [92] and $\mathcal{H}$ -matrix compression [93] approach used for computing and compressing the inverse of $\mathbf{M}$ (i.e. the LU-factorization of $\mathbf{M}^{-1}$) in $O\left(N \cdot \log^2 N\right)$ time, and using $O\left(N \cdot \log N\right)$ memory, where N is the number of unknown variables.

In the multifrontal method inverses of small dense matrices and partial updates are used to construct an LU-factorization of $\mathbf{M}^{-1}$. First, we will describe a process we used to partition the domain into several sub-domains called 'Domain Decomposition'. Then, we will explain how we determine the LU-factorization of $\mathbf{M}^{-1}$ by using the inverses of the small sub-matrices corresponding to the interactions between elements on the same sub-domain and partial updates. Finally, we explain how we lower the time and memory requirements of the multi-frontal approach by using an $\mathcal{H}$ -matrix [93] format (a data sparse representation) to store the matrices. The asymptotic complexity estimates and technical details of the implementation are discussed at the very end of this section.

4.2.1 Finite Difference (FD) Scheme

This solver computes the total electric field $\mathbf{E}(\mathbf{r},t)$ generated at positions $\mathbf{r}$ inside the head when the TMS coil is driven by a current $\mathbf{I}(\mathbf{r};t) = p(t)\mathbf{I}(\mathbf{r})$, where $p(t)$ is a unit pulse. In general, $\mathbf{E}(\mathbf{r};t)$ is composed of a vector $\mathbf{A}(\mathbf{r};t)$ and a scalar potential $\phi(\mathbf{r};t)$ contribution as:

$$\mathbf{E}(\mathbf{r};t) = -\frac{d}{dt}\mathbf{A}(\mathbf{r};t) - \nabla\phi(\mathbf{r};t)\,. \tag{4.2}$$

For the range of frequencies of typical TMS pulses (1-10 kHz) and the range of conductivities of the head (0.01-1.6 S/m) the following quasi-stationary assumptions are valid [98]: (i) the coils are solely responsible for the vector potential contribution of the electric field, (ii) delay effects are negligible (iii) displacement currents are negligible . Correspondingly, the primary electric field is

$$\begin{aligned}\mathbf{E_p}(\mathbf{r},t) &= -\frac{d}{dt}p(t)\mathbf{A}(\mathbf{r}) \\ &= -\frac{d}{dt}p(t)\mu_0 \oint_{coil} \frac{\mathbf{I}(\mathbf{r}')}{4\pi|\mathbf{r}-\mathbf{r}'|}d\mathbf{r}'\end{aligned}, \tag{4.3}$$

where $\mu_0 = 4\pi \times 10^{-7} H/m$ is permeability of free space. The secondary electric field is $\mathbf{E}_s(\mathbf{r},t) = -\nabla\varphi(\mathbf{r};t)$. And gauss's law is:

$$\nabla \bullet \sigma(\mathbf{r})\mathbf{E}(\mathbf{r};t) = 0 \ , \tag{4.4}$$

.

or equivalently,

$$\begin{aligned}&\nabla \bullet \sigma(\mathbf{r})\nabla\varphi(\mathbf{r};t) \\ &= -\nabla \bullet \sigma(\mathbf{r})\frac{d}{dt}\mathbf{A}(\mathbf{r};t) = \frac{d}{dt}p(t)\nabla \bullet \sigma(\mathbf{r})\nabla\varphi(\mathbf{r})\end{aligned}, \tag{4.5}$$

where. $\varphi(\mathbf{r};t) = (dp(t)/dt)\varphi(\mathbf{r})$. Thus, $\mathbf{E_s}(\mathbf{r},t)$ can be easily determined by solving

$$\nabla \bullet \sigma(\mathbf{r})\nabla\varphi(\mathbf{r}) = -\nabla \bullet \sigma(\mathbf{r})\mathbf{A}(\mathbf{r}) . \tag{4.6}$$

Here the scalar potential $\varphi(\mathbf{r})$ is determined using a standard 2nd order FD method for an inhomogeneous Poisson equation [99]. Briefly, a hexahedral region containing the brain is partitioned into a regular Cartesian mesh Ω consisting of $(N_x^0 - 1)\times(N_y^0 - 1)\times(N_z^0 - 1)$ homogenous conductive (i.e. constant $\sigma(\mathbf{r})$) $\Delta_x \times \Delta_y \times \Delta_z$ voxels, where voxel (η,β,ξ) is assigned a conductivity $\sigma_{\eta,\beta,\xi}$ equal to that at its center. The unknown vector $\mathbf{x}$ is a collection of scalar potential $\varphi(\mathbf{r})$ values at each internal node of the Cartesian mesh. Each row of the system matrix $\mathbf{M}$ is a discrete approximation to:

$$\oiint_{\partial V} \sigma(\mathbf{r}) \nabla \varphi(\mathbf{r}) \bullet d\mathbf{s} = -\oiint_{\partial V} \sigma(\mathbf{r}) \mathbf{A}(\mathbf{r}) \bullet d\mathbf{s} \ , \tag{4.7}$$

where V a hexahedral region having dimensions $\Delta_x \times \Delta_y \times \Delta_z$ and centered about a node of the Cartesian mesh with ∂V as its boundary and $d\mathbf{s}$ is oriented by outward-pointing normal vectors. Because $\varphi(\mathbf{r})$ is known to decay rapidly with increasing distance from the head, on the boundary nodes of the Cartesian mesh a zero Dirichlet boundary condition is assumed [98].

The matrix is $\mathbf{M}$ ordered according to a global index vector $\mathbf{p} = \left\{ p_1, p_2, \ldots, p_{N_x^0 N_y^0 N_z^0} \right\}$, where the scalar $p_{\eta+(\beta-1)N_x^0+(\xi-1)N_x^0 N_y^0}$ is the index of the column, or row, corresponding to the scalar potential at position on the internal node (η, β, ξ), or the equation arising from applying (4.7) on the hexahedral region centered about the node (η, β, ξ). (Note: For the remaining sub-sections, we will mainly deal with the lattice of nodes of the Cartesian mesh and refer to the different rows and columns of $\mathbf{M}$ by their associated node and not their index (i.e. we will use (η, β, ξ) instead of $p_{\eta+(\beta-1)N_x^0+(\xi-1)N_x^0 N_y^0}$ to refer to column and rows of the matrix).)

4.2.2 Multi Frontal Approach

4.2.2.1 Domain Decomposition

Domain decomposition utilizes a procedure called geometric bisection where a Cartesian lattice is partitioned into two Cartesian sub-lattices along the longest edge and on its center. In other words, if $N_\eta^0 = \max\{N_x^0, N_y^0, N_z^0\}$, then the lattice is separated into two lattices by a plane oriented perpendicular to the η-direction and situated on the center of the domain. The domain decomposition can be applied to a mesh having arbitrary dimensions, however, for clarity we will assume that $N_x^0 \times N_y^0 \times N_z^0 = P2^a \times P2^b \times P2^c$, where $P, a, b, c \in \mathbb{N}$.

Let Ω_1^0 denote the lattice of nodes of the Cartesian mesh. Ω. First, Ω_1^0 is split into Ω_1^1 and Ω_2^1 by geometric bisection. Then, as depicted in Fig. 4.1, the procedure is

repeated hierarchically until each sub-lattice has dimensions $P \times P \times P$. In other words, at each level each sub-lattice Ω_j^k, where k is the level and j the lattice index, is split into Ω_{2j-1}^{k+1} and Ω_{2j}^{k+1} each with dimensions $N^k = N_x^k N_y^k N_z^k = N / 2^k$ nodes by geometric bisection.

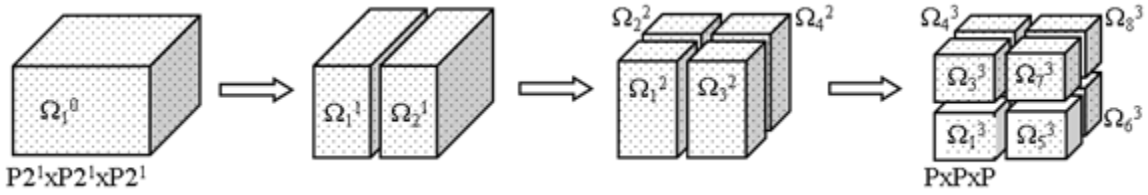

Figure 4.1 Domain decomposition of a $2P \times 2P \times 2P$ domain by geometric bisections.

The domain decomposition is shown schematically as a binary tree $T(\Omega)$ in Fig. 4.2. Each vertex of $T(\Omega)$ correspond to a Ω_j^k sub-lattice and each edge to inheritance relations. The geometric bisection is applied for $K = a \cdot b \cdot c$ levels and $T(\Omega)$ has a depth of $K+1$. The k-th level has $nd(k) = 2^k$ sub-lattices and there are a total of $nd(1) \cdot nd(2) \cdot \ldots \cdot nd(K) = 2^{1+2+\ldots+K}$ sub-lattices.

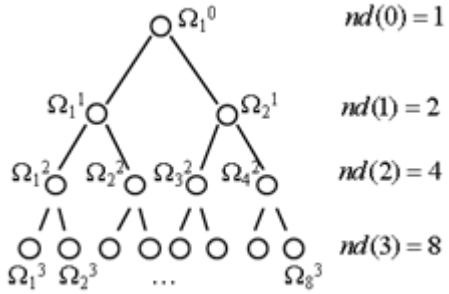

Figure 4.2 Tree representation $T(\Omega)$ of the domain decomposition of a $2P \times 2P \times 2P$. There is a vertex for each subdomain and edges represent inheritance relations. At the k-th level there are $nd(k) = 2^k$ vertices and the depth is $K+1 = 4$.

The LU- factorization utilizes subsets of the sub-lattices called clusters shown in Fig. 4.3. For the K^{th} level each cluster is identical to its sub-lattice. For levels $k < K$,

cluster Γ_j^k consists of the boundaries of the two adjacent Ω_{2j-1}^{k+1} and Ω_{2j}^{k+1} sub-lattices. In other words, j-th cluster Γ_j^k at level k is

$$\Gamma_j^k = \begin{cases} \Omega_j^K & \text{for } k = K \\ \text{bnd}(\Omega_{2j-1}^{k+1}) \cup \text{bnd}(\Omega_{2j}^{k+1}) & \text{for } k < K \end{cases}, \tag{4.8}$$

where $bnd(\Omega_j^k)$ is the set of boundary nodes of Ω_j^k. We further partition each cluster into two sets one containing 'cluster boundary' nodes, i.e. $\Gamma_j^k|_b = bnd(\Omega_j^k)$, and 'cluster internal' nodes $\Gamma_j^K|_i = \Gamma_j^K - \Gamma_j^K|_b$.

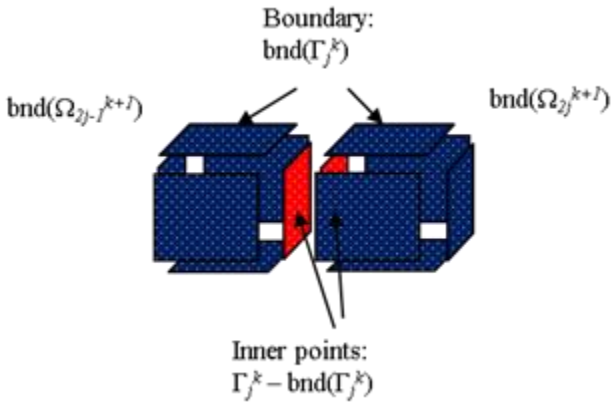

Figure 4.3 Depiction of a generic cluster Γ_j^K. The inner and boundary nodes of a cluster lie on the red and blue regions, respectively.

4.2.2.2 LU-Factorization

The strategy of the LU-factorization is to rearrange the matrix $\mathbf{M}$ into a product of block-diagonal, lower-triangular, and upper-triangular matrices whose inverses can be computed using small matrices, which are determined using algorithm 4.1. The product of $\mathbf{M}^{-1}$ with a vector by using the small matrices is outlined in algorithm 4.2. First we describe how the small matrices whose inverses we need to compute are determined. Then, how the individual small matrix blocks can be assembled to generate a factorized version of $\mathbf{M}^{-1}$.

1: input $\mathbf{M}$

2: for $j = 1, 2, \ldots, nd(K)$

3: $\mathbf{A}^K_{j\,\mathbf{ib}} \leftarrow \mathbf{M}^K_{j\,\mathbf{ib}}$, $\mathbf{A}^K_{j\,\mathbf{bi}} \leftarrow \mathbf{M}^K_{j\,\mathbf{bi}}$, $(\mathbf{A}^K_{j\,\mathbf{ii}})^{-1} \leftarrow (\mathbf{M}^K_{j\,\mathbf{ii}})^{-1}$

4: $\mathbf{S}^K_j \leftarrow \mathbf{A}^K_{j\,\mathbf{bb}} - \mathbf{A}^K_{j\,\mathbf{bi}} (\mathbf{A}^K_j)^{\mathbf{-1}}_{\mathbf{ii}} \mathbf{A}^K_{j\,\mathbf{ib}}$

5: end

6: for $k = K-1, K-2, \ldots, 1$

7: for $j = 1, 2, \ldots, nd(k)$

8: $\mathbf{A}^k_j \leftarrow \begin{cases} \begin{pmatrix} \mathbf{S}^{k+1}_{2j-1} & \mathbf{M}(\Gamma^{k+1}_{2j-1}|_b \times \Gamma^{k+1}_{2j}|_b) \\ \mathbf{M}(\Gamma^{k+1}_{2j}|_b \times \Gamma^{k+1}_{2j-1}|_b) & \mathbf{S}^{k+1}_{2j} \end{pmatrix} & k < K \\ \mathbf{M}^K_j & k = K \end{cases}$

9: compute $(\mathbf{A}^k_{j\mathbf{ii}})^{-1}$

10: $\mathbf{S}^k_j \leftarrow \mathbf{A}^k_{j\mathbf{bb}} - \mathbf{A}^k_{j\mathbf{bi}} (\mathbf{A}^k_j)^{\mathbf{-1}}_{\mathbf{ii}} \mathbf{A}^k_{j\mathbf{ib}}$

11: end

12: end

13: $(\mathbf{S}^1_0)^{-1} \leftarrow (\mathbf{A}^1_{0\mathbf{bb}} - \mathbf{A}^1_{0\mathbf{bi}} (\mathbf{A}^1_0)^{\mathbf{-1}}_{\mathbf{ii}} \mathbf{A}^1_{0\mathbf{ib}})^{-1}$

14: return $(\mathbf{A}^k_{j\mathbf{ii}})^{-1}$, $\mathbf{A}^k_{j\mathbf{ib}}$, $\mathbf{A}^k_{j\mathbf{bi}}$ and $(\mathbf{S}^1_0)^{-1}$

Algorithm 4.1: Computation of the Schur complements

1: input $\mathbf{b}$, $(\mathbf{A}^k_{j\mathbf{ii}})^{-1}$, $\mathbf{A}^k_{j\mathbf{ib}}$, $\mathbf{A}^k_{j\mathbf{bi}}$ and $(\mathbf{S}^1_0)^{-1}$

2: $\mathbf{x} = \mathbf{b}$

3: for $k = K-1, K-2, \ldots, 1$

4: for $j = 1, 2, \ldots, nd(k)$

5: $\mathbf{x}^k_{j\mathbf{b}} \leftarrow \mathbf{x}^k_{j\mathbf{b}} - \mathbf{A}^k_{j\mathbf{bi}}(\mathbf{A}^k_{j\mathbf{ii}})^{-1}\mathbf{x}^k_{j\mathbf{i}}$ (forward-substitution)

6: end

7: end

8: $\mathbf{x}^0_{1\mathbf{b}} \leftarrow (\mathbf{S}^0_1)^{-1}\mathbf{x}^0_{1\mathbf{b}}$

9: for $k = 1, 2, \ldots, K$

10: for $j = 1, 2, \ldots, nd(k)$

11: $\mathbf{x}^k_{j\mathbf{i}} \leftarrow (\mathbf{A}^k_{j\mathbf{ii}})^{-1}(\mathbf{x}^k_{j\mathbf{i}} - \mathbf{A}^k_{j\mathbf{ib}}\mathbf{x}^k_{j\mathbf{b}})$ (backward -substitution)

12: return $\mathbf{x}$

Algorithm 4.2: Multiply with $\mathbf{M}^{-1}$

For notational brevity, for any generic matrix $\mathbf{C}$ where there is an equation and variable associated with each node of the Cartesian lattice Ω^0_1 (e.g. $\mathbf{M}$), we denote $\mathbf{C}^k_j$ the sub-block of the matrix $\mathbf{C}$ corresponding to the rows and columns associated with the cluster Γ^k_j. Furthermore, $\mathbf{C}^k_j$ can be split into four parts by distinguishing between inner and boundary cluster nodes, that is,

$$\mathbf{C}^k_j \equiv \mathbf{C}\left(\Gamma^k_j \times \Gamma^k_j\right) = \begin{pmatrix} \mathbf{C}^k_{j\mathbf{ii}} & \mathbf{C}^k_{j\mathbf{ib}} \\ \mathbf{C}^k_{j\mathbf{bi}} & \mathbf{C}^k_{j\mathbf{bb}} \end{pmatrix}, \tag{4.9}$$

where $\mathbf{C}^k_{j\mathbf{ii}}$, $\mathbf{C}^k_{j\mathbf{ib}}$, $\mathbf{C}^k_{j\mathbf{bi}}$ and $\mathbf{C}^k_{j\mathbf{bb}}$ denote the sub-blocks $\mathbf{C}(\Gamma^k_j|_i \times \Gamma^k_j|_i)$, $\mathbf{C}(\Gamma^k_j|_i \times \Gamma^k_j|_b)$, $\mathbf{C}(\Gamma^k_j|_b \times \Gamma^k_j|_i)$ and $\mathbf{C}(\Gamma^k_j|_b \times \Gamma^k_j|_b)$, respectively. For example,

$$\mathbf{Mx} = \begin{pmatrix} \odot & \begin{bmatrix} \mathbf{0} & \odot \end{bmatrix} & \odot \\ \begin{bmatrix} \mathbf{0} \\ \odot \end{bmatrix} & \begin{bmatrix} \mathbf{M}^K_{j\,\mathbf{ii}} & \mathbf{M}^K_{j\,\mathbf{ib}} \\ \mathbf{M}^K_{j\,\mathbf{bi}} & \mathbf{M}^K_{j\,\mathbf{bb}} \end{bmatrix} & \begin{bmatrix} \mathbf{0} \\ \odot \end{bmatrix} \\ \odot & \begin{bmatrix} \mathbf{0} & \odot \end{bmatrix} & \odot \end{pmatrix} \begin{pmatrix} \vdots \\ \begin{pmatrix} \mathbf{x}^K_{j\,\mathbf{i}} \\ \mathbf{x}^K_{j\,\mathbf{b}} \end{pmatrix} \\ \vdots \end{pmatrix}, \quad (4.10)$$
$$= \begin{pmatrix} \vdots \\ \begin{pmatrix} \mathbf{b}^K_{j\,\mathbf{i}} \\ \mathbf{b}^K_{j\,\mathbf{b}} \end{pmatrix} \\ \vdots \end{pmatrix}$$

where $\odot$ denote the non-zero blocks of matrix $\mathbf{M}$.

In Fig.4.4 all the clusters Γ^k_j are shown for a domain, the regions of each cluster with internal lattice points are colored red and the regions for boundary points blue. For all of the clusters, the inner points (i.e. red regions) are completely enclosed by the boundary points. Since, the non-zero entries of the matrix $\mathbf{M}$ correspond to "interactions" between directly neighboring points, the rows and columns of $\mathbf{M}$ corresponding to $\Gamma^k_j|_i$ have non zero entries only on $\mathbf{M}^k_{j\mathbf{ii}}$, $\mathbf{M}^k_{j\mathbf{ib}}, \mathbf{M}^k_{j\mathbf{bi}}$. Consequently, shur-complements can be used to lower the computational cost of computing $\mathbf{M}^{-1}$ to that of computing $(\mathbf{A}^k_j)_{\mathbf{ii}}^{-1}$, $\mathbf{A}^k_{j\mathbf{bi}}$ and $\mathbf{A}^k_{j\mathbf{ib}}$ at each level and a matrix $(\mathbf{S}^0_1)^{-1}$, where

$$\mathbf{A}^k_j = \begin{cases} \begin{pmatrix} \mathbf{S}^{k+1}_{2j-1} & \mathbf{M}(\Gamma^{k+1}_{2j-1}|_b \times \Gamma^{k+1}_{2j}|_b) \\ \mathbf{M}(\Gamma^{k+1}_{2j}|_b \times \Gamma^{k+1}_{2j-1}|_b) & \mathbf{S}^{k+1}_{2j} \end{pmatrix} & k < K \\ \mathbf{M}^K_j & k = K \end{cases}, \quad (4.11)$$

$$\mathbf{S}^k_j = \mathbf{A}^k_{j\mathbf{bb}} - \mathbf{A}^k_{j\mathbf{bi}} (\mathbf{A}^k_j)_{\mathbf{ii}}^{-1} \mathbf{A}^k_{j\mathbf{ib}}, \quad (4.12)$$

and $k = 1,2,...,K$ and $j = 1,2,...,nd(k)$. The $\mathbf{A}^k_j$s and $\mathbf{S}^k_j$s are defined recursively starting from $\mathbf{A}^K_j = \mathbf{M}^K_j$ and $\mathbf{S}^K_j = \mathbf{M}^K_{j\,\mathbf{bb}} - \mathbf{M}^K_{j\,\mathbf{bi}} (\mathbf{M}^K_j)_{\mathbf{ii}}^{-1} \mathbf{M}^K_{j\,\mathbf{ib}}$ each time decreasing the level by 1 and ending at the $k = 1$ level. Furthermore, at each level, $\mathbf{A}^k_j$ must be computed before $\mathbf{S}^k_j$. The procedure for computing the matrices $(\mathbf{A}^k_j)_{\mathbf{ii}}^{-1}$, $\mathbf{A}^k_{j\mathbf{bi}}$, $\mathbf{A}^k_{j\mathbf{ib}}$ and $(\mathbf{S}^0_1)^{-1}$ is outlined in Algorithm 4.1.

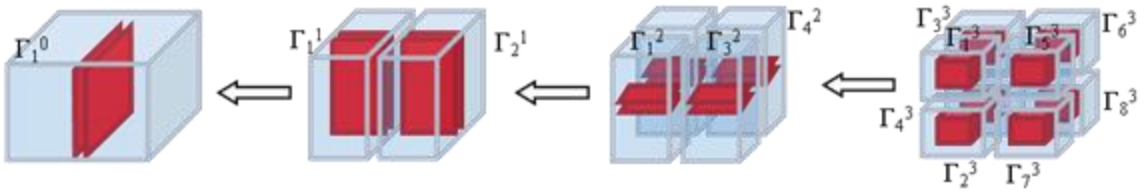

Figure 4.4 Clusters for a $2P\times 2P\times 2P$ domain. The inner and boundary nodes of a cluster lie on the red and blue regions, respectively.

The matrices $(\mathbf{A}_j^k)_{\mathbf{ii}}^{-1}$, $\mathbf{A}_{j\mathbf{bi}}^k$, $\mathbf{A}_{j\mathbf{ib}}^k$ and $(\mathbf{S}_1^0)^{-1}$ are Shur-complements and they make solution of internal points of each cluster independent of the solution of the rest of the domain. Thus, they enable determination of $\mathbf{x}$ applying $(\mathbf{A}_j^k)_{\mathbf{ii}}^{-1}$, $\mathbf{A}_{j\mathbf{bi}}^k$, $\mathbf{A}_{j\mathbf{ib}}^k$ and $(\mathbf{S}_1^0)^{-1}$ to $\mathbf{b}$, as in algorithm 4.2. In algorithm 4.2, the back-substitutions and forward-substitution correspond to the following product

$$\mathbf{M}^{-1}=\left(\mathbf{U}\right)^{-1}\mathbf{P}^{\mathbf{T}}\mathbf{D}^{-1}\mathbf{P}\left(\mathbf{L}\right)^{-1}, \tag{4.13}$$

where,

$$\mathbf{L}_j^k=\begin{pmatrix}\mathbf{I} & \begin{bmatrix}\mathbf{0} & \mathbf{0}\end{bmatrix} & \mathbf{0}\\ \mathbf{0} & \begin{bmatrix}\mathbf{I} & \mathbf{0}\\ \mathbf{A}_{j\mathbf{bi}}^k(\mathbf{A}_{j\mathbf{ii}}^k)^{-1} & \mathbf{I}\end{bmatrix} & \mathbf{0}\\ \mathbf{0} & \begin{bmatrix}\mathbf{0} & \mathbf{0}\end{bmatrix} & \mathbf{I}\end{pmatrix},\qquad \mathbf{U}_j^k=\begin{pmatrix}\mathbf{I} & \begin{bmatrix}\mathbf{0} & \mathbf{0}\end{bmatrix} & \mathbf{0}\\ \mathbf{0} & \begin{bmatrix}\mathbf{I} & (\mathbf{A}_{j\mathbf{ii}}^k)^{-1}\mathbf{A}_{j\mathbf{ib}}^k\\ \mathbf{0} & \mathbf{I}\end{bmatrix} & \mathbf{0}\\ \mathbf{0} & \begin{bmatrix}\mathbf{0} & \mathbf{0}\end{bmatrix} & \mathbf{I}\end{pmatrix}, \tag{4.14}$$

$$\begin{aligned}\mathbf{L}^k&=\mathbf{L}_1^k\cdot\mathbf{L}_2^k\ldots\mathbf{L}_{nd(k)}^k\\ \mathbf{U}^k&=\mathbf{U}_1^k\cdot\mathbf{U}_2^k\ldots\mathbf{U}_{nd(k)}^k\end{aligned}, \tag{4.15}$$

$$\begin{aligned}\mathbf{L}&=\mathbf{L}^1\cdot\mathbf{L}^2\ldots\mathbf{L}^K\\ \mathbf{U}&=\mathbf{U}^1\mathbf{U}^2\ldots\mathbf{U}^K\end{aligned}, \tag{4.16}$$

$$\mathbf{D}=\begin{pmatrix} \mathbf{D^K} & & \mathbf{0} & \\ & \ddots & \mathbf{0} & \mathbf{0} \\ \mathbf{0} & \mathbf{0} & \mathbf{D^1} & \mathbf{0} \\ & \mathbf{0} & \mathbf{0} & \mathbf{S}_1^1 \end{pmatrix}, \tag{4.17}$$

$$\mathbf{D}^k \equiv \begin{pmatrix} \mathbf{A}_{1\,\mathbf{ii}}^k & \mathbf{0} & \mathbf{0} \\ \mathbf{0} & \ddots & \mathbf{0} \\ \mathbf{0} & \mathbf{0} & \mathbf{A}_{nd(k)\mathbf{ii}}^k \end{pmatrix}, \tag{4.18}$$

$k=1,2,...,K$ and $j=1,2,...,nd(k)$, and $\mathbf{P}$ is a permutation matrix that arranges the variables by listing only internal nodes of each cluster starting from the $k=K$ level. The the forward substitution computes the inverse of $\mathbf{L}$ and the back substitution computes the inverse of $\mathbf{U}$. Each step of the back and forward algorithm represent a product with each of the following matrices:

$$\begin{aligned} (\mathbf{L})^{-1} &= \left(\mathbf{L}^1\right)^{-1}\left(\mathbf{L}^2\right)^{-1}....\left(\mathbf{L}^K\right)^{-1}, \\ (\mathbf{U})^{-1} &= \left(\mathbf{U}^K\right)^{-1}\left(\mathbf{U}^{K-1}\right)^{-1}....\left(\mathbf{U}^1\right)^{-1} \end{aligned}, \tag{4.19}$$

where,

$$\begin{aligned} \left(\mathbf{L}^k\right)^{-1} &= \left(\mathbf{L}_1^k\right)^{-1}\cdot\left(\mathbf{L}_2^k\right)^{-1}...\left(\mathbf{L}_{nd(K)}^k\right)^{-1} \\ \left(\mathbf{U}^k\right)^{-1} &= \left(\mathbf{U}_1^k\right)^{-1}\cdot\left(\mathbf{U}_2^k\right)^{-1}...\left(\mathbf{U}_{nd(K)}^k\right)^{-1} \end{aligned}, \tag{4.20}$$

and

$$\begin{aligned} \left(\mathbf{L}_j^k\right)^{-1} &= \begin{pmatrix} \mathbf{I} & \begin{bmatrix} \mathbf{0} & \mathbf{0} \end{bmatrix} & \mathbf{0} \\ \mathbf{0} & \begin{bmatrix} \mathbf{I} & \mathbf{0} \\ -\mathbf{A}_{j\mathbf{bi}}^k(\mathbf{A}_{j\mathbf{ii}}^k)^{-1} & \mathbf{I} \end{bmatrix} & \mathbf{0} \\ \mathbf{0} & \begin{bmatrix} \mathbf{0} & \mathbf{0} \end{bmatrix} & \mathbf{I} \end{pmatrix} \\ \left(\mathbf{U}_j^k\right)^{-1} &= \begin{pmatrix} \mathbf{I} & \mathbf{0} & \mathbf{0} \\ \mathbf{0} & \begin{bmatrix} \mathbf{I} & -(\mathbf{A}_{j\mathbf{ii}}^k)^{-1}\mathbf{A}_{j\mathbf{ib}}^k \\ \mathbf{0} & \mathbf{I} \end{bmatrix} & \mathbf{0} \\ \mathbf{0} & \begin{bmatrix} \mathbf{0} & \mathbf{0} \end{bmatrix} & \mathbf{I} \end{pmatrix} \end{aligned}. \tag{4.21}$$

From (4.21) it is clear that only matrices $\left(\mathbf{S}_0^1\right)^{-1}$, $\left(\mathbf{A}_{j\mathbf{ii}}^k\right)^{-1}$, $\mathbf{A}_{j\mathbf{bi}}^k$, and $\mathbf{A}_{j\mathbf{ib}}^k$ are necessary for computing $\mathbf{M}^{-1}$. These matrices can be easily determined using dense matrix algebra. However, in the next section we will introduce $\mathcal{H}$-matrix algebra, which, can be used to rapidly compute and compress them.

4.2.3 Compression by $\mathcal{H}$-matrices

In the previous section an algorithm for computing and storing the LU-factorization of $\mathbf{M}$ in an efficient way was described. However, computing $\left(\mathbf{S}_1^1\right)^{-1}$, $\left(\mathbf{A}_{j\mathbf{ii}}^k\right)^{-1}$, $\mathbf{A}_{j\mathbf{bi}}^k$, and $\mathbf{A}_{j\mathbf{ib}}^k$ using dense matrix algebra requires excessive computational resources. Fortunately, each of these matrices can be compressed using the $\mathcal{H}$-matrix format introduced by Hackbusch [93]. This approach has already been effectively used in other direct solvers and block-diagonal preconditioners [97, 100-105] as it can lower the orders of the matrix-matrix and matrix-vector multiplication complexities and the storage requirements of a n-by-n matrix from $O(n^3)$, $O(n^2)$ and $O(n^2)$ down to $O(n\cdot\log^2 n)$, $O(n\cdot\log n)$ and $O(n\cdot\log n)$, respectively [106]. In general, the formal structure of the $\mathcal{H}$-matrix approximation to a given matrix depends highly on the type of matrix being compressed. Here, only the construction of $\mathcal{H}$-matrices out of the dense matrices arising from the LU factorization of $\mathbf{M}$ are explained. For a more general theory of $\mathcal{H}$-matrices, as well as, more detailed explanations of the method consult [93, 106, 107].

An $\mathcal{H}$-matrix approximation to a given (full) matrix is obtained by hierarchically partitioning the matrix and at each level replacing certain blocks of the (full) matrix with a compressed format called the 'Rk-format'. In the 'Rk-format' a $m\times n$ matrix $\mathbf{D}$ with maximum singular value $\sigma_{\max}$ and r singular values greater than $\varepsilon\sigma_{\max}$, is stored to a precision of ε as [93]

$$\mathbf{D}_{m\times n}\approx\mathbf{u}_{m\times r}\cdot\mathbf{v}_{r\times n}, \tag{4.22}$$

where $\mathbf{u}$ and $\mathbf{v}$ are $m\times r$ and $r\times n$ matrices, respectively. If the value $r<mn/(m+n)$, then storing matrices $\mathbf{u}$ and $\mathbf{v}$ instead of storing the block $\mathbf{D}$ in the full matrix format

(column by column) reduces the number of elements to be stored from $m \cdot n$ down to $(m+n) \cdot r$. To assess the level of compression that is achieved the compression ratio

$$cr = \frac{n_{cmpr}}{n_{full}} \ , \tag{4.23}$$

where n_{cmpr} and n_{full} is the number entries in the compressed format and in the full format, respectively, is used. Compression is only achieved if $cr < 1$, and we would like $cr << 1$, furthermore, storing $\mathbf{D}$ in the Rk-format results in a compression ratio of $cr = (m+n)r / mn$. Thus, storing $\mathbf{D}$ in the Rk-format is only guaranteed to result in compression when $r < \max(m,n)/2$. For the matrices we consider here, the value of the rank is not known a priori, however, an upper bound k for it is known. Thus, the actual rank is determined during run-time by using a rank revealing factorization (e.g. Singular Value Decomposition).

Let $\mathbf{C}$ be one of $\left(\mathbf{S}_1^0\right)^{-1}$, $\left(\mathbf{A}_{j\mathbf{ii}}^k\right)^{-1}$, $\mathbf{A}_{j\mathbf{bi}}^k$, or $\mathbf{A}_{j\mathbf{ib}}^k$ and have associated cluster Γ_j^k. For FD matrices arising from Poisson kernels (i.e. $\mathbf{M}$) and their inverses, the rank of sub-blocks of the matrices representing interactions between two clusters of nodes decreases with relative distance between the clusters [106, 107]. Consequently, the 'admissible' blocks of $\mathbf{C}$ (i.e. sub-blocks of $\mathbf{C}$ that can be compressed), correspond to interactions between two distant sub-clusters of Γ_j^k. To extract the admissible blocks of $\mathbf{C}$ we specify a condition for admissibility as follows: Let $\mathbf{t}_i$ and $\mathbf{t}_j$ be detached sub-clusters Γ_j^k (i.e. $\mathbf{t}_i, \mathbf{t}_j \subset \Gamma_j^k, \mathbf{t}_i \cap \mathbf{t}_j = 0$), let $diam(\mathbf{t}_i)$ denote the largest physical distance between any two distinct cluster points in $\mathbf{t}_i$ and $separ\left(\mathbf{t}_i, \mathbf{t}_j\right)$ the minimum physical distance between one point in $\mathbf{t}_i$ and another in $\mathbf{t}_j$, then, we say that the corresponding matrix block is admissible if

$$min\left\{diam\left(\mathbf{t_1}\right),\ diam(\mathbf{t_2})\right\} \le 2\eta \cdot separ\left(\mathbf{t_1}, \mathbf{t_2}\right), \tag{4.24}$$

where the value of η is a small number close to one that defines the admissibility, e.g. $\eta = \sqrt{3}/2$ [106]. The admissibility condition of (4.24) ensures that the two clusters are separated by at least a fraction η of the diameter of the smaller of the two clusters.

The $\mathcal{H}$-matrix structure of $\mathbf{C}$ is created by recursively bisecting the cluster using a block cluster tree $T(\Omega\times\Omega)$ in a similar way as was done with the lattice tree $T(\Omega)$. At each level admissible blocks are stored in the Rk-format and inadmissible blocks are further bisected. We repeat the procedure recursively until each block is not admissible, smaller than 196×196 or too small to achieve a $cr<0.95$; we store the remaining sub-blocks as full matrices. Each matrix is compressed to a precision $\varepsilon=\delta\sigma_{\mathbf{M}}/\sigma_{\max}$, where $\sigma_{\mathbf{M}}$ and $\sigma_{\max}$ are the maximum singular values of the matrix $\mathbf{M}$ and the matrix being compressed, respectively, and δ is an input threshold value parameter to the algorithm.

4.2.4 Assymptotic Complexity estimates $\mathcal{H}$-matrices

For the $\mathcal{H}$-matrices we consider, the computational resources (i.e. computational complexity) required to perform most linear algebra operations (e.g. matrix-matrix addition or multiplication) scale almost linearly with size. More precisely, if $P(n)$ is a function that for a $n\times n$ $\mathcal{H}$-matrix counts memory requirements to store it or the number of operations required to compute a matrix-vector multiplication or a matrix inversion, then $P(n)$ is $O\left(n\cdot\log_2 n\right)$ or $O\left(n\cdot\log_2^2 n\right)$ or $O\left(n\cdot\log_2^2 n\right)$, respectively [106], where $O(\cdot)$ denotes asymptotic complexity.

The overall asymptotic complexity of the factorization and solution steps (Algorithms 4.1 and 4.2) can be obtained by counting operations at each level of the process. At each level the number of nodes in each Ω_j^k lattice is roughly $N/2^k$ nodes. Since the cluster points Γ_j^k lie on facets of Ω_{2j-1}^{k+1} and Ω_{2j}^{k+1}, it has roughly $n\approx 6N^{2/3}/2^{2k/3}$ nodes. Correspondingly, the number operations that are performed on each of the $\mathcal{H}$-matrices associated with each cluster is $O\left(N^{2/3}/2^{2k/3}\cdot\log_2^{\alpha}N^{2/3}\right)$, where α is 1 or 2. Furthermore, there are $nd(k)=2^k$ clusters at each level. Thus, the number of operations required to perform algorithms 4.1 and 4.2 is:

$$O\left(\left\{\begin{matrix}1+2^1(\frac{1}{2^{2/3}})+\ldots\\ +2^K(\frac{1}{2^{2K/3}})\end{matrix}\right\}N^{2/3}\log_2^{\alpha}N^{2/3}\right), \qquad (4.25)$$
$$=O(N\log_2^{\alpha}N^{2/3})$$

where α= 1 for the solution time and α= 2 for the factorization time. (Note: we used $K=\log_2(N/P^3)$ to simplify (4.25).)

Similarly the total memory required scales as the total storage to store individual $\mathcal{H}$-matrix times the number of $\mathcal{H}$-matrices. Thus, the total memory required is $O(N\cdot\log_2 N)$.

4.2.5 Implementation Details

The solver has two main independent parts: a library of subroutines for hierarchical matrices and our implementation of the multifrontal method. The hierarchical matrix library contains subroutines for linear algebra operations on $\mathcal{H}$-matrices (and other data-sparse structures) [93]. Most of the subroutines use BLAS and LAPACK for basic linear algebra operations. Our multifrontal method library is capable of decomposing a hexagonal computational domain of an arbitrary size. Depending on the problem size, the bisecting process is stopped for $P=4$ or $P=8$. The factorization (Algorithm 1) computes and stores matrices $\mathbf{A_{ii}}$ (in the compressed format), $\mathbf{A_{ib}}$ and $\mathbf{A_{bi}}$ (in the MKL's coordinate format). To reduce the computational overhead and to increase the execution speed, matrix blocks smaller than 196×196 and blocks with compression ratios more than 0.95 are treated as full matrices regardless of whether they are admissible or not; required operations on these blocks are performed by BLAS/LAPACK subroutines. Other than $\mathbf{S}_1^1$ the intermediate Schur complements are not necessary for the final solution step and they are not stored.

4.3 Application of the Fast Direct Solver to TMS

In this section, we demonstrate the robustness of the proposed solver in terms of memory and speed and show that it compares favorably to a commercial multi-frontal direct solver (PARDISO). We also demonstrate an application for real-time coil positioning during TMS. All runs are run on our cluster consisting of 66 nodes each with a quad-core AMD Opteron 2220 SE processor and 16 GB of physical RAM per computer node.

4.3.1 Benchmark Tests

Here we investigate how the fast direct solver parameters (e.g. P) affect solution accuracy, time, and memory. Furthermore, we also compare the proposed solver to PARDISO, a commercial sparse direct solver and part of Intel's MKL library [108]. To do this we consider the electric field generated inside homogenous (i.e. when $\sigma(\mathbf{r}) = 1\text{S/m}$ hexahedral domains $\forall\ \mathbf{r} \in \Omega$) of varying sizes. We choose forcing vectors $\mathbf{b}$ generated using a uniform random number generator. We determine the solution $\mathbf{x}$ using the fast direct solver and the 'exact' reference solution $\mathbf{x}_{\mathbf{ref}}$ by using PARDISO with double precision. All of the runs in this section are done on a single cluster node.

First, we varied the threshold value δ and analyzed a domain with 64^3 unknowns. Table 4.1 lists the memory used and CPU runtime by the fast direct solver when run with different thresholds. Since computational resources are expected to have a logarithmic dependence with respect to precision ε, which is directly related to δ, we used the following regression function $y(\delta) = \mathrm{y}_0 + \mathrm{c} \cdot \log^2(\delta)$, where c is a positive factor, to interpolate each of the computational resources measured as a function of δ. The values of y_0 for the memory, factorization and solution runtimes are 2786 MB, 1239 seconds and 1.14 seconds, respectively. The values of y_0 are important because they are lower bounds for the resources required to obtain a factorization with a threshold less than 1. By decreasing δ from 10^{-3} to 10^{-6} the solution runtime is increased by 7%, and the factorization runtime by 25%. Thus, by increasing the accuracy of the compression from

10^{-3} to 10^{-6} not many more computational resources are necessary. Consequently, we use $\delta = 10^{-6}$ for subsequent numerical experiments.

Threshold	Residuum	Error	Storage (MB)	cr	Factorization (sec)	Solution (sec)
1E-2	1.08E-03	1.18E-01	2832	0.46	1289	1.16
1E-3	1.36E-04	9.97E-03	2891	0.47	1354	1.19
1E-4	1.05E-05	4.64E-04	2964	0.48	1438	1.22
1E-5	1.03E-06	1.68E-05	3038	0.49	1562	1.36
1E-6	1.13E-07	9.98E-07	3121	0.50	1703	1.27

Table 4.1 Performance of the fast direct solver in dependence on the level of accuracy for a domain of size 64x64x64.

Secondly, to determine the asymptotic memory and speed costs of the fast direct solver, we varied the number of unknowns N by factorizing matrices arising from different domain sizes while keeping all other solver parameters constant. To determine minimal, or optimized, storage, we replace the strong admissibility criterion with a compressibility criterion, that is, we compute each sub-matrix in full format and Rk-format and choose the format that uses the least memory (i.e. we store as full if $r > \max(m,n)/2$ otherwise we store it in the Rk-format). Fig. 4.5 shows the total memory required to store the factorized matrix by the fast direct solver for domains of varying sizes along with the 'optimized storage'. As expected, the memory of the factorized matrix depends almost linearly on N. The direct solver only requires 1.2 – 1.5 times the minimal storage. Thus, the admissibility criterion of the fast direct solver is able to achieve an almost ideal compression.

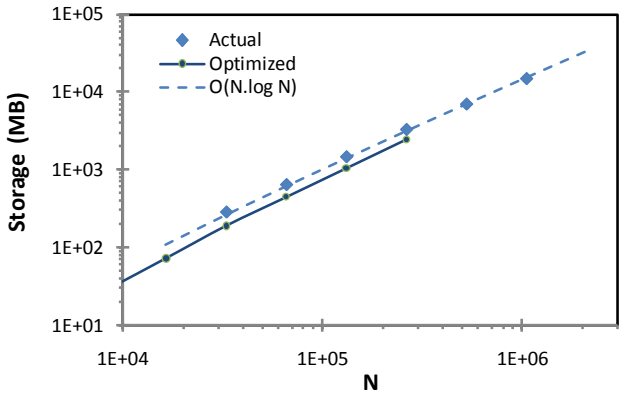

Figure 4.5 Storage memory for the factorized matrix

Fig. 4.6 shows the total factorization and solution run times for domains of varying sizes along with curves for the predicted solution and factorization run times. To generate the predicted run time curves, we formed two curves by fitting the data to the asymptotic run time of the different steps, that is, $N \cdot \log^2 N + c$ for factorization and $N \cdot \log N + c$ for solution (c is just some arbitrary constant). There is mostly good agreement with the expected asymptotic behavior. Note: the last point on the solution time is much greater than the other solution. However, this is not because the algorithm does not scale it is because there is not enough physical memory and some swapping occurs this, in turn, slows down computations.

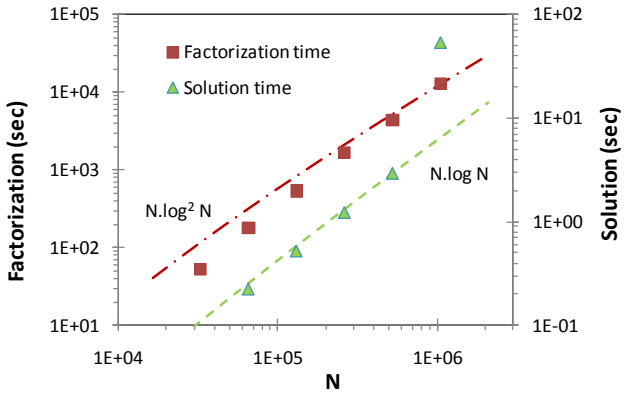

Figure 4.6 Performance of the fast direct solver on a single CPU. Factorization time (squares) and solution time (triangles). Lines show the expected asymptotic behavior.

Lastly, we compare the fast direct solver with PARDISO, a commercial multi-frontal direct solver. Fig. 4.7 shows the ratio of memory used to store the factorized inverse matrix by the fast-direct solver versus PARDISO for varying domain sizes. A ratio of near 1 means that most of the sub-matrices are being stored in the full matrix format by the fast direct solver and smaller ratios mean that more of the sub-matrices are being stored in the Rk-format. As expected, the compression ratio decreases with increasing domain sizes. Fig. 4.8 shows the rank distribution of $\left(\mathbf{A}^1_{1ii}\right)^{-1}_{(7688\times 7688)}$ matrix for a domain of size $128\times 64\times 64$. This sub-matrix represents the diagonal sub-block of a fairly large cluster and the compression is effective, that is, many of the square off-

diagonal blocks have a vector length between 200 to 1000 unknowns and the ranks vary from 5 to 24.

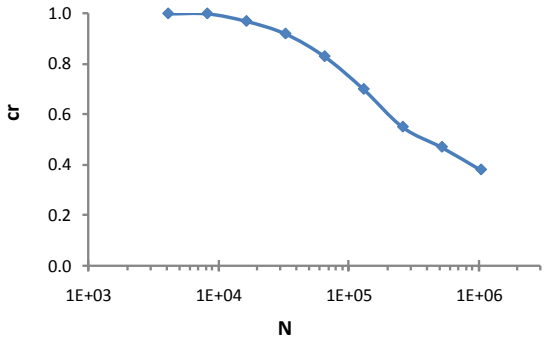

Figure 4.7 Compression ratio of the factorized LU decomposition as a function of the domain size.

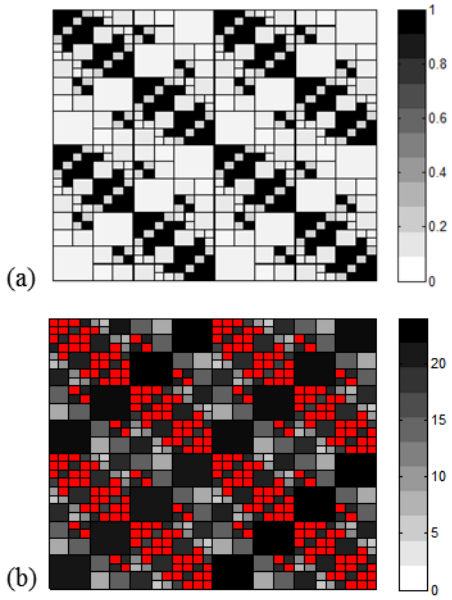

Figure 4.8 (a) Compression ratio and (b) rank distribution of matrix A_{ii}^{-1} of the node T_{10} for the air-filled domain of size 128x64x64, P=4 and threshold 10^{-6}. The largest rank is 24. The red blocks in the rank distribution represent matrices in the full format

Table 4.2 lists the total factorization and solution run times and total memory required to run fast direct solver and PARDISO for domains of varying sizes. For small domains (i.e. $N \leq 32^3$ unknowns) PARDISO performs better than the fast direct solver.

However, for large domains (i.e. $N > 32^3$ unknowns) the fast direct solver has a faster solution time and for $N \geq 72^3$ it uses less memory. The smallest domain size where the fast direct solver starts to require less total factorization run time was not observed because we could not factorize a big enough matrix using PARDISO using a single node.

size	N	Storage (MB)		Factorization (sec)		Solution (sec)	
		Pardiso	FDS	Pardiso	FDS	Pardiso	FDS
32^3	32768	157	283	8	53	0.1	0.1
64^3	262144	2900	3313	549	1683	1.3	1.2
72^3	373248	4700	4693	1106	3142	2.2	1.9
81^3	531441	8152	6929	2330	5669	4.1	3.2
90^3	729000	12500	9550	4630	8658	7.2	4.7

Table 4.2 Performance comparison between the sparse direct solver Pardiso and the fast direct solver (threshold 1E-6).

Fig. 4.9 shows the residual error $r = \|\mathbf{b} - \mathbf{M}\mathbf{x}\|_2 / \|\mathbf{b}\|_2$ and relative solution error $e = \|\mathbf{x} - \mathbf{x}_{\mathbf{ref}}\|_2 / \|\mathbf{x}_{\mathbf{ref}}\|_2$ for varying domain sizes. For domains smaller than $N \sim 10^4$ the computed residual and solution errors are nearly equal to the double-precision error (nearly 10^{-16}). This is because for small domains most of the sub-matrices are stored in full format, and thus, there is little loss of accuracy associated with the compression. However, for domains with more than 10^4 unknowns a significant number of sub-matrices become compressible and, as expected, there is a sharp increase in the error from the double precision accuracy to slightly below the threshold value δ. This is because at 10^4 unknowns most of the matrices are being stored to δ accuracy. Beyond 10^4 unknowns the error increases slightly at a constant rate because the error is hierarchically amplified. However, the errors are below the threshold value for the domain sizes we need to analyze, that is, for $N = 10^6$ unknowns with $\delta = 10^{-6}$, $r = 10^{-6}$ and $e = 10^{-8}$. Furthermore, from the results of this test we expect this method to be stable for much bigger domains.

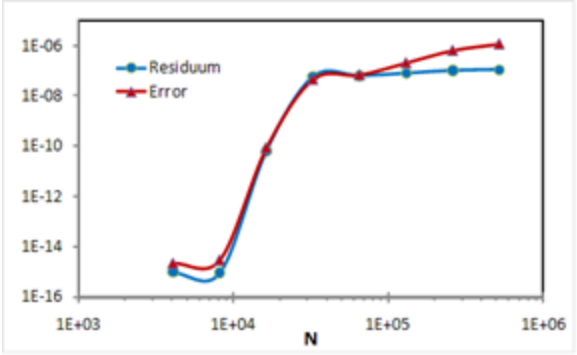

Figure 4.9 Relative residual error and solution error.

4.3.2 TMS Simulation Example

We consider a 'MRI-derived' conductivity model of the human head [Figs. 4.10a-c] generated by segmenting a high resolution MRI image and assigning electrical conductivity values to each tissue type using data from literature [109]. The MRI image consists of $256\times256\times198$ homogenous cubic voxels each having an edge length of 1.2 mm and was obtained by scanning a single male subject in a 3T GE Signa scanner (Waukesha, WI) using an IR-prepped, 3D, SPGR pulse sequence (TR=9.03, TE = 1.84, TI = 500 ms, FOV = 24 cm, slice thickness = 1.2 mm). First, the image is segmented into gray matter, white matter, and ventricular CSF by the SPM5 segmentation toolbox (http://www.fil.ion.ucl.ac.uk/spm). Next, remaining unclassified tissue is further partitioned into another three types, namely bone, muscle, and CSF, by FAST, a component of FSL's image analysis package (http://www.fmrib.ox.ac.uk/fsl/). Each voxel is assigned a conductivity between $3.9\cdot10^{-5}-1.67$ S/m corresponding to the average conductivity of voxel tissue. The resulting conductivity maps are sub-sampled to $128\times128\times99$ voxels with an edge length of 2.4 mm by averaging the conductivity values of each $2\times2\times2$ block of voxels of the original image. To allow for the scalar potential to decay, the computational domain is then padded by placing the brain centered about the mesh and increasing the domain to $158\times158\times129$ voxels by adding air. Air is non-conductive, however, (4.7) is only valid when the conductivity is non-zero. To maintain a hexagonal computational domain, we assume air has a small conductivity σ_{air}, which is several orders of magnitude smaller than the minimum value of conductivity in the head; this replacement has negligible effects on the final value obtained for $\varphi(\mathbf{r})$ using our FD

method. We place a figure-8 coil, consisting of two flat circular coils each with a diameter of 72 mm and centered 7 mm above the head as shown in Fig. 4.10.

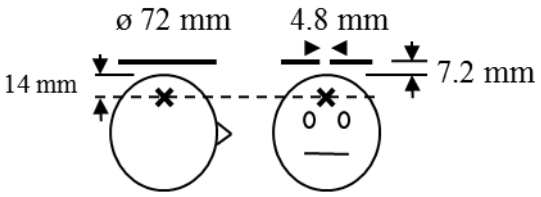

Figure 4.10 Localization and orientation of the figure-8 coil above the head. Coil diameter, coil separation and distance from the head displayed. The dashed line shows position of the axial plane in the results

The system was solved to obtain φ both using an iterative solver and the proposed direct method. To compute the total electric field the gradient of φ is determined by using a central difference and the vector potential is calculated directly using (4.3).

Each simulation was run on multiple cluster nodes a total of 32 CPUs and 20 GB of memory where used. To distribute the memory among each of the cluster nodes we assigned each to each processor of the node one sub-domain Ω_j^4. The observed speedup obtained from this simple parallelization is 2.5 times for the factorization and about 5 times for the solution. A greater speedup can be obtained for this class of problems by using dynamic allocation of resources and a parallel implementation of the $\mathcal{H}$-matrix algebra. The interested reader can find more details about the dynamic allocation in [110].

To compare the performance of the fast direct solver against an iterative method, we used a block-diagonally preconditioned quasi-minimal residual (MINRES) method again with 32CPUs. We split the domain by assigning each processor a subdomain of size $32\times32\times50$. We use a preconditioner composed of the inverse of diagonal blocks of $\mathbf{M}$ each corresponding to one of the $32\times32\times50$ sub-domains using PARDISO. To both

minimize run-time and accurately determine the electric field we chose $\sigma_{air} = 0.01$; this choice of σ_{air} results in 100 iterations to achieve residual of 10^{-4}, and a relative electric field error of 1%, which is in the order of what we would expect from the FD method [36]. Even by optimizing iterative solver parameters to minimize the solution time, the preconditioned iterative solver has a run time of 72 seconds. In contrast, the fast direct solver is runs in less than 4 seconds.

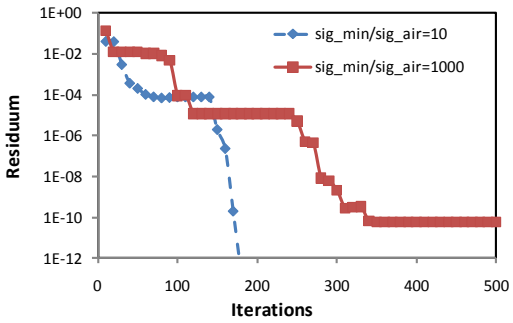

Figure 4.11 Convergence of the iterative solver with a block-diagonal preconditioner.

In Figs. 4.12d-f, the spatial distribution of the total electric field inside the head computed by the direct solver is shown. More importantly, in Figs. 4.12g-i the relative error achieved by the direct solver when compared with an 'exact' solution obtained by letting the iterative solver converge to a residual error of 10^{-12} is shown. Through the head the head the error is around 10^{-5}, however, near the nasal area the error is around 10^{-3}; this is because the nasal area has low-average conductivity and the field varies rapidly near it. Fortunately, the incident field on the nasal area is small relative to other regions and it is not of interest for TMS.

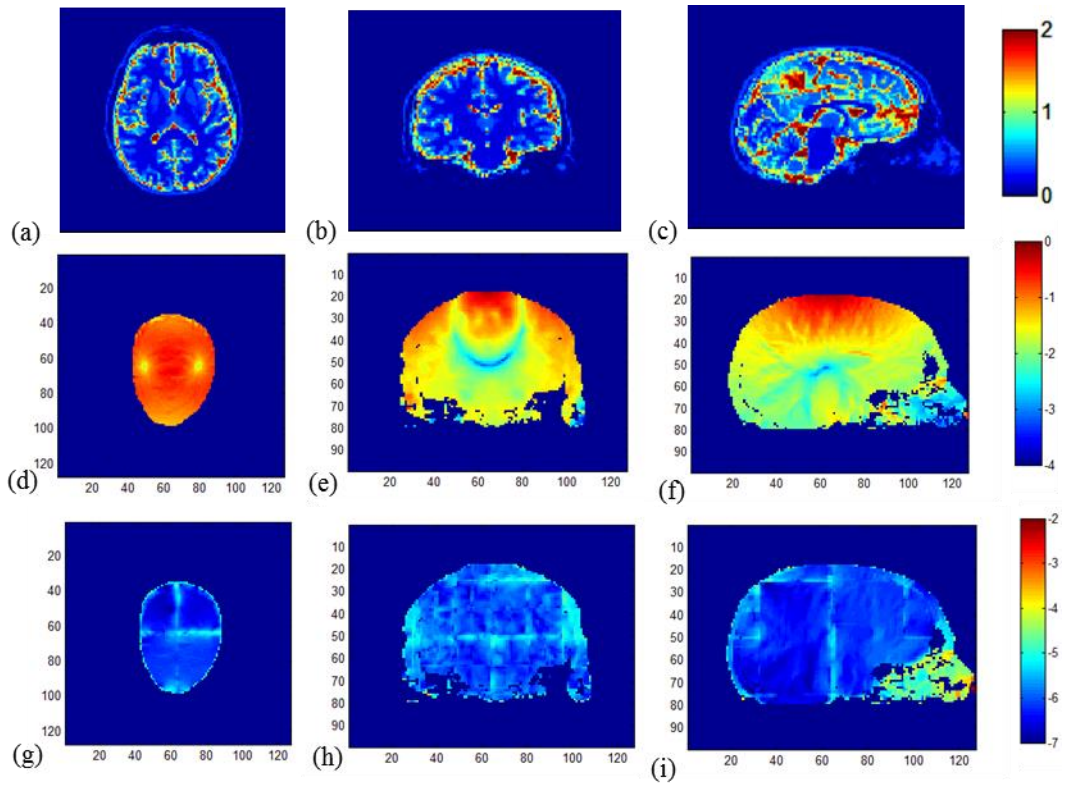

Figure 4.12 Conductivity: (a) transverse plane (b) coronal plane (c) sagittal plane. Magnitude of the total electric field inside the head normalized with respect to the highest value in the head: (d) transverse plane (e) coronal plane (f) sagittal plane. Absolute error of the total electric field inside the head: (g) transverse plane (h) coronal plane (i) sagittal plane

4.3.3 Real Time Coil Positioning

We illustrate how the fast direct solver can be used to find the optimum coil position during TMS. For the results that follow we use the same MRI derived brain and coil as in section 2.3.2. We compute the electric field generated by the coil when placed at different positions relative to the head and determine its effectiveness at targeting a single voxel each time. The target voxel is located on the left dorsal prefrontal cortex, 24 mm below the scalp; this region is often targeted during treatments of depression. Initially, we place the center of the coil 4.8 mm from a point on the scalp that is closest to the target point. Then, we vary its position displacing it by varying azimuthal angles Φ

and Θ relative to the line connecting the target voxel and the initial position, and varying the radius r so that the vertex is always 4.8 mm detached from the scalp [Fig. 4.13].

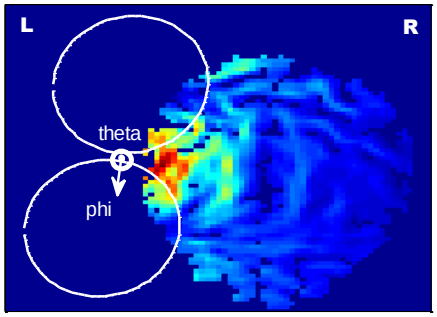

Figure 4.13 Electric field distribution in the axial plane crossing the target point (31 mm below the top of the head). The white circles represent a projection of the figure-8 coil into the plane

We initially position the coil at locations corresponding to all possible combination of the following angles $\phi = -10°, -8°, ..., 10°$ and $\Theta = -10°, -8°, ..., 10°$. Then, to obtain a better estimate of we further refined our search by positioning the coil at all possible combinations of angles $\phi = 6°, 7°, ..., 10°$ degrees and $\Theta = 0°, 1°, ..., 5°$. From these results, we determined the distance between the maximum of the electric field inside the brain and the target voxel. We found that the maximum Electric field inside the brain occurs in regions near the skull nearest to the coil, and since, the target is deep inside the brain the maximum cannot occur on it. The optimal coil position minimizes the distance between the actual maximum and the target. Fig. 4.14 shows the distance between the maximum of electric field and the target voxel for all of the different coil positions tested. The optimal coil position is not directly above the target, as a coil positioning device relying on the primary field would indicate, but displaced by about 4 pixels (that is, at $\phi = 4$ and $\Theta = 4$ degrees); this is because the secondary electric field significantly affects the total field generated. We note that the maximum is less sensitive changes in Θ than ϕ, this is because the electric field of the coil is more sharp in the ϕ direction (cf. Fig. 4.14).

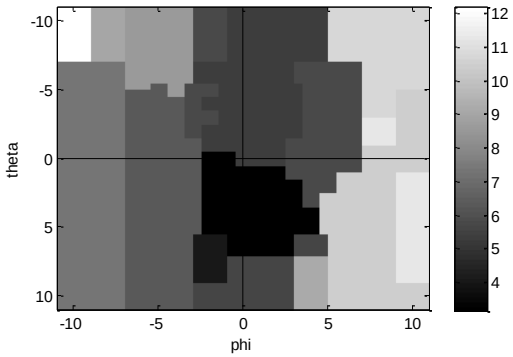

Figure 4.14 Distance between the electric field maxima and the single target for different coil locations. The local directions are defined in Fig. 4.10.

To produce these results, the electric field generated during TMS for 217 different coil positions had to be determined. An iterative solver would have taken about 137 seconds for each coil position and a total of 29,737 seconds to create these results while the direct solver we initially factorized the system in 7997 seconds, then, computed the results for each positions at a rate of 2.2 seconds taking up a total time of 477.4 (less than 8 minutes). In a real time positioning applications the solver could be used in the following way: First, the patient comes in and an MRI image of his brain is collected. Second, a conductivity model of his head and a TMS FD system of equations are created. Then, the system is factorized. Finally, on a second visit, the factorized system can be used to deteremine the optimum coil position for targeting specific regions of the head.

4.3.4 Concluding Remarks

A novel fast direct solver for analyzing TMS phenomena was developed. The solver exploits the hierarchical low-rank nature of sub-blocks of the factorization of the FD matrix pertinent to TMS. The CPU and memory requirements of the proposed solver scale almost linearly in the number of unknowns describing electric fields. Our numerical experiments indicate that the proposed solver's solution step executes faster than that of existing sparse direct solvers for $N > 4 \cdot 10^5$ and is roughly 25 times faster than a preconditioned iterative solver for a typical TMS problem involving $N \sim 10^7$ unknowns. The lower solution time can enable the construction of the frameless stereotactic TMS

systems that account for secondary electric fields when estimating the ideal coil position, thereby significantly improving the targeting accuracy of current TMS systems. Future research will be oriented on the improvement of the code parallelization and on utilization of GPUs that could facilitate the computation of the electric fields in a fraction of a second.

CHAPTER 5
Low-frequency Stable Internally Combined Volume-Surface Integral Equation for High-Contrast Scatterers

5.1 Introduction

Many electromagnetic applications call for the analysis of scattering by inhomogeneous dielectric scatterers. To this end, volume integral equations (VIEs) [111] and volume surface integral equations (VSIEs) [112] are often used. Unfortunately, VIEs suffer from high-contrast (HC) breakdown: when applied to scatterers with electric permittivities that are vastly different from those of the surrounding medium their discretization results in ill-conditioned systems of equations [24, 113]. Ill-conditioning often slows the convergence of iterative solvers, which severely limits the utility of the VIEs in modeling electromagnetic phenomena pertinent to many biological and geophysical applications.

Some VSIEs do not suffer from a HC breakdown. However, VSIEs suffer from a low-frequency (LF) breakdown: when the mesh that discretizes the scatterer contains elements with dimensions that are much smaller than the wavelength, discretization of the VSIE again results in ill-conditioned systems of equations. In this paper, a new internally combined VSIE (ICVSIE) equation that does not suffer from either HC or LF breakdown is introduced [114].

VSIEs eliminate the HC breakdown of the VIE by lowering the maximum contrast of the dielectric scatterer through the use of surface integral equations. First, the scatterer is subdivided into subscatterers each having a small (controlled) ratio of maximum to minimum permittivity. Next, each subscatterer is wrapped in equivalent

electric and magnetic surface currents, and interactions between subscatterers are modeled using surface integral equations in terms of these currents; this procedure also allows for an artificial increase in the effective permittivity of the "background medium" in which the polarization currents of each subscatterer radiate. Finally, the surface and volume currents are determined by numerically solving a system of Volume-Surface Integral Equations (VSIE) consisting of coupled discrete Combined Field Integral Equations (CFIEs) and a VIE. Previously, a Poggio-Miller-Chew-Harrington-Wu-Tsai Combined Field Integral Equation (PMCHWT-CFIE) [115] and a VIE was used to construct a VSIE system of equations [112]. While the resulting VSIE is more accurate than the standard VIE when applied to high-contrast scatterers [112], our numerical results show that it suffers from both HC and LF breakdown. VSIEs can also be formulated using a Muller CFIE [116] on the surface and a VIE. Our numerical results show that the resulting VSIE does not suffer from HC breakdown, however, it still suffers from a LF breakdown. In fact, here it is shown that all VSIE formulations suffer from a LF breakdown due to coupling of the surface currents with the VIE. Furthermore, a method is proposed to make Muller VSIEs LF stable.

The proposed ICVSIE also uses equivalent electric and magnetic surface currents to artificially increase the permittivity of the background medium in which volume polarization currents radiate. A modern discretization of the Muller CFIE [117], which in itself does not suffer from HC or LF breakdowns, is coupled with the VIE. To ensure that the formulation does not suffer from LF breakdown due to coupling of the surface currents with the VIE, contributions due to the surface currents exterior to the scatterer and propagating in the "background medium" are added to the VIE. The resulting formulation does not suffer from either a HC or LF breakdown. While we focus on 2-D time harmonic TE_z implementations, extension of the method to 3-D is straightforward.

This chapter is organized as follows. Section 5.2 introduces notation and presents relevant background material relating to the construction of VIE, VSIE, and ICVSIE. Section 5.3 presents numerical results that demonstrate the effectiveness of the proposed formulation. Section 5.4 summarizes our conclusions and avenues for future research.

5.2 Formulation

5.2.1 Background

Consider an infinite 2-D inhomogeneous dielectric cylinder that resides in a homogenous medium with permittivity ε_b and permeability μ_b, The cylinder is invariant along the $\hat{\mathbf{z}}$-axis, has permittivity $\varepsilon(\boldsymbol{\rho})$ (where $\boldsymbol{\rho} = x\hat{\mathbf{x}} + y\hat{\mathbf{y}}$), which is different from that of its surrounding medium on a cross-section $\boldsymbol{\Omega}$ with boundary $\partial\boldsymbol{\Omega}$ on the x-y plane [Fig.5.1a].

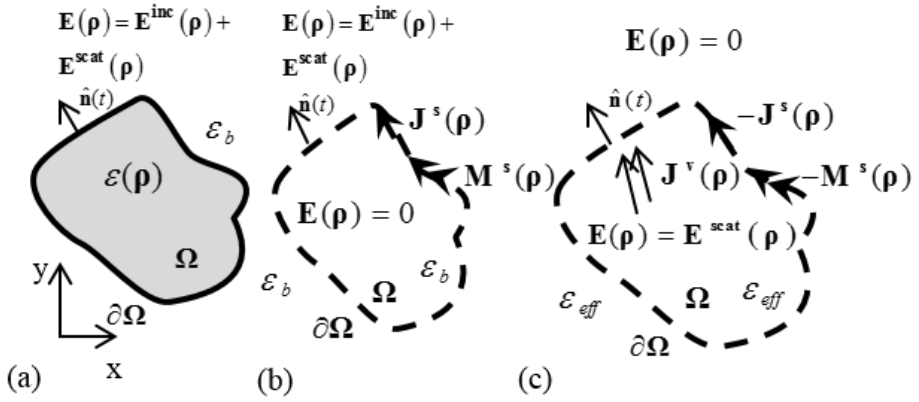

Figure 5.1 (a) Inhomogeneous dielectric body $\boldsymbol{\Omega}$ with electric permittivity $\epsilon(\boldsymbol{\rho})$, surrounded by a medium with electrical permittivity ϵ_b, and illuminated a time-harmonic electric field $\mathbf{E}^{\mathbf{inc}}(\boldsymbol{\rho})$. (b) Equivalent scenario where the whole space is replaced by surface currents $\mathbf{J}^{\mathbf{s}}(\boldsymbol{\rho})$ and $\mathbf{M}^{\mathbf{s}}(\boldsymbol{\rho})$ propagating in a medium with electric permittivity ε_b. (c) Equivalent scenario where the inhomogeneous dielectric body $\boldsymbol{\Omega}$ is replaced by polarization volumetric current density $\mathbf{J}^{\mathbf{v}}(\boldsymbol{\rho})$, and the background permittivity is artificially raised to ε_{eff} by introducing surface currents $-\mathbf{J}^{\mathbf{s}}(\boldsymbol{\rho})$ and $-\mathbf{M}^{\mathbf{s}}(\boldsymbol{\rho})$.

The cylinder is illuminated by TE_z electric and magnetic fields $\mathbf{E}^{\mathbf{inc}}(\boldsymbol{\rho}) = E_x^{inc}(\boldsymbol{\rho})\hat{\mathbf{x}} + E_y^{inc}(\boldsymbol{\rho})\hat{\mathbf{y}}$ and $\mathbf{H}^{\mathbf{inc}}(\boldsymbol{\rho}) = H_z^{inc}(\boldsymbol{\rho})\hat{\mathbf{z}}$, respectively. Interaction of these fields with the cylinder produces scattered electric and magnetic fields $\mathbf{E}^{\mathbf{scat}}(\boldsymbol{\rho})$ and $\mathbf{H}^{\mathbf{scat}}(\boldsymbol{\rho})$ [Fig.5.1a]. (Note: a time dependence $e^{j\omega t}$ is assumed and suppressed). To

determine the total electric and magnetic fields $\mathbf{E}(\boldsymbol{\rho})=\mathbf{E}^{\mathbf{inc}}(\boldsymbol{\rho})+\mathbf{E}^{\mathbf{scat}}(\boldsymbol{\rho})$ and $\mathbf{H}(\boldsymbol{\rho})=\mathbf{H}^{\mathbf{inc}}(\boldsymbol{\rho})+\mathbf{H}^{\mathbf{scat}}(\boldsymbol{\rho})$, volume and surface equivalence principles are invoked to construct equivalent 'exterior' [Fig. 5.1b] and 'interior' [Fig. 5.1c] scenarios. The equivalent exterior scenario consists of incident fields and electric $\mathbf{J}^{\mathbf{s}}(\boldsymbol{\rho})=\hat{\mathbf{n}}\times\mathbf{H}(\boldsymbol{\rho})$ and magnetic $\mathbf{M}^{\mathbf{s}}(\boldsymbol{\rho})=-\hat{\mathbf{n}}\times\mathbf{E}(\boldsymbol{\rho})$ surface currents on $\partial\boldsymbol{\Omega}$ radiating in a homogenous medium with permittivity ε_b and permeability μ_b. These currents together with the incident fields generate $\mathbf{E}(\boldsymbol{\rho})$ and $\mathbf{H}(\boldsymbol{\rho})$ exterior to $\boldsymbol{\Omega}$ and zero fields elsewhere. The interior problem consists of surface currents $-\mathbf{J}^{\mathbf{s}}(\boldsymbol{\rho})$ and $-\mathbf{M}^{\mathbf{s}}(\boldsymbol{\rho})$ on $\partial\boldsymbol{\Omega}$ and a volumetric polarization current $\mathbf{J}^{v}(\boldsymbol{\rho})=jk_{eff}\chi_E^{(eff)}(\boldsymbol{\rho})\mathbf{E}(\boldsymbol{\rho})/\eta_{eff}$ in $\boldsymbol{\Omega}$ radiating in a homogenous medium with permittivity ε_{eff} and permeability μ_b; here $\chi_E^{(eff)}(\boldsymbol{\rho})=\left(\varepsilon(\boldsymbol{\rho})/\varepsilon_{eff}-1\right)$ is the electric contrast. These currents generate $\mathbf{E}(\boldsymbol{\rho})$ and $\mathbf{H}(\boldsymbol{\rho})$ inside $\boldsymbol{\Omega}$ and zero fields elsewhere.

By judiciously combining interior and exterior electric and magnetic field integral operators, a VSIE system of equations for $\mathbf{J}^{\mathbf{s}}(\boldsymbol{\rho})$, $\mathbf{M}^{\mathbf{s}}(\boldsymbol{\rho})$ and $\mathbf{J}^{\mathbf{v}}(\boldsymbol{\rho})$ can be derived. The VSIE

$$\begin{bmatrix} \frac{(\alpha_{ext}-\alpha_{int})}{2}\mathcal{I}-\hat{\mathbf{n}}\times(\alpha_{ext}\mathcal{K}_{\partial\boldsymbol{\Omega}}^{(b)}+\alpha_{int}\mathcal{K}_{\partial\boldsymbol{\Omega}}^{(eff)}) & \hat{\mathbf{n}}\times(\alpha_{ext}\eta_b\mathcal{L}_{\partial\boldsymbol{\Omega}}^{(b)}+\alpha_{int}\eta_{eff}\mathcal{L}_{\partial\boldsymbol{\Omega}}^{(eff)}) & -\hat{\mathbf{n}}\times\alpha_{int}\mathcal{L}_{\boldsymbol{\Omega}}^{(eff)}\chi_E^{(eff)} \\ \hat{\mathbf{n}}\times(\frac{\beta_{ext}}{\eta_b}\mathcal{L}_{\partial\boldsymbol{\Omega}}^{(b)}+\frac{\beta_{int}}{\eta_{eff}}\mathcal{L}_{\partial\boldsymbol{\Omega}}^{(eff)}) & \frac{(\beta_{int}-\beta_{ext})}{2}\mathcal{I}+\hat{\mathbf{n}}\times(\beta_{ext}\mathcal{K}_{\partial\boldsymbol{\Omega}}^{(b)}+\beta_{int}\mathcal{K}_{\partial\boldsymbol{\Omega}}^{(eff)}) & -\hat{\mathbf{n}}\times\beta_{int}\mathcal{K}_{\boldsymbol{\Omega}}^{(eff)}\chi_E^{(eff)} \\ -\mathcal{K}_{\partial\boldsymbol{\Omega}}^{(eff)} & \eta_{eff}\mathcal{L}_{\partial\boldsymbol{\Omega}}^{(eff)} & \mathcal{I}-\mathcal{L}_{\boldsymbol{\Omega}}^{(eff)}\chi_E^{(eff)} \end{bmatrix} \begin{bmatrix} \mathbf{M}^{\mathbf{s}} \\ \mathbf{J}^{\mathbf{s}} \\ \mathbf{E} \end{bmatrix}(\boldsymbol{\rho})=\begin{bmatrix} -\alpha_{ext}\hat{\mathbf{n}}\times\mathbf{E}^{\mathbf{inc}} \\ -\beta_{ext}\hat{\mathbf{n}}\times\mathbf{H}^{\mathbf{inc}} \\ 0 \end{bmatrix}(\boldsymbol{\rho}) \tag{5.1}$$

consists of three equations: 1) α_{int} times an interior surface EFIE plus α_{ext} times an exterior surface EFIE; 2) β_{int} times an interior surface MFIE plus β_{ext} times an exterior surface MFIE; and 3) a VIE equation for $\mathbf{E}(\boldsymbol{\rho})$ inside the scatterer. In (5.1),

$$\begin{aligned} \mathcal{K}_{\partial\Omega}^{(l)}[\mathbf{F}](\boldsymbol{\rho}) &= -p.v.\int_{\partial\Omega}\mathbf{F}(\boldsymbol{\rho}')\times\nabla\frac{\mathrm{H}_0^2\left(k_l|\boldsymbol{\rho}-\boldsymbol{\rho}'|\right)}{4j}d\boldsymbol{\rho}' \\ \mathcal{K}_{\boldsymbol{\Omega}}^{(l)}[\mathbf{F}](\boldsymbol{\rho}) &= -j\frac{k_l}{\eta_l}\int_{\boldsymbol{\Omega}}\mathbf{F}(\boldsymbol{\rho}')\times\nabla\frac{\mathrm{H}_0^2\left(k_l|\boldsymbol{\rho}-\boldsymbol{\rho}'|\right)}{4j}d\boldsymbol{\rho}' \end{aligned}, \tag{5.2}$$

,

$$\begin{aligned}\mathcal{L}_{\partial\Omega}^{(l)}[\mathbf{F}](\boldsymbol{\rho}) &= -jk_l\mathcal{L}_{\partial\Omega}^{s(l)}[\mathbf{F}](\boldsymbol{\rho}) + \frac{1}{jk_l}\mathcal{L}_{\partial\Omega}^{h(l)}[\mathbf{F}](\boldsymbol{\rho}) \\ &= -jk_l\int_{\partial\Omega}\mathbf{F}(\boldsymbol{\rho}')\frac{\mathrm{H}_0^2\left(k_l|\boldsymbol{\rho}-\boldsymbol{\rho}'|\right)}{4j}d\boldsymbol{\rho}' + \frac{1}{jk_l}\int_{\partial\Omega}\nabla'\cdot\mathbf{F}(\boldsymbol{\rho}')\nabla\frac{\mathrm{H}_0^2\left(k_l|\boldsymbol{\rho}-\boldsymbol{\rho}'|\right)}{4j}d\boldsymbol{\rho}'\end{aligned}, \tag{5.3}$$

$$\begin{aligned}\mathcal{L}_{\Omega}^{(l)}[\mathbf{F}](\boldsymbol{\rho}) &= k_l{}^2\mathcal{L}_{\Omega}^{s(l)}[\mathbf{F}](\boldsymbol{\rho}) + \mathcal{L}_{\Omega}^{h(l)}[\mathbf{F}](\boldsymbol{\rho}) \\ &= k_l{}^2\int_{\Omega}\mathbf{F}(\boldsymbol{\rho}')\frac{\mathrm{H}_0^2\left(k_l|\boldsymbol{\rho}-\boldsymbol{\rho}'|\right)}{4j}d\boldsymbol{\rho}' + \int_{\Omega}(\nabla'\cdot\mathbf{F}(\boldsymbol{\rho}'))\nabla\frac{\mathrm{H}_0^2\left(k_l|\boldsymbol{\rho}-\boldsymbol{\rho}'|\right)}{4j}d\boldsymbol{\rho}'\end{aligned}, \tag{5.4}$$

and $\mathcal{I}$ is the identity operator. In the above equations, $k_l = \omega\sqrt{\varepsilon_l\mu_l}$ and $\eta_l = \sqrt{\mu_l/\varepsilon_l}$ are the wavenumber and characteristic impedance of a medium with permittivity ε_l and permeability μ_l; both $\mathcal{K}_{\partial\Omega}^{(l)}$ and $\mathcal{K}_{\Omega}^{(l)}$ are magnetic field integral operators; $\mathcal{L}_{\partial\Omega}^{(l)}$ and $\mathcal{L}_{\Omega}^{(l)}$ are surface and volume electric field integral operators, each of which is composed of smoothing ($\mathcal{L}_{\partial\Omega}^{s(l)}$ or $\mathcal{L}_{\Omega}^{s(l)}$) and singular ($\mathcal{L}_{\partial\Omega}^{h(l)}$ or $\mathcal{L}_{\Omega}^{h(l)}$) terms; $\mathrm{H}_0^2(\cdot)$ is the zeroth-order Hankel function of the second kind, and *p.v.* indicates principal value. Parameters α_{ext}, α_{int}, β_{ext}, and β_{int} in principle can be chosen arbitrarily. In practice they are carefully chosen to ensure that the 2×2 top-left diagonal sub-block of the matrix that arises upon discretization of (5.1) is 'well-conditioned' under various conditions. In [112], α_{ext}, β_{ext}, α_{int} and β_{int} are all set to one (known as the PMCHWT-CFIE); this choice leads to a resonance-free VSIE system of equations, which unfortunately suffers from HC and LF breakdown. The HC breakdown can be removed by choosing $\alpha_{int} = \varepsilon_{eff}$, $\beta_{int} = \mu_b$, $\alpha_{ext} = -\varepsilon_b$, and $\beta_{ext} = -\mu_b$ (known as the Muller-CFIE).

Independent of the choice of α_{ext}, α_{int}, β_{ext} and β_{int}, (5.1) always suffers from a LF breakdown. This is because as $\omega\to 0$: $\eta_{eff}\mathcal{L}_{\partial\Omega}^{s(eff)} \sim O(\omega)$, $\eta_{eff}\mathcal{L}_{\partial\Omega}^{h(eff)} \sim O(1/\omega)$, $\mathcal{K}_{\partial\Omega}^{(eff)} \sim O(1)$ and $(\mathcal{I} - \mathcal{L}_{\Omega}^{(eff)}\chi_E^{(eff)}) \sim O(1)$, and thus, as $\omega\to 0$, the singular surface term $\eta_{eff}\mathcal{L}_{\partial\Omega}^{h(eff)}$ in the third row of (5.1) becomes dominant. In the exterior problem [Fig.5.1b] the electric field generated by the surface currents inside $\boldsymbol{\Omega}$ is $-\mathbf{E}^{\mathbf{inc}}(\boldsymbol{\rho})$. To remove the LF breakdown from (5.1), $\mathbf{E}^{\mathbf{inc}}(\boldsymbol{\rho})$ is added to the third row of (5.1). The final ICVSIE system of equations is

$$\begin{bmatrix} \frac{(\alpha_{ext}-\alpha_{int})}{2}\mathcal{I}-\hat{\mathbf{n}}\times(\alpha_{ext}\mathcal{K}_{\partial\Omega}^{(b)}+\alpha_{int}\mathcal{K}_{\partial\Omega}^{(eff)}) & \hat{\mathbf{n}}\times(\alpha_{ext}\eta_b\mathcal{L}_{\partial\Omega}^{(b)}+\alpha_{int}\eta_{eff}\mathcal{L}_{\partial\Omega}^{(eff)}) & -\hat{\mathbf{n}}\times\alpha_{int}\mathcal{L}_{\Omega}^{(eff)}\chi_E^{(eff)} \\ \hat{\mathbf{n}}\times(\frac{\beta_{ext}}{\eta_b}\mathcal{L}_{\partial\Omega}^{(b)}+\frac{\beta_{int}}{\eta_{eff}}\mathcal{L}_{\partial\Omega}^{(eff)}) & \frac{(\beta_{int}-\beta_{ext})}{2}\mathcal{I}+\hat{\mathbf{n}}\times(\beta_{ext}\mathcal{K}_{\partial\Omega}^{(b)}+\beta_{int}\mathcal{K}_{\partial\Omega}^{(eff)}) & -\hat{\mathbf{n}}\times\beta_{int}\mathcal{K}_{\Omega}^{(eff)}\chi_E^{(eff)} \\ -(\xi_{ext}\mathcal{K}_{\partial\Omega}^{(b)}+\xi_{int}\mathcal{K}_{\partial\Omega}^{(eff)}) & (\xi_{ext}\eta_b\mathcal{L}_{\partial\Omega}^{(b)}+\xi_{int}\eta_{eff}\mathcal{L}_{\partial\Omega}^{(eff)}) & \xi_{int}(\mathcal{I}-\mathcal{L}_{\Omega}^{(eff)}\chi_E^{(eff)}) \end{bmatrix} \cdot$$

$$\begin{bmatrix} \mathbf{M}^s \\ \mathbf{J}^s \\ \mathbf{E} \end{bmatrix}(\boldsymbol{\rho}) = \begin{bmatrix} -\alpha_{ext}\hat{\mathbf{n}}\times\mathbf{E}^{inc} \\ -\beta_{ext}\hat{\mathbf{n}}\times\mathbf{H}^{inc} \\ -\xi_{ext}\mathbf{E}^{inc} \end{bmatrix}(\boldsymbol{\rho})$$

(5.5)

If $\xi_{int}=\varepsilon_{eff}$, and $\xi_{ext}=-\varepsilon_b$ (i.e. as in the Muller-CFIE), then as $\omega\to 0$ the operators: $\varepsilon_b\eta_b\mathcal{L}_{\partial\Omega}^{s(b)}-\varepsilon_{eff}\eta_{eff}\mathcal{L}_{\partial\Omega}^{s(eff)}\sim O(\omega)$, $-\varepsilon_{eff}(\mathcal{I}-\mathcal{L}_{\Omega}^{(eff)}\chi_E^{(eff)})\sim O(1)$, $\varepsilon_b\eta_b\mathcal{L}_{\partial\Omega}^{h(b)}-\varepsilon_{eff}\eta_{eff}\mathcal{L}_{\partial\Omega}^{h(eff)}\sim O(\omega)$ and $\varepsilon_b\mathcal{K}_{\partial\Omega}^{(b)}-\varepsilon_{eff}\mathcal{K}_{\partial\Omega}^{(eff)}\sim O(1)$; thus, the smoothing and hyper-singular terms of the surface electric field operators both scale as ω and (5.2) does not suffer from a LF breakdown. Note: for a given mesh density the surface currents resulting from solving a Muller-CFIE are known to be less accurate than those determined from solving a PMCHWT-CFIE. To achieve an ICVSIE that is both accurate and stable, it would be advantageous to construct a Calderon preconditioned PMCHWT-ICVSIE, using a CFIE analogous to the one described in [118].

5.2.2 Discrete Formulation

To solve the ICVSIE we approximate $\boldsymbol{\Omega}$ with a mesh of triangles and $\partial\boldsymbol{\Omega}$ with the edges on the surface of the discrete scatterer. (NOTE: From a numerical standpoint it has been found that there is no significant difference when we solve for $\mathbf{D}(\boldsymbol{\rho})$, or $\mathbf{E}(\boldsymbol{\rho})$, however, in a proper discretization of $\mathbf{E}(\boldsymbol{\rho})$ there are boundary integrals on the surfaces of all elements of the mesh, which increases the setup cost in a numerical approximation of (5.5); thus, we span $\mathbf{D}(\boldsymbol{\rho})$ in the discrete formulation.) First, we approximate the surface electric current density $\mathbf{J}^s(\boldsymbol{\rho})$, surface magnetic current density $\mathbf{M}^s(\boldsymbol{\rho})$, and the volumetric electric flux $\mathbf{D}(\boldsymbol{\rho})$ as

$$\mathbf{J}^{s}(\boldsymbol{\rho})=\sum_{j=1}^{N_s} J_j\, t_j(\boldsymbol{\rho}) \tag{5.6}$$

$$\mathbf{M}^{s}(\boldsymbol{\rho})=\sum_{j=1}^{N_s} M_j\, \hat{\mathbf{n}}\times t_j(\boldsymbol{\rho}) \tag{5.7}$$

$$\mathbf{D}(\boldsymbol{\rho})=\sum_{j=1}^{N_v} D_j\, RWG_j(\boldsymbol{\rho}) \tag{5.8}$$

where $t_i(\boldsymbol{\rho})$ is a triangle basis function [119], $RWG_i(\boldsymbol{\rho})$ is Rao-Wilton-Glisson basis function [120], N_s are the number of nodes on the boundary of the discrete scatterer, and N_v are the number of edges of the discrete scatterer. Then, we test (5.5), using the Galerkin testing method and $\hat{\mathbf{n}}\times t(\boldsymbol{\rho})$, $t(\boldsymbol{\rho})$, and $RWG(\boldsymbol{\rho})$, respectively. This results in:

$$\begin{bmatrix} \alpha_{ext}\eta_b\mathbf{Z}^{(b)}_{\mathbf{J},\mathbf{J}}+\alpha_{\mathrm{int}}\eta_{eff}\mathbf{Z}^{(eff)}_{\mathbf{J},\mathbf{J}} & \frac{(\alpha_{ext}-\alpha_{int})}{2}\mathbf{I}-(\alpha_{ext}\mathbf{Z}^{(b)}_{\mathbf{J},\mathbf{M}}+\alpha_{\mathrm{int}}\mathbf{Z}^{(eff)}_{\mathbf{J},\mathbf{M}}) & -\alpha_{int}\eta_{eff}\mathbf{Z}^{(eff)}_{\mathbf{J},\mathbf{D}} \\ \frac{-\beta_{ext}+\beta_{int}}{2}\mathbf{I}+(\beta_{ext}\mathbf{Z}^{(b)}_{\mathbf{M},\mathbf{J}}+\beta_{int}\mathbf{Z}^{(eff)}_{\mathbf{M},\mathbf{J}}) & \frac{\beta_{ext}}{\eta_b}\mathbf{Z}^{(b)}_{\mathbf{M},\mathbf{M}}+\frac{\beta_{int}}{\eta_{eff}}\mathbf{Z}^{(eff)}_{\mathbf{M},\mathbf{M}} & -\beta_{int}\mathbf{Z}^{(eff)}_{\mathbf{M},\mathbf{D}} \\ \xi_{ext}\eta_b\mathbf{Z}^{(b)}_{\mathbf{D},\mathbf{J}}+\xi_{int}\eta_{eff}\mathbf{Z}^{(eff)}_{\mathbf{D},\mathbf{J}} & -(\xi_{ext}\mathbf{Z}^{(b)}_{\mathbf{D},\mathbf{M}}+\xi_{int}\mathbf{Z}^{(eff)}_{\mathbf{D},\mathbf{M}}) & -\xi_{int}\eta_{eff}\mathbf{Z}^{(eff)}_{\mathbf{D},\mathbf{D}} \end{bmatrix}, \tag{5.9}$$

$$\begin{bmatrix}\mathbf{J}\\ \mathbf{M}\\ \mathbf{D}\end{bmatrix}=\begin{bmatrix}\alpha_{ext}\mathbf{E}^{\mathbf{inc}}\\ \beta_{ext}\mathbf{H}^{\mathbf{inc}}\\ \xi_{ext}\mathbf{E}^{\mathbf{inc}}_{\mathbf{v}}\end{bmatrix}$$

Where,

$$\left(\mathbf{Z}^{(l)}_{\mathbf{J},\mathbf{J}}\right)_{i,j}=\left\langle \hat{\mathbf{n}}_{\mathrm{i}}\times \mathrm{t}_{\mathrm{i}}(\boldsymbol{\rho}), \hat{\mathbf{n}}_{\mathrm{i}}\times \mathcal{L}^{(l)}_{\partial\Omega}[\mathrm{t}_{\mathrm{j}}(\boldsymbol{\rho}')](\boldsymbol{\rho})\right\rangle,$$

$$\left(\mathbf{Z}^{(l)}_{\mathbf{J},\mathbf{M}}\right)_{i,j}=\left\langle \hat{\mathbf{n}}_{\mathbf{i}}\times \mathrm{t}_{\mathrm{i}}(\boldsymbol{\rho}), \hat{\mathbf{n}}_{\mathbf{i}}\times \mathcal{K}^{(l)}_{\partial\Omega}[\vec{\mathbf{n}}_{\mathrm{j}}\times \mathrm{t}_{\mathrm{j}}(\boldsymbol{\rho}')](\boldsymbol{\rho})\right\rangle,$$

$$\left(\mathbf{Z}^{(l)}_{\mathbf{J},\mathbf{D}}\right)_{\mathrm{i,j}}=\left\langle \hat{\mathbf{n}}_{\mathbf{i}}\times \mathrm{t}_{\mathrm{i}}(\boldsymbol{\rho}), \hat{\mathbf{n}}_{\mathbf{i}}\times \mathcal{L}^{(l)}_{\Omega}[\frac{\chi(\boldsymbol{\rho}';\varepsilon_l)}{\varepsilon(\boldsymbol{\rho}')}\mathrm{RWG}_{\mathrm{j}}(\boldsymbol{\rho}')](\boldsymbol{\rho})\right\rangle,$$

$$\left(\mathbf{Z}^{(l)}_{\mathbf{M},\mathbf{J}}\right)_{i,j}=\left\langle \mathrm{t}_{\mathrm{i}}(\boldsymbol{\rho}), \hat{\mathbf{n}}_{\mathbf{i}}\times \mathcal{K}^{(l)}_{\partial\Omega}[\mathrm{t}_{\mathrm{j}}(\boldsymbol{\rho}')](\boldsymbol{\rho})\right\rangle,$$

$$\left(\mathbf{Z}^{(l)}_{\mathbf{M},\mathbf{M}}\right)_{i,j}=\left\langle \mathrm{t}_{\mathrm{i}}(\boldsymbol{\rho}), \hat{\mathbf{n}}_{\mathbf{i}}\times \mathcal{L}^{(l)}_{\partial\Omega}[\hat{\mathbf{n}}_{\mathbf{j}}\times \mathrm{t}_{\mathrm{j}}(\boldsymbol{\rho}')](\boldsymbol{\rho})\right\rangle,$$

$$\left(\mathbf{Z}^{(l)}_{\mathbf{M},\mathbf{D}}\right)_{\mathrm{i,j}}=\left\langle \mathrm{t}_{\mathrm{i}}(\boldsymbol{\rho}), \hat{\mathbf{n}}_{\mathbf{i}}\times \mathcal{K}^{(l)}_{\partial\Omega}[\frac{\chi(\boldsymbol{\rho}';\varepsilon_l)}{\varepsilon(\boldsymbol{\rho}')}\mathrm{RWG}_{\mathrm{j}}(\boldsymbol{\rho}')](\boldsymbol{\rho})\right\rangle,$$

$$\left(\mathbf{Z}_{\mathbf{D,J}}^{(l)}\right)_{\mathrm{i,j}} = \left\langle \mathrm{RWG}_{\mathrm{i}}(\boldsymbol{\rho}), \mathcal{L}_{\partial\Omega}^{(l)}[\mathrm{t}_{\mathrm{j}}(\boldsymbol{\rho}')](\boldsymbol{\rho}) \right\rangle ,$$

$$\left(\mathbf{Z}_{\mathbf{D,M}}^{(l)}\right)_{\mathrm{i,j}} = \left\langle \mathrm{RWG}_{i}(\boldsymbol{\rho}), \mathcal{K}_{\partial\Omega}^{(l)}[\hat{\mathbf{n}}_{\mathrm{j}} \times \mathrm{t}_{\mathrm{j}}(\boldsymbol{\rho}')](\boldsymbol{\rho}) \right\rangle,$$

$$\left(\mathbf{Z}_{\mathbf{D,D}}^{(l)}\right)_{\mathrm{i,j}} = \frac{-1}{\eta_l}\left\langle \mathrm{RWG}_{\mathrm{i}}(\boldsymbol{\rho}), \frac{\mathrm{RWG}_{\mathrm{j}}(\boldsymbol{\rho})}{\varepsilon(\mathbf{r})} \right\rangle + \left\langle \mathrm{RWG}_{\mathrm{i}}(\boldsymbol{\rho}), \mathcal{L}_{\Omega}^{(l)}[\frac{\chi(\boldsymbol{\rho}';\varepsilon_l)}{\varepsilon(\boldsymbol{\rho}')} \mathrm{RWG}_{\mathrm{j}}(\boldsymbol{\rho}')](\boldsymbol{\rho}) \right\rangle,$$

$$\left(\mathbf{E}^{\mathbf{inc}}\right)_{\mathrm{i}} = \left\langle \hat{\mathbf{n}}_{\mathrm{i}} \times \mathrm{t}_{\mathrm{i}}(\boldsymbol{\rho}), \hat{\mathbf{n}}_{\mathrm{i}} \times \mathbf{E}^{\mathbf{inc}}(\boldsymbol{\rho}) \right\rangle ,$$

$$\left(\mathbf{H}^{\mathbf{inc}}\right)_{\mathrm{i}} = \left\langle \mathrm{t}_{\mathrm{i}}(\boldsymbol{\rho}), \hat{\mathbf{n}}_{\mathrm{i}} \times \mathbf{H}^{\mathbf{inc}}(\boldsymbol{\rho}) \right\rangle ,$$

$$\left(\mathbf{E}_{\mathbf{v}}^{\mathbf{inc}}\right)_{\mathrm{i}} = \left\langle RWG_{\mathrm{i}}(\boldsymbol{\rho}), \mathbf{E}^{\mathbf{inc}}(\boldsymbol{\rho}) \right\rangle ,$$

and

$$\left\langle \mathbf{A}(\boldsymbol{\rho}), \mathbf{B}(\boldsymbol{\rho}) \right\rangle = \int \mathbf{A}(\boldsymbol{\rho}) \cdot \mathbf{B}(\boldsymbol{\rho}) d\mathbf{r} .$$

We store (5.9) in full-format and compute the self-terms using the singularity-subtraction technique previously described in [121]. The performance of the ICVSIE is compared with that of the VIE (i.e. $(\mathcal{I} - \mathcal{L}_{\Omega}^{(b)}\chi_E^{(b)})\mathbf{E}(\boldsymbol{\rho}) = \mathbf{E}^{\mathbf{inc}}(\boldsymbol{\rho})$) and various VSIE formulations [Table I]. The latter are constructed by choosing popular combinations of α_{ext}, α_{int}, β_{ext}, β_{int}, ξ_{ext}, ξ_{int}, and $\epsilon_{eff} = \min(\epsilon(\boldsymbol{\rho}))$, and choosing either $\mathbf{E}(\boldsymbol{\rho})$ or the electric flux $\mathbf{D}(\boldsymbol{\rho}) = \varepsilon(\boldsymbol{\rho})\mathbf{E}(\boldsymbol{\rho})$ as the volumetric source unknown [Table 5.1].

Equation	$(\alpha_{ext}, \alpha_{int}, \beta_{ext}, \beta_{int}, \xi_{\mathbf{ext}}, \xi_{\mathbf{int}})$	$\mathbf{J}^v$ field associated unknown	HC Breakdown	LF Breakdown
VIE [24]	(N/A, N/A, N/A, N/A,N/A,1)	**D**	Yes	No
PMCHWT VSIE-E [112]	(1,1,1,1,0 ,1)	**E**	Yes	Yes
PMCHWT VSIE-D	(1,1,1,1,0 ,1)	**D**	Yes	Yes
Muller VSIE-E	$(-\varepsilon_b, \varepsilon_{eff}, -\mu_b, \mu_b, 0, 1)$	**E**	No	Yes
Muller VSIE-D	$(-\varepsilon_b, \varepsilon_{eff}, -\mu_b, \mu_b, 0, 1)$	**D**	No	Yes
ICVSIE	$(-\varepsilon_b, \varepsilon_{eff}, -\mu_b, \mu_b, -\varepsilon_b, \varepsilon_{eff})$	**D**	No	No

Table 5.1 Integral equation Formulations

5.3 Results and Discussions

This section, presents examples that demonstrate the effectiveness of the proposed method for the analysis of both electrically small and large strongly-inhomogeneous highly-heterogeneous objects.

All numerical experiments below involve a four layer circular cylinder that has a total radius r and layer radii $r/4$, $r/2$, $3r/4$ and r. The cylinder is approximated by a mesh consisting of 1208 triangles, 1850 edges, and a maximum edge length of $0.12r$. The cylinder resides in a free space background medium with permittivity $\varepsilon_b = \varepsilon_0$ and permeability $\mu_b = \mu_0$. For iterative convergence and accuracy tests, it is assumed that the cylinder is illuminated by a uniform TE_z plane-wave propagating along the $-\hat{\mathbf{x}}$ direction and a Transpose Free Quasi-minimal Residual (TFQMR) method [122] is used to solve each system of equations to a residual error of 10^{-5}.

LF Breakdown: Consider layered cylinders with total radius of $r = 10^{-4}, 10^{-5}, ..., 10^{-9}\ \lambda_0$ having layers (inner to outer) with electric permittivities of $3\times10^4\varepsilon_0$, $10^4\varepsilon_0$, $2\times10^4\varepsilon_0$ and $4\times10^4\varepsilon_0$. The condition number (i.e. the ratio of the maximum singular value to the minimum singular value) of the VIE, VSIEs, and ICVSIE systems of equations for each cylinder are shown in Fig. 5.2a. The condition numbers of the VIE and the ICVSIE are relatively constant functions of r, while the condition numbers of all the VSIEs are inversely proportional to r. In contrast to all VSIE formulations, the proposed ICVSIE does not exhibit any LF breakdown.

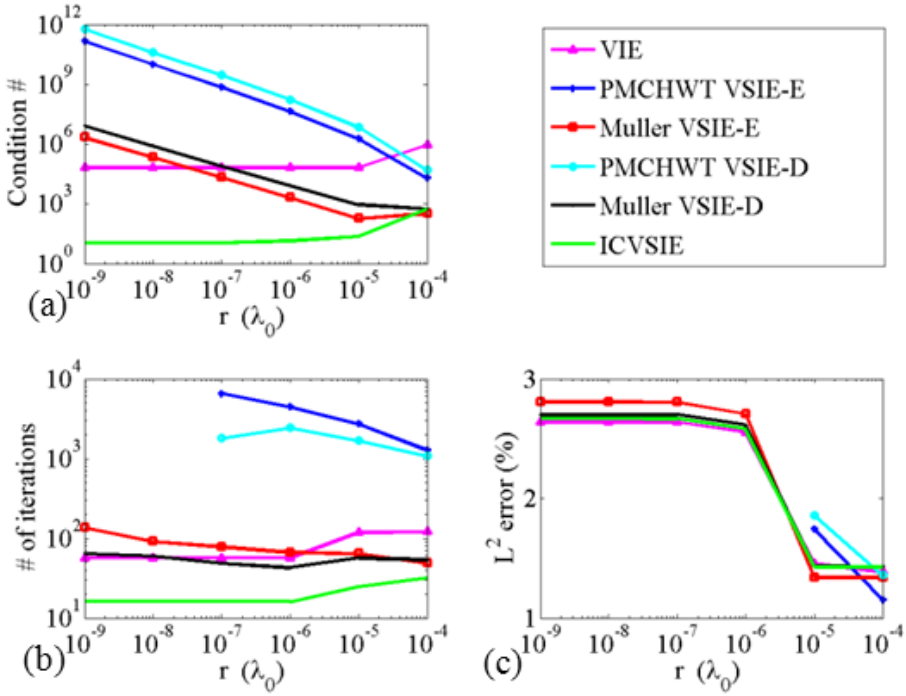

Figure 5.2 (a) Condition number of systems of equations as a function of electrical size (b) number of iterations for TFQMR procedure to reach a RRE of 10^{-5} as a function of electrical size (c) The relative L^2 norm error of the electric field inside the scatterer as a function of electrical size.

The effectiveness of TFQMR for solving the discretized VIE, VSIEs, and ICVSIE systems of equations is compared. For each cylinder, discretized VIE, VSIEs, and ICVSIE systems of equations are solved using TFQMR. The total number of iterations required to converge are given in Fig. 5.2b. The number of iterations for the VIE and the ICVSIE are relatively constant functions of r, while the number of iterations for all other formulations increase with decreasing r. The PMCHWT VSIEs requires the most iterations and for $r = 10^{-8}\lambda_0$ and $r < 10^{-9}\lambda_0$ TFQMR does not converge. For all r, the ICVSIE requires the least number of iterations and for the smallest $r = 10^{-9}\lambda_0$ the ICVSIE requires more than 3.5 times less iterations than all other methods. Fig. 5.2b demonstrates the clear benefit of using the ICVSIE as opposed to the VIE or any other VSIE for electrically small and high-permittivity scatterers.

The relative L^2 norm error of the electric field inside each of the scatters is shown in Fig.5.2c. As the electrical size of the cylinder decreases the PMCHWT VSIEs become

less accurate and for cylinders with $r < 10^{-5}\lambda_0$ the relative L^2 norm error is above 10% and it is not shown. All of the other formulations exhibit similar and nearly constant relative L^2 norm error ranging from 1.3% and 2.8%. The VIE, Muller VSIEs and ICVSIE are suitable for accurately analyzing electrically small and high-contrast scatterers.

HC breakdown: Next the dependence of the condition number of the discretized VIE, VSIEs, and ICVSIE systems of equations on the maximum permittivity is studied. Consider four concentric layer cylinders each with total radius $\lambda_0 / 4\sqrt{\varepsilon_{\max}}$ and having layers (inner to outer) with electric permittivity $3\varepsilon_{\max}/4$, $\varepsilon_{\max}/2$, $\varepsilon_{\max}/4$ and $\varepsilon_{\max}$, where $\varepsilon_{\max} = 4\varepsilon_0, 4\times 10\varepsilon_0, ..., 4\times 10^6 \varepsilon_0$. The condition number of the VIE, VSIEs, and ICVSIE systems of equations for each cylinder are shown in Fig.5.3a. The condition number of the VIE, and PMCHWT VSIEs [112] grows linearly with ϵ_r. The condition number of both the Muller VSIE and ICVSIE are relatively constant as a function of $\varepsilon_{\max}$. All the Muller VSIE formulations and the proposed ICVSIE do not exhibit any HC breakdown. The average condition number of the ICVSIE is 13.5, which is significantly lower than the 73.6 (and 48.1) of the Muller VSIE with $\mathbf{D}$ (and $\mathbf{E}$) as volumetric unknown.

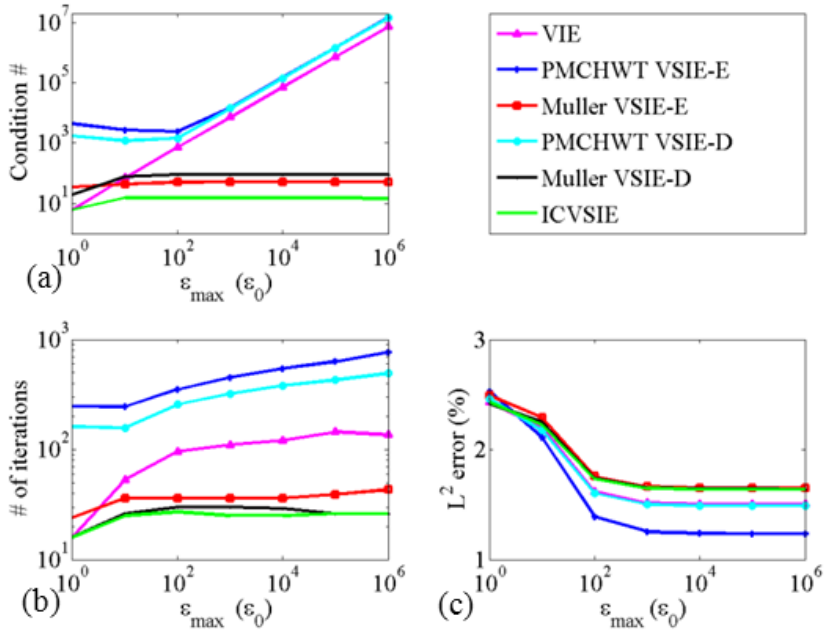

Figure 5.3 (a) Condition number of systems of equations as a function of maximum electric permittivity (b) number of iterations for TFQMR procedure to reach a RRE of

10^{-5} as a function of maximum electric permittivity (c) The relative L^2 norm error of the electric field inside the scatterer as a function of maximum electric permittivity.

The effectiveness of TFQMR for solving the discretized VIE, VSIEs, and ICVSIE systems of equations is compared. For each cylinder, discretized VIE, VSIEs, and ICVSIE systems of equations are solved using TFQMR and the total number of iterations required to converge are shown in Fig. 5.3b. The number of iterations for the Muller VSIEs and the ICVSIE are relatively constant functions of $\varepsilon_{\max}$, while the number of iterations for all other formulations increase with increasing $\varepsilon_{\max}$. Again for all $\varepsilon_{\max}$, the ICVSIE requires the least number of iterations. Fig. 5.3b demonstrates the clear benefit of using the ICVSIE as opposed to the VIE or any other VSIE for high-permittivity scatterers.

The relative L^2 norm error of the electric field inside each of the scatters for each formulation is shown in Fig. 5.3c. The error decreases slightly as $\varepsilon_{\max}$ increases. For small $\varepsilon_{\max}$ all formulations give a similar error. Overall the PMCHWT VSIE-E is slightly more accurate than all the other formulations. For example, for $\varepsilon_{\max} = 4 \times 10^6 \varepsilon_0$ the PMCHWT VSIE-E achieves an error of 1.2% and the ICVSIE an error of 1.6%. The VIE, VSIEs and ICVSIE are all suitable for accurately analyzing high-contrast scatterers.

5.4 Conclusions

We presented and computationally verified a novel approach for computing electromagnetic fields inside heterogeneous high-contrast scatterers. Unlike previous VIE and VSIE approaches, our method does not suffer from high-contrast or low-frequency breakdown. While the method as presented is suitable only for weakly inhomogeneous cylinders, it can be extended to strongly inhomogeneous scatterers by introducing additional surface variables on interfaces between volumes with vastly different permittivities. An extension of such a scheme in 3-D is shown in chapter 6.

CHAPTER 6
3D Internally Combined Volume-Surface Integral Equation

6.1 Introduction

In the previous chapters the ICVSIE was introduced and it was shown that the ICVSIE is low-frequency stable for the analysis of scattering by high-contrast and negative permittivity infinitely long cylinders. In this chapter, the ICVSIE is shown to exhibit the same properties for general 3D structures. More importantly, it is used to determine the electric fields generated during TMS.

This chapter is organized as follows. Section 6.2 introduces notation and presents relevant background material relating to the construction of VIE, VSIE, and ICVSIE. Section 6.3 presents numerical results that demonstrate the effectiveness of the proposed formulation. Section 6.4 summarizes our conclusions and avenues for future research.

6.2 Formulation

6.2.1 Background

Consider an inhomogeneous dielectric object that resides in a homogenous background medium with permittivity ε_b and permeability μ_b. The inhomogeneous object has permittivity $\varepsilon(\mathbf{r})$, $\mathbf{r}=x\hat{\mathbf{x}}+y\hat{\mathbf{y}}+z\hat{\mathbf{z}}$, and resides in a domain $\boldsymbol{\Omega}$ with boundary $\partial\boldsymbol{\Omega}$ and outward pointing normal $\hat{\mathbf{n}}$ [Fig. 6.1a]. (Note: Through this chapter, a time dependence $e^{j\omega t}$ is assumed and suppressed.)

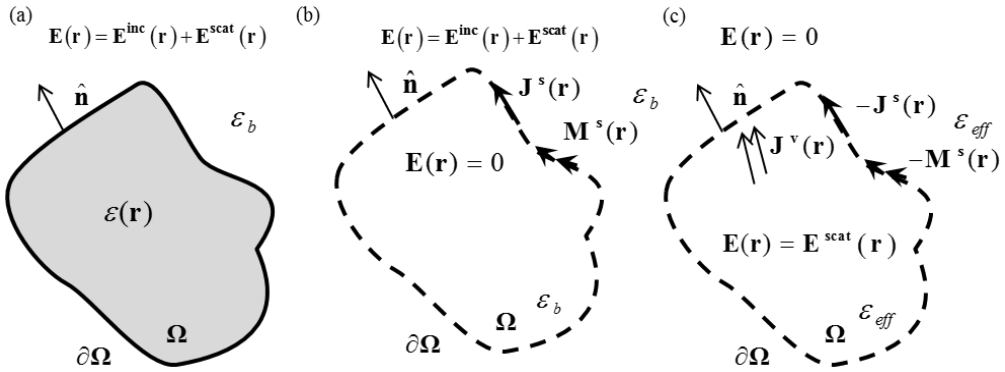

Figure 6.1 (a) Scattering scenario (b) equivalent exterior scenario (c) equivalent interior scenario.

Whenever the object is illuminated by incident time-harmonic electric and magnetic fields $\mathbf{E}^{\text{inc}}(\mathbf{r})$ and $\mathbf{H}^{\text{inc}}(\mathbf{r})$, respectively. The dielectric object generates scattered electric and magnetic fields $\mathbf{E}^{\text{scat}}(\mathbf{r})$ and $\mathbf{H}^{\text{scat}}(\mathbf{r})$ [Fig. 6.1a]. The total electric and magnetic fields are $\mathbf{E}(\mathbf{r})=\mathbf{E}^{\text{inc}}(\mathbf{r})+\mathbf{E}^{\text{scat}}(\mathbf{r})$ and $\mathbf{H}(\mathbf{r})=\mathbf{H}^{\text{inc}}(\mathbf{r})+\mathbf{H}^{\text{scat}}(\mathbf{r})$. To determine $\mathbf{E}(\mathbf{r})$ and $\mathbf{H}(\mathbf{r})$, volume and surface equivalence principles are invoked to construct equivalent 'exterior' [Fig. 6.1b] and 'interior' [Fig. 6.1c] scenarios. The equivalent exterior scenario consists of incident fields and electric $\mathbf{J}^{s}(\mathbf{r})=\hat{\mathbf{n}}\times\mathbf{H}(\mathbf{r})$ and magnetic $\mathbf{M}^{s}(\mathbf{r})=-\hat{\mathbf{n}}\times\mathbf{E}(\mathbf{r})$ surface currents on $\partial\Omega$ radiating in a homogenous medium with permittivity ε_b and permeability μ_b. These currents together with the incident fields generate $\mathbf{E}(\mathbf{r})$ and $\mathbf{H}(\mathbf{r})$ exterior to Ω and zero fields elsewhere. The exterior electric field integral equation (EFIE) and magnetic field integral equation (MFIE) and VIE can be derived by evaluating the electric and magnetic fields on the surface and the electric field inside the scatterer

$$\frac{\mathbf{M}^{s}(\mathbf{r})}{2}+\hat{\mathbf{n}}\times\eta_b\mathcal{L}_{\partial\Omega}^{(b)}[\mathbf{J}^{s}](\mathbf{r})-\hat{\mathbf{n}}\times\mathcal{K}_{\partial\Omega}^{(b)}[\mathbf{M}^{s}](\mathbf{r})=-\hat{\mathbf{n}}\times\mathbf{E}^{\text{inc}}(\mathbf{r})\quad \mathbf{r}\in\partial\Omega\ , \tag{6.1}$$

$$-\frac{\mathbf{J}^{s}(\mathbf{r})}{2}+\hat{\mathbf{n}}\times\frac{1}{\eta_b}\mathcal{L}_{\partial\Omega}^{(b)}[\mathbf{M}^{s}](\mathbf{r})+\hat{\mathbf{n}}\times\mathcal{K}_{\partial\Omega}^{(b)}[\mathbf{J}^{s}](\mathbf{r})=-\hat{\mathbf{n}}\times\mathbf{H}^{\text{inc}}(\mathbf{r})\quad \mathbf{r}\in\partial\Omega\ , \tag{6.2}$$

$$\eta_b\mathcal{L}_{\partial\Omega}^{(b)}[\mathbf{J}^{s}](\mathbf{r})-\mathcal{K}_{\partial\Omega}^{(b)}[\mathbf{M}^{s}](\mathbf{r})=-\mathbf{E}^{\text{inc}}(\mathbf{r})\quad \mathbf{r}\in\Omega\ , \tag{6.3}$$

where

$$\mathcal{L}_{\partial\Omega}^{(l)}[\mathbf{F}](\mathbf{r})=-jk_l\int_{\partial\Omega}\mathbf{F}(\mathbf{r}')\frac{\exp(-jk_l|\mathbf{r}-\mathbf{r}'|)}{4\pi|\mathbf{r}-\mathbf{r}'|}d\mathbf{r}'+\frac{\nabla}{jk_l}\int_{\partial\Omega}(\nabla'\cdot\mathbf{F}(\mathbf{r}'))\frac{\exp(-jk_l|\mathbf{r}-\mathbf{r}'|)}{4\pi|\mathbf{r}-\mathbf{r}'|}d\mathbf{r}'$$
$$\mathcal{K}_{\partial\Omega}^{(l)}[\mathbf{F}](\mathbf{r})=-p.v.\int_{\partial\Omega}\mathbf{F}(\mathbf{r}')\times\nabla\frac{\exp(-jk_l|\mathbf{r}-\mathbf{r}'|)}{4\pi|\mathbf{r}-\mathbf{r}'|}d\mathbf{r}' \quad , \tag{6.4}$$

$$\mathcal{L}_{\Omega}^{(l)}[\mathbf{F}](\mathbf{r})=k_l^{\,2}\int_{\Omega}\mathbf{F}(\mathbf{r}')\frac{\exp(-jk_l|\mathbf{r}-\mathbf{r}'|)}{4\pi|\mathbf{r}-\mathbf{r}'|}d\mathbf{r}'+\nabla\int_{\Omega}(\nabla'\cdot\mathbf{F}(\mathbf{r}'))\frac{\exp(-jk_l|\mathbf{r}-\mathbf{r}'|)}{4\pi|\mathbf{r}-\mathbf{r}'|}d\mathbf{r}'$$
$$\mathcal{K}_{\Omega}^{(l)}[\mathbf{F}](\mathbf{r})=-\frac{jk_l}{\eta_l}\int_{\Omega}\mathbf{F}(\mathbf{r}')\times\nabla\frac{\exp(-jk_l|\mathbf{r}-\mathbf{r}'|)}{4\pi|\mathbf{r}-\mathbf{r}'|}d\mathbf{r}' \quad , \tag{6.5}$$

$k_l=\omega\sqrt{\varepsilon_l\mu_l}$ is the wavenumber, $\eta_l=\sqrt{\mu_l/\varepsilon_l}$ denotes the characteristic impedance of the medium with permittivity ε_l and permeability μ_l, $\mathcal{L}_{\partial\Omega}^{(l)}$ is the surface electric field integral operator, $\mathcal{K}_{\partial\Omega}^{(l)}$ is the surface magnetic field integral operator, $\mathcal{L}_{\Omega}^{(l)}$ is the volume electric field integral operator, $\mathcal{K}_{\Omega}^{(l)}$ is the volume magnetic field integral operator, and $p.v.$ indicates the principal value of the integral. In the 'interior' scenario, surface currents $-\mathbf{J}^s(\mathbf{r})$ and $-\mathbf{M}^s(\mathbf{r})$ on $\partial\Omega$ and volumetric polarization current $\mathbf{J}^v(\mathbf{r})=jk_{eff}\chi_D^{(eff)}(\mathbf{r})\mathbf{E}(\mathbf{r})/\eta_{eff}$ in Ω radiate in a homogenous background medium with permittivity ε_{eff} and permeability μ_b, where $\chi_D^{(eff)}(\mathbf{r})=\left(\varepsilon(\mathbf{r})/\varepsilon_{eff}-1/\varepsilon(\mathbf{r})\right)$ is the electric contrast. These currents generate $\mathbf{E}(\mathbf{r})$ and $\mathbf{H}(\mathbf{r})$ inside Ω and zero fields elsewhere. The interior EFIE and MFIE and the volume integral equation can be derived by evaluating the fields generated on the surface of the object and inside the object as

$$-\frac{\mathbf{M}^s(\mathbf{r})}{2}+\hat{\mathbf{n}}\times\eta_{eff}\mathcal{L}_{\partial\Omega}^{(eff)}[\mathbf{J}^s](\mathbf{r})-\hat{\mathbf{n}}\times\mathcal{K}_{\partial\Omega}^{(eff)}[\mathbf{M}^s](\mathbf{r})-\hat{\mathbf{n}}\times\mathcal{L}_{\Omega}^{(eff)}[\frac{\eta_{eff}}{jk_{eff}}\mathbf{J}^v](\mathbf{r})=0 \quad \mathbf{r}\in\partial\Omega \ , \tag{6.6}$$

$$\frac{\mathbf{J}^s(\mathbf{r})}{2}+\hat{\mathbf{n}}\times\frac{1}{\eta_{eff}}\mathcal{L}_{\partial\Omega}^{(eff)}[\mathbf{M}^s](\mathbf{r})+\hat{\mathbf{n}}\times\mathcal{K}_{\partial\Omega}^{(eff)}[\mathbf{J}^s](\mathbf{r})-\hat{\mathbf{n}}\times\mathcal{K}_{\Omega}^{(eff)}[\frac{\eta_{eff}}{jk_{eff}}\mathbf{J}^v](\mathbf{r})=0 \quad \mathbf{r}\in\partial\Omega \ , \tag{6.7}$$

$$\mathbf{E}(\mathbf{r})+\eta_{eff}\mathcal{L}_{\partial\Omega}^{(eff)}[\mathbf{J}^s](\mathbf{r})-\mathcal{K}_{\partial\Omega}^{(eff)}[\mathbf{M}^s](\mathbf{r})-\mathcal{L}_{\Omega}^{(eff)}[\frac{\eta_{eff}}{jk_{eff}}\mathbf{J}^v](\mathbf{r})=0 \quad \mathbf{r}\in\Omega \ . \tag{6.8}$$

Combining (6.1)-(6.3) with (6.6)-(6.8) yields the following 3-D ICVSIE system of equations:

$$\begin{bmatrix} \frac{(\alpha_{ext}-\alpha_{int})}{2}\mathcal{I}-\hat{\mathbf{n}}\times(\alpha_{ext}\mathcal{K}_{\partial\Omega}^{(b)}+\alpha_{int}\mathcal{K}_{\partial\Omega}^{(eff)}) & \hat{\mathbf{n}}\times(\alpha_{ext}\eta_b\mathcal{L}_{\partial\Omega}^{(b)}+\alpha_{int}\eta_{eff}\mathcal{L}_{\partial\Omega}^{(eff)}) & -\hat{\mathbf{n}}\times\alpha_{int}\mathcal{L}_{\Omega}^{(eff)}\chi_E^{(eff)} \\ \hat{\mathbf{n}}\times(\frac{\beta_{ext}}{\eta_b}\mathcal{L}_{\partial\Omega}^{(b)}+\frac{\beta_{int}}{\eta_{eff}}\mathcal{L}_{\partial\Omega}^{(eff)}) & \frac{(\beta_{int}-\beta_{ext})}{2}\mathcal{I}+\hat{\mathbf{n}}\times(\beta_{ext}\mathcal{K}_{\partial\Omega}^{(b)}+\beta_{int}\mathcal{K}_{\partial\Omega}^{(eff)}) & -\hat{\mathbf{n}}\times\beta_{int}\mathcal{K}_{\Omega}^{(eff)}\chi_E^{(eff)} \\ -(\xi_{ext}\mathcal{K}_{\partial\Omega}^{(b)}+\xi_{int}\mathcal{K}_{\partial\Omega}^{(eff)}) & (\xi_{ext}\eta_b\mathcal{L}_{\partial\Omega}^{(b)}+\xi_{int}\eta_{eff}\mathcal{L}_{\partial\Omega}^{(eff)}) & \xi_{int}(\frac{\mathcal{I}}{\varepsilon}-\mathcal{L}_{\Omega}^{(eff)}\chi_D^{(eff)}) \end{bmatrix}. \quad (6.9)$$

$$\begin{bmatrix} \mathbf{M}^s \\ \mathbf{J}^s \\ \mathbf{D} \end{bmatrix}(\mathbf{r})=\begin{bmatrix} -\alpha_{ext}\hat{\mathbf{n}}\times\mathbf{E}^{inc} \\ -\beta_{ext}\hat{\mathbf{n}}\times\mathbf{H}^{inc} \\ -\xi_{ext}\mathbf{E}^{inc} \end{bmatrix}(\mathbf{r})$$

Eqn. is obtained by (i) adding α_{ext} times exterior EFIE (Eqn. (6.1)) to α_{int} times interior EFIE (Eqn. (6.6)), (ii) adding β_{ext} times exterior MFIE (Eqn. (6.2)) to β_{int} interior MFIE (Eqn. (6.7)), and (iii) adding ξ_{ext} times exterior volume integral equation (Eqn. (6.3)) to ξ_{int} interior volume integral (Eqn. (6.8)).

6.2.2 Discrete Formulation

To solve the 3-D ICVSIE system of equations, $\mathbf{\Omega}$ is discretized with a mesh of hexahedrons while $\partial\mathbf{\Omega}$ is discretized with a mesh of rectangles. Then, $\mathbf{J}^s(\mathbf{r})$, $\mathbf{M}^s(\mathbf{r})$, and $\mathbf{D}(\mathbf{r})$ are approximated as

$$\mathbf{J}^s(\mathbf{r})=\sum_{j=1}^{N_s} J_j\, R_j(\mathbf{r}) \quad (6.10)$$

$$\mathbf{M}^s(\mathbf{r})=\sum_{j=1}^{N_s} M_j\, R_j(\mathbf{r}) \quad (6.11)$$

$$\mathbf{D}(\mathbf{r})=\sum_{j=1}^{N_v} D_j\, Br_j(\mathbf{r}) \quad (6.12)$$

where $R_j(\mathbf{r})$ is a roofttop basis function [123], $Br_j(\mathbf{r})$ is a brick basis function [123], N_s is the number of edges on the boundary of the mesh, and N_v is the number of rectangles of the mesh. Then, we test the surface integral equations in Eqn. (6.9) with $R_i(\mathbf{r})$ basis functions and the volume integral equation with $Br_i(\mathbf{r})$. The testing yields

$$\begin{bmatrix} \alpha_{ext}\eta_b \mathbf{Z}^{(b)}_{\mathbf{J,J}} + \alpha_{\text{int}}\eta_{eff}\mathbf{Z}^{(eff)}_{\mathbf{J,J}} & \frac{(\alpha_{ext}-\alpha_{int})}{2}\mathbf{I} - (\alpha_{ext}\mathbf{Z}^{(b)}_{\mathbf{J,M}} + \alpha_{\text{int}}\mathbf{Z}^{(eff)}_{\mathbf{J,M}}) & -\alpha_{int}\mathbf{Z}^{(eff)}_{\mathbf{J,D}} \\ \frac{-\beta_{ext}+\beta_{int}}{2}\mathbf{I} + (\beta_{ext}\mathbf{Z}^{(b)}_{\mathbf{M,J}} + \beta_{int}\mathbf{Z}^{(eff)}_{\mathbf{M,J}}) & \frac{\beta_{ext}}{\eta_b}\mathbf{Z}^{(b)}_{\mathbf{M,M}} + \frac{\beta_{int}}{\eta_{eff}}\mathbf{Z}^{(eff)}_{\mathbf{M,M}} & -\beta_{int}\mathbf{Z}^{(eff)}_{\mathbf{M,D}} \\ \xi_{ext}\eta_b \mathbf{Z}^{(b)}_{\mathbf{D,J}} + \xi_{int}\eta_{eff}\mathbf{Z}^{(eff)}_{\mathbf{D,J}} & -(\xi_{ext}\mathbf{Z}^{(b)}_{\mathbf{D,M}} + \xi_{int}\mathbf{Z}^{(eff)}_{\mathbf{D,M}}) & -\xi_{int}\mathbf{Z}^{(eff)}_{\mathbf{D,D}} \end{bmatrix}, \tag{6.13}$$

$$\begin{bmatrix} \mathbf{J} \\ \mathbf{M} \\ \mathbf{D} \end{bmatrix} = \begin{bmatrix} \alpha_{ext}\mathbf{E}^{\mathbf{inc}} \\ \beta_{ext}\mathbf{H}^{\mathbf{inc}} \\ \xi_{ext}\mathbf{E}^{\mathbf{inc}}_{\mathbf{v}} \end{bmatrix}$$

where

$$(\mathbf{I})_{i,j} = \left\langle \mathrm{R}_{\mathrm{i}}(\mathbf{r}), \mathrm{R}_{\mathrm{j}}(\mathbf{r}) \right\rangle,$$

$$\left(\mathbf{Z}^{(l)}_{\mathbf{J,J}}\right)_{i,j} = -\left\langle \hat{\mathbf{n}} \times \mathrm{R}_{\mathrm{i}}(\mathbf{r}), \mathcal{L}^{(l)}_{\partial\Omega}[\mathrm{R}_{\mathrm{j}}(\mathbf{r}')](\mathbf{r}) \right\rangle,$$

$$\left(\mathbf{Z}^{(l)}_{\mathbf{J,M}}\right)_{i,j} = -\left\langle \hat{\mathbf{n}} \times \mathrm{R}_{\mathrm{i}}(\mathbf{r}), \mathcal{K}^{(l)}_{\partial\Omega}[\mathrm{R}_{\mathrm{j}}(\mathbf{r}')](\mathbf{r}) \right\rangle,$$

$$\left(\mathbf{Z}^{(l)}_{\mathbf{J,D}}\right)_{\mathrm{i,j}} = -\left\langle \hat{\mathbf{n}} \times \mathrm{R}_{\mathrm{i}}(\mathbf{r}), \mathcal{L}^{(l)}_{\Omega}[\frac{\chi(\mathbf{r}';\varepsilon_l)}{\varepsilon(\mathbf{r}')}\mathrm{Br}_{\mathrm{j}}(\mathbf{r}')](\mathbf{r}) \right\rangle,$$

$$\left(\mathbf{Z}^{(l)}_{\mathbf{M,J}}\right)_{i,j} = -\left\langle \hat{\mathbf{n}} \times \mathrm{R}_{\mathrm{i}}(\mathbf{r}), \mathcal{K}^{(l)}_{\partial\Omega}[\mathrm{R}_{\mathrm{j}}(\mathbf{r}')](\mathbf{r}) \right\rangle,$$

$$\left(\mathbf{Z}^{(l)}_{\mathbf{M,M}}\right)_{i,j} = -\left\langle \hat{\mathbf{n}} \times \mathrm{R}_{\mathrm{i}}(\mathbf{r}), \mathcal{L}^{(l)}_{\partial\Omega}[\mathrm{R}_{\mathrm{j}}(\mathbf{r}')](\mathbf{r}) \right\rangle,$$

$$\left(\mathbf{Z}^{(l)}_{\mathbf{M,D}}\right)_{\mathrm{i,j}} = -\left\langle \hat{\mathbf{n}} \times \mathrm{R}_{\mathrm{i}}(\mathbf{r}), \mathcal{K}^{(l)}_{\Omega}[\frac{\chi(\mathbf{r}';\varepsilon_l)}{\varepsilon(\mathbf{r}')}\mathrm{Br}_{\mathrm{j}}(\mathbf{r}')](\mathbf{r}) \right\rangle,$$

$$\left(\mathbf{Z}^{(l)}_{\mathbf{D,J}}\right)_{\mathrm{i,j}} = \left\langle \mathrm{Br}_{\mathrm{i}}(\mathbf{r}), \mathcal{L}^{(l)}_{\partial\Omega}[\mathrm{R}_{\mathrm{j}}(\mathbf{r}')](\mathbf{r}) \right\rangle,$$

$$\left(\mathbf{Z}^{(l)}_{\mathbf{D,M}}\right)_{\mathrm{i,j}} = \left\langle \mathrm{Br}_{i}(\mathbf{r}), \mathcal{K}^{(l)}_{\partial\Omega}[\hat{\mathbf{n}}_{\mathrm{j}} \times \mathrm{R}_{\mathrm{j}}(\mathbf{r}')](\mathbf{r}) \right\rangle,$$

$$\left(\mathbf{Z}^{(l)}_{\mathbf{D,D}}\right)_{\mathrm{i,j}} = -\left\langle \mathrm{Br}_{\mathrm{i}}(\mathbf{r}), \frac{\mathrm{Br}_{\mathrm{j}}(\mathbf{r})}{\varepsilon(\mathbf{r})} \right\rangle + \left\langle \mathrm{Br}_{\mathrm{i}}(\mathbf{r}), \mathcal{L}^{(l)}_{\Omega}[\frac{\chi(\mathbf{r}';\varepsilon_l)}{\varepsilon(\mathbf{r}')}\mathrm{Br}_{\mathrm{j}}(\mathbf{r}')](\mathbf{r}) \right\rangle,$$

$$\left(\mathbf{E}^{\mathbf{inc}}\right)_{\mathrm{i}} = \left\langle \mathrm{R}_{\mathrm{i}}(\mathbf{r}), \mathbf{E}^{\mathbf{inc}}(\mathbf{r}) \right\rangle,$$

$$\left(\mathbf{H}^{\mathbf{inc}}\right)_{\mathrm{i}} = \left\langle \mathrm{R}_{\mathrm{i}}(\mathbf{r}), \mathbf{H}^{\mathbf{inc}}(\mathbf{r}) \right\rangle,$$

$$\left(\mathbf{E}_{\mathbf{v}}^{\mathbf{inc}}\right)_{\mathrm{i}} = \left\langle \mathrm{Br}_{\mathrm{i}}(\mathbf{r}), \mathbf{E}^{\mathbf{inc}}(\mathbf{r}) \right\rangle ,$$

and

$$\left\langle \mathbf{A}(\mathbf{r}), \mathbf{B}(\mathbf{r}) \right\rangle = \int \mathbf{A}(\mathbf{r}) \cdot \mathbf{B}(\mathbf{r}) \, d\mathbf{r} .$$

The matrix is compressed leveraging fast convolutions via FFTs [124] and self-terms are calculated using the singularity-subtraction technique previously described in [121]. The performance of the ICVSIE is compared with that of the VIE (i.e. $(\mathcal{I}/\varepsilon - \mathcal{L}_{\mathbf{\Omega}}^{(b)} \chi_D^{(b)})\mathbf{D}(\mathbf{r}) = \mathbf{E}^{\mathbf{inc}}(\mathbf{r})$)

6.3 Results and Discussions

6.3.1 High-Contrast/Low-Frequency Layered Sphere

In the following section we consider scattering by dielectric four concentric layer spheres each with radius r, layer radii $r/4$, $r/2$, $3r/4$ and r and electric permittivity inner to outer of $\varepsilon_{\max}/4$, $\varepsilon_{\max}/2$, $3\varepsilon_{\max}/4$ and $\varepsilon_{\max}$. Each sphere resides in a free-space background medium with $\varepsilon_b = \varepsilon_0$ and $\mu_b = \mu_0$ and is illuminated by a time-harmonic $3\,kHz$ $\hat{\mathbf{x}}$-polarized plane-wave propagating along the $\hat{\mathbf{z}}$ direction. The ICVSIE is discretized with $\varepsilon_{eff} = \varepsilon_{\max}/4$.

Accuracy: Consider layered spheres with $\varepsilon_{\max} = \{10, 10^4, 10^7\}\varepsilon_0$, and $r = 1/(10\sqrt{\varepsilon_{\max}})$ m. Each sphere is approximated by a mesh consisting of $64 \times 64 \times 64$ square voxels each with dimensions $r/32 \times r/32 \times r/32$. The electric field are computed using the VIE, ICVSIE, and a Mie series solution. The magnitudes of the electric field components along lines crossing the center of the sphere are shown in fig. 6.2. There is good agreement between the analytical and both the VIE and ICVSIE solutions for the $\varepsilon_{\max} = \{10, 10^4\}\varepsilon_0$ cases. However, for the case where $\varepsilon_{\max} = 10^7 \varepsilon_0$ only the ICVSIE accurate. The ICVSIE is more accurate than the VIE for high permitivities.

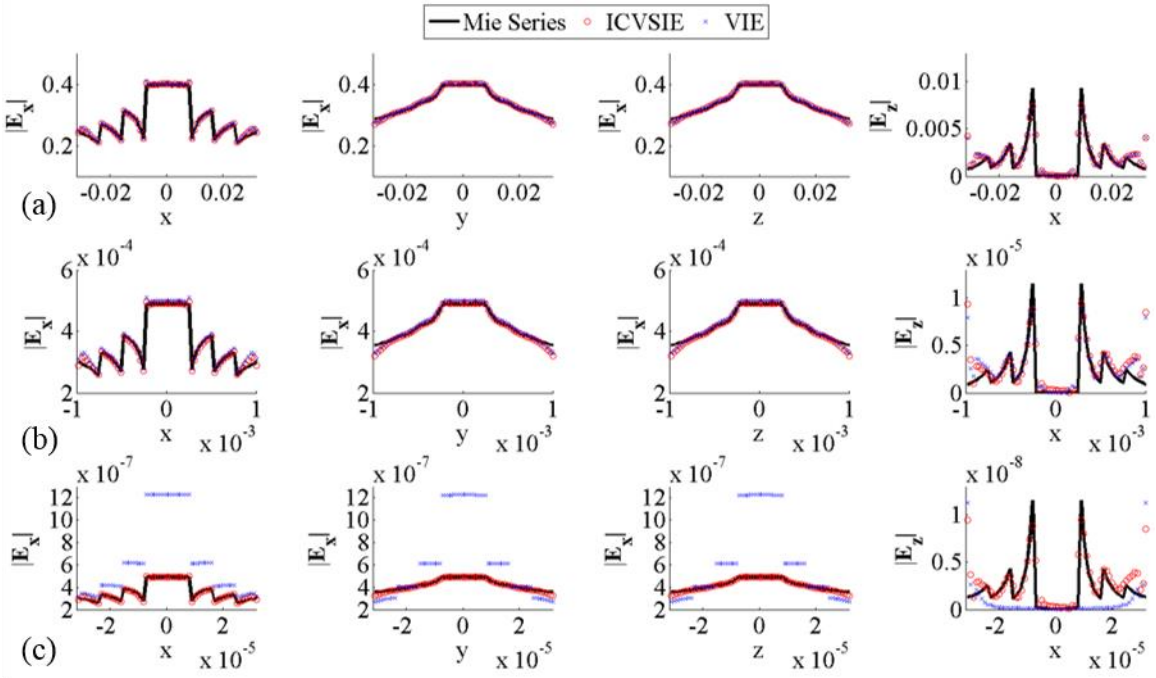

Figure 6.2 Electric field along lines crossing the center of the four layer sphere: (a) $\varepsilon_{\max} = 10\varepsilon_0$ (b) $\varepsilon_{\max} = 10^4\varepsilon_0$ (c) $\varepsilon_{\max} = 10^7\varepsilon_0$.

Condition Number: Consider layered spheres with $\varepsilon_{\max} = \{10, 10^2, ..., 10^7\}\varepsilon_0$, and $r = 1/(10\sqrt{\varepsilon_{\max}})$ m. Each sphere is approximated by a mesh consisting of $16\times16\times16$ square voxels each with dimensions $r/8 \times r/8 \times r/8$. The condition number of the matrix arising from the discretization of VIE and ICVSIE for each sphere are computed and shown in figure 6.3. The condition number of the ICVSIE is constant with respect to increasing permittivity, whereas the VIE condition number increases linearly with increasing permittivity. For electrically small spheres the ICVSIE is stable with respect to increasing permittivity. Thus making it suitable for analysis of TMS fields.

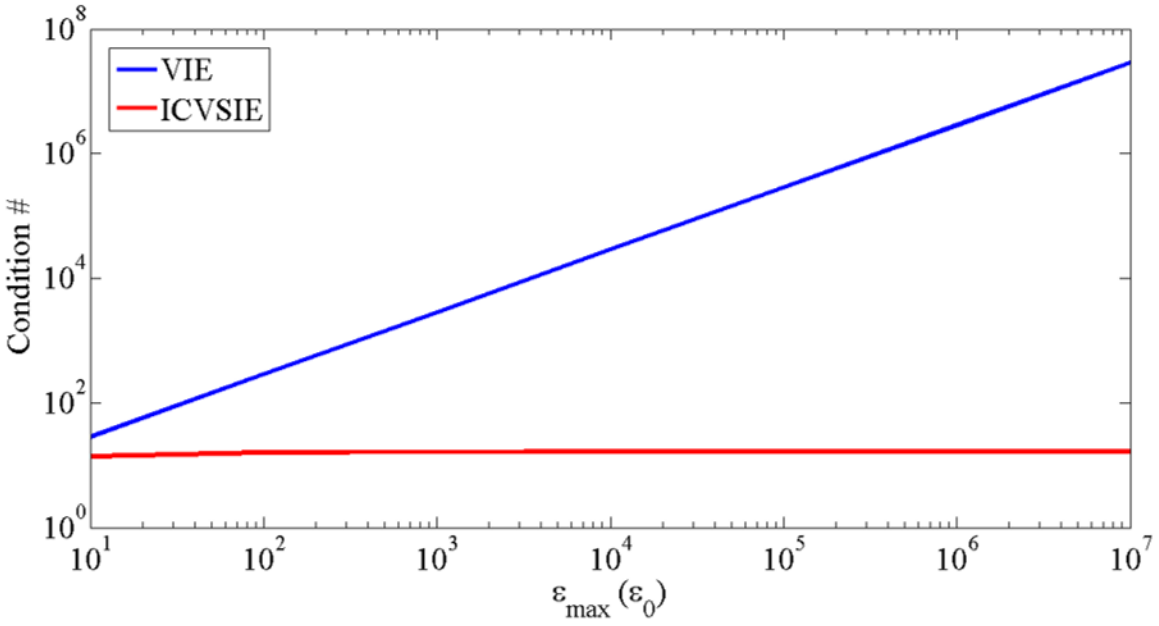

Figure 6.3 Condition number as a function of maximum electric permittivity.

6.3.2 MRI Derived Head Model

We approximate the head by a 'MRI-derived' conductivity head model as described in section 2.3.2. The head model has $128\times128\times62$ voxels with an edge length of 2.4 mm. First, the head model is excited by a Figure-8 coil consisting of two filamentary wire circular loops with radius of 3cm side by side. The coil is placed 1cm above the head as shown in Fig. 6.4 and is driven by a time-harmonic current with frequency of 3kHz and having a magnitude of $9.072\,k$A .

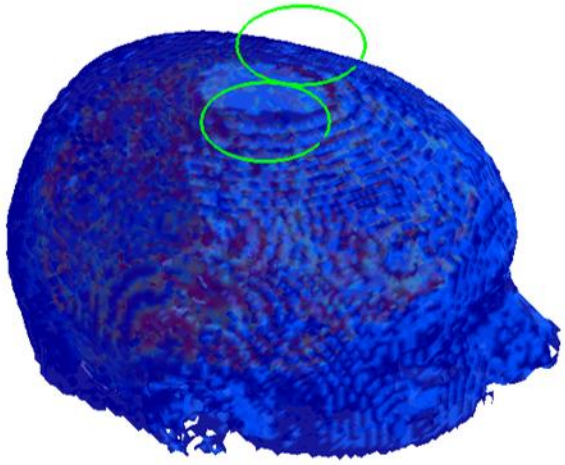

Figure 6.4 TMS setup

The electric field generated inside the MRI derived brain is determined by solving ICVSIE and VIE systems of equations using a Transpose Free Quasi-minimal Residual (TFQMR) method [122]. The TFQMR method is run till a residual error of 10^{-4} is reached or the method stagnates. The iterative convergence is shown in Fig. 6.5. For TMS scenarios the VIE system of equations is ill-conditioned and it did not converge. Contrastingly, the ICVSIE converged after 212 iterations. In conclusion, unlike the VIE, the ICVSIE can be used in conjunction with iterative solvers for determining fields generated during TMS.

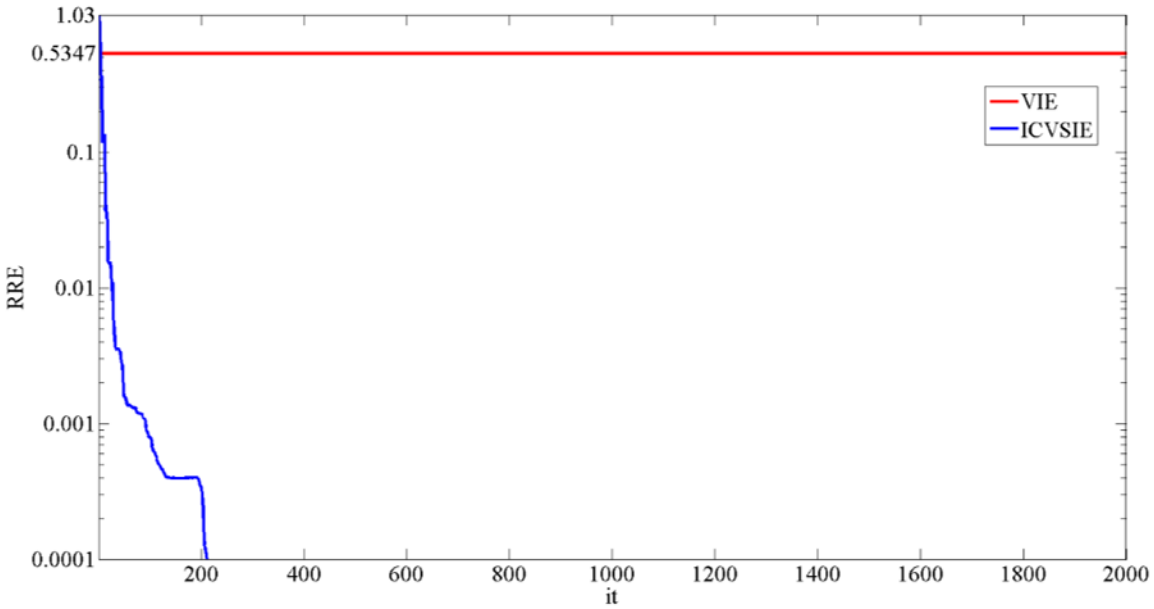

Figure 6.5 Relative Residual history for the VIE and ICVSIE

The total electric field computed using the ICVSIE and the incident field on selected planes are shown in Fig. 6.6. As expected the total field is a distorted version of the incident electric field.

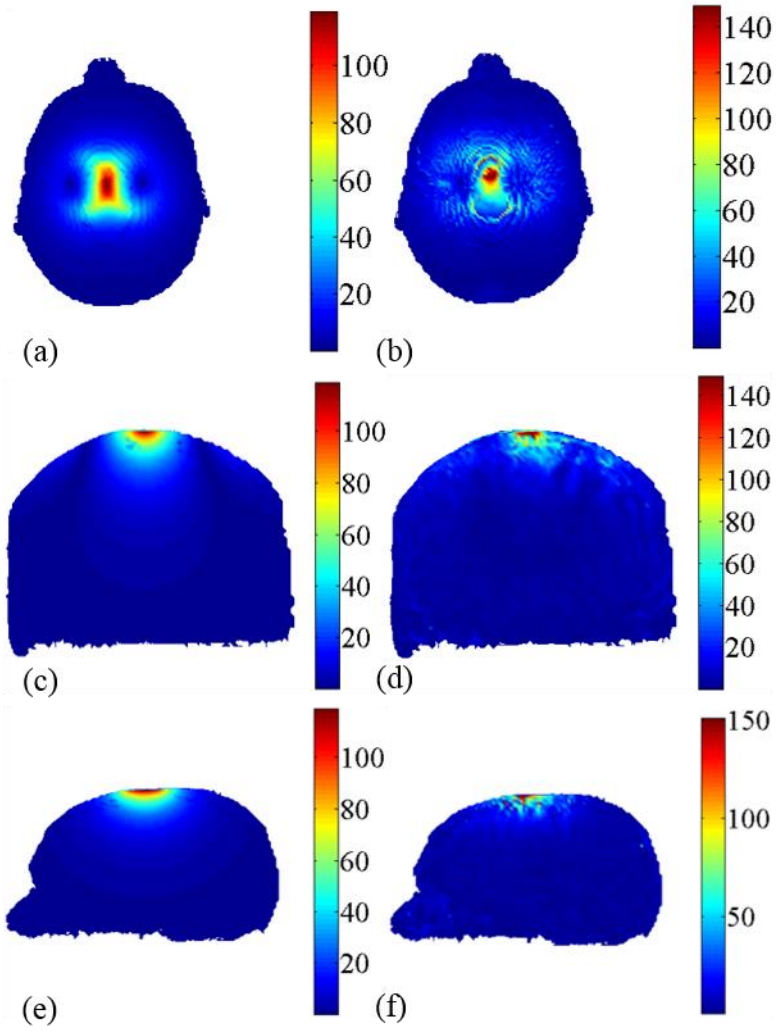

Figure 6.6 Electric field (V/m) generated during TMS scenario on various planes: (a) incident field on the scalp (b) total field on the scalp (c) incident field on a coronal plane crossing the center of the coil (d) total field on a coronal plane crossing the center of the coil (e) incident field on a sagittal plane crossing the center of the coil (f) total field on a sagittal plane crossing the center of the coil

Second, A BC-70 coil is placed by a (simulated) Medtronic MC-B70 Figure-8 coil (P/N 9790) [45] [Fig. 3.4] consisting of two spiral wings, each of which has 10 wire turns and inner/outer radii of $12\,\text{mm}/54\,\text{mm}$, and is driven by a time-harmonic current with frequency of 3kHz and having a magnitude of $9.072\,k\text{A}$. The left and right windings are bent by angles of 18.5° and 16°, respectively, and positioned $5\,\text{mm}$ away from one another (measured at the center of the coil). The coil is centered as shown in Fig. 6.7.

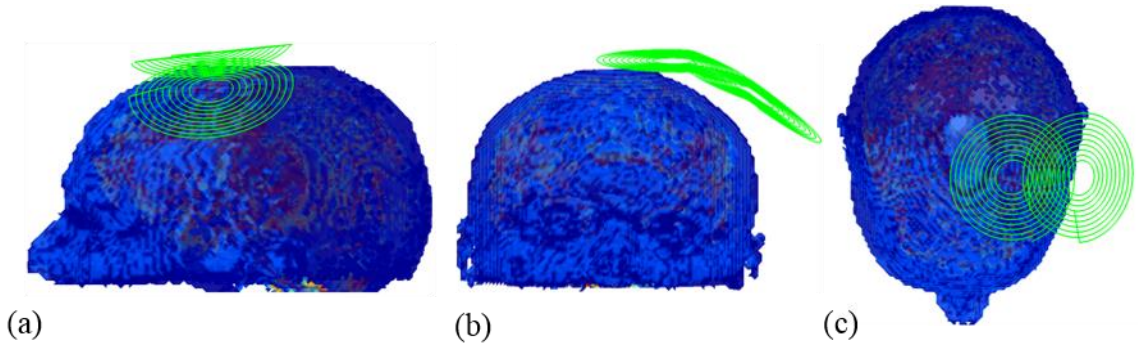

Figure 6.7 TMS setup: (a) side view (b) front view (c) top view

The electric field generated inside the MRI derived brain is determined by solving ICVSIE and VIE systems of equations using a Transpose Free Quasi-minimal Residual (TFQMR) method [122]. The TFQMR method is run till a residual error of 10^{-4} is reached or the method stagnates. The iterative convergence is shown in Fig. 6.8. For TMS scenarios the VIE system of equations is ill-conditioned and it did not converge. Contrastingly, the ICVSIE converged after 179 iterations. In conclusion, unlike the VIE, the ICVSIE can be used in conjunction with iterative solvers for determining fields generated during TMS.

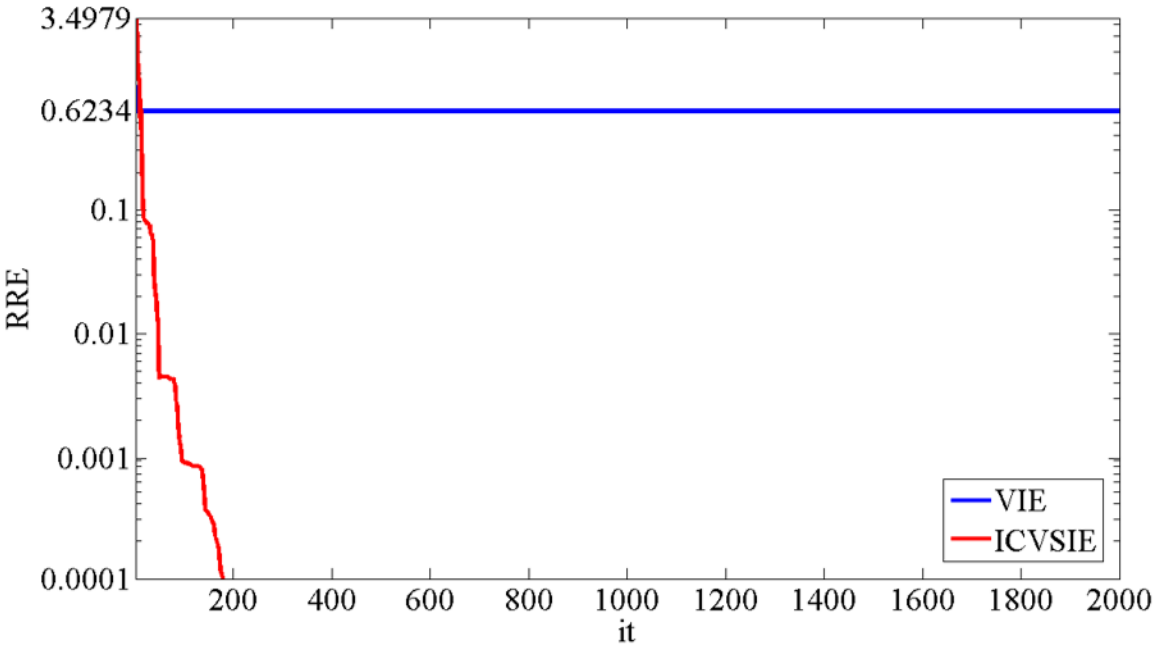

Figure 6.8 Relative Residual history for the VIE and ICVSIE

The electric field computed using the ICVSIE along selected planes are shown in Fig. 6.9. The overall shape of the field and magnitudes match those expected for this TMS scenario.

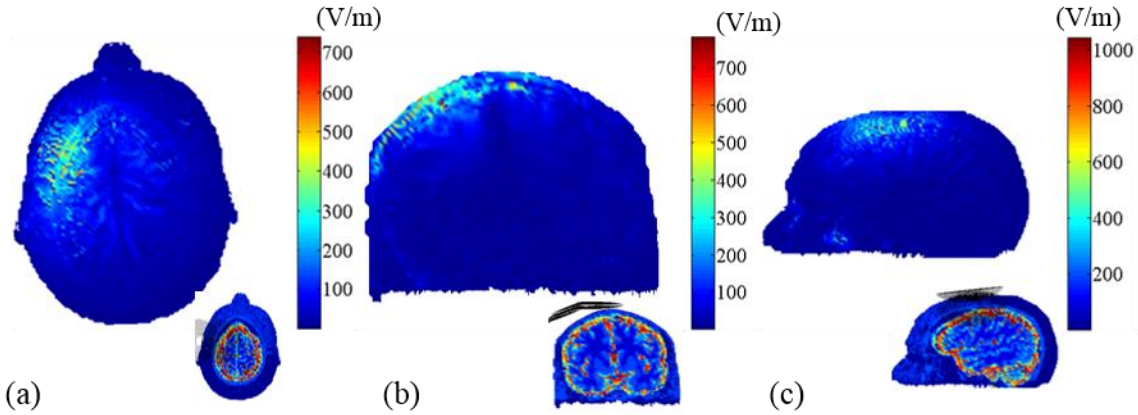

Figure 6.9 Electric field generated during TMS on various planes: (a) transverse plane (b) coronal plane (c) sagittal plane

6.4 Conclusions

We presented and computationally verified a 3D implementation of the ICVSIE. Unlike other integral equation approaches for analyzing electromagnetic fields generated inside heterogeneous high-contrast scatterers, our method does not suffer from high-contrast or low-frequency breakdown.

CHAPTER 7
Conclusions and Future Work

Advances in computation technology enable the use of computational/numerical techniques for the development of new technologies and scientific discovery. Thus far, high-fidelity numerical models have only been developed for use in a handful of research areas. In this research we have developed and applied new numerical techniques to improve Transcranial magnetic stimulation (TMS) systems.

7.1 Summary

This thesis presented several Electromagnetics (CEM) tools for the design of next generation Transcranial magnetic stimulation (TMS) systems. The contibutions of this thesis are the following:

TMS coil design: We developed a systematic, multi-objective Pareto genetic algorithm based technique for synthesizing multi-channel arrays that minimize the volume of the stimulated region required to reach a prescribed penetration depth. Numerical data shows that the arrays designed via the proposed technique are vastly superior to that of existing TMS coils. Furthermore, we devised a method to convert the multi-channel arrays into single-channel ones without materially deteriorating their performance.

Uncertainty Quantification of TMS: We have developed a framework that leverages a high dimensional model representation (HDMR) for statistically characterizing the region stimulated by TMS. First, we generate parameterized surrogate models for the electric field. Next, we use the surrogate models in lieu of the

electromagnetic simulator to obtain the statistics of the stimulated regions via Monte-Carlo. The framework was then used to analyze the uncertainty of the electric field generated during TMS treatments of depression.

Fast direct solver for TMS: By leveraging the multi-frontal approach, geometric bisection and compressibility using hierarchical matrices, we constructed a fast direct solver determining the electric fields generated during TMS using an FD method. After a single factorization step the solver is able to solve the FD system of equation in seconds, and thus, enabling its use in real-time TMS applications.

Internally Combined Volume Surface Integral Equation (ICVSIE): A novel ICVSIE approach for analyzing scattering by highly heterogenous objects was introduced. The ICVSIE can be used to analyse scattering from objects with arbitrarily large and negative permitivities (appendix A). It is also low-frequency stable enabling its use for analysis of TMS fields.

We have developed CEM tools, which enable neuroscientists to better predict the stimulated region during TMS, as well as, design TMS systems producing highly localized stimulation. This will broaden TMS' research and therapeutic appeal.

7.2 Future Work

The coil design methodologies and computational techniques introduced in this work vastly differ from the ones previously used for computer aided design and analysis of TMS. Correrspondingly, all of the techniques remain in their infancy and several ongoing efferts are being made to further advance them.

TMS coil design: The algorithm described in chapter 2 for synthesizing single-channel TMS coil arrays has been numerically shown to come up with designs that are vastily superior to currently used TMS coils. However, experimental validation of our results remains to be done. Currently, prototypes of the coils are being built and the magnetic fields they generate during operation are being measured using a technique described in [125].

Uncertainty Quantification of TMS: A framework for quantifying uncertatinty of the electric field generated during TMS resulting from uncertainty in the TMS procedure was developed in this work. The framework was applied to analyze the uncertainty of the electric field generated during TMS depression therapy. However, further refinements to the framework and experiments remain to be done. The framework needs to include uncertainty quantification of other parameters that are of interest to neuroscientists (e.g. the location/volume/depth of the stimulated region during TMS). Since the level of TMS intensity is often altered during the TMS procedure and it is not understood how this affects the electric field generated in underlying tissue, the framework is being used to study the effects of the level of TMS intensity on the TMS procedure. In the future, this technique could be hybridized with the one introduced in chapter 2 to come up with coil designs that exhibit optimal trade-offs between penetration depth, volume of excitation, and variance of the electric field as a function of uncertainty in the TMS procedure.

Fast direct solver for TMS: In chapter 4, a fast direct solver for the FD linear systems of equations, which after a single factorization step it's able to solve the linear system of equation in seconds, and thus, enabling its use in real-time applications was introduced. Future research will be oriented on the improvement of the code parallelization and on utilization of GPUs that could facilitate the computation of the electric fields in a fraction of a second.

New integral equation formulation for TMS: In chapters 5 and 6 and Appendix A, the Internally Combined Volume-Surface Integral Equation (ICVSIE) integral equation was presented and it was shown that the discretization of the ICVSIE yields matrices with condition numbers that are unaffected by the materials maximum permittivity, electric size, or sign of the pemittivity. Currently an implementation based on triangle and tetrahedral elements of the ICVSIE method for analysis of 3D structures is being developed.

7.3 Contributions

This research resulted in the following contributions:

Papers:

[1] Hernandez, L.; Hall, T.; Gomez, L.; Michielssen, E.; “A numerically optimized active shield for improved transcranial magnetic stimulation targeting.” Brain Stimulation, vol. 3, pp. 218-25, Oct. 2010.

[2] Gomez, L.; Cajko, F., Hernandez-Garcia, L.; Grbic, A.; and Michielssen, E. ; "Numerical Analysis and Design of Single-Source Multicoil TMS for Deep and Focused Brain Stimulation," Biomedical Engineering, IEEE Transactions on, vol. 60, pp. 2771-82, 2013.

[3] Gomez, L.; Yucel A.; Hernandez-Garcia L.; Taylor S.; Michielssen, E; “Uncertainty Quantification in Transcranial Magnetic Stimulation via High Dimensional Model Representation Technique.” Biomedical Engineering, IEEE Transactions on, (Accepted)

[4] Gomez, L.; Yucel A.; Michielssen, E.; “Low-Frequency Stable Internally Combined Volume-Surface Integral Equation for High-Contrast Scatterers.” Antennas and Wireless Propagation Letters (In review)

[5] Gomez, L.; Yucel A.; Michielssen, E.; “Volume-Surface Combined Field Integral Equation for Plasma Scatterers.” Antennas and Wireless Propagation Letters (In Review)

[6] Cajko, F.; Gomez, L.; Michielssen, E.; Martinsson, P.G.; Hernandez, L.; “A Simple Fast Finite-Difference Direct Solver for Real-Time Simulation of Transcranial Magnetic Stimulation” (In Preparation)

Conference Papers:

[1] Gomez, L.; Hernandez, L.; Grbic, A.; Michielssen, E.; , "A simulation of focal brain stimulation using metamaterial lenses," Antennas and Propagation Society International Symposium (APSURSI), July 2010

[2] Cajko, F.; Michielssen, E.; Gomez, L.; Martinsson, P.G.; Hernandez, L.; , " A Fast Direct Solver for Transcranial Magnetic Stimulation Analysis," Antennas and Propagation Society International Symposium (APSURSI), July 2010

[3] Gomez, L.; Hernandez, L.; Grbic, A.; Michielssen, E.; , "Focused multi-coil transcranial magnetic stimulation," Antennas and Propagation Society International Symposium (APSURSI), July 2011

[4] Cajko, F.; Michielssen, E.; Gomez, L.; Martinsson, P.G.; Hernandez, L.; , "A fast direct solver for TMS analysis and design in 3D," Antennas and Propagation Society International Symposium (APSURSI), July 2011

[5] Gomez, L.; Hernandez, L.; Grbic, A.; Michielssen, E.; , " Single-Source Multi-Coil Transcranial Magnetic Stimulators for Deep and Focused Stimulation of the Human Brain," Antennas and Propagation Society International Symposium (APSURSI), July 2013

[6] Gomez, L.; Michielssen, E.; , " A Well-Conditioned Volume-Surface Field Integral Equation (VSCFIE) for Inhomogeneous Cylindrical Scatterers with High-Electrical Contrasts," Antennas and Propagation Society International Symposium (APSURSI), July 2013

[7] Gomez, L.; Yucel, A. C.; Hernandez, L.; Michielssen, E.; , " Uncertainty Quantification in Transcranial Magnetic Stimulation," Antennas and Propagation Society International Symposium (APSURSI), July 2013

[8] Gomez, L.; Yucel, A. C.; Michielssen, E.; , " A Well-Conditioned Volume-Surface Combined Field Integral Equation (VSCFIE) for Inhomogeneous Scatterers with Negative Permittivities," Antennas and Propagation Society International Symposium (APSURSI), July 2014

[9] Yucel, A. C.; Gomez, L.; Liu, Y.; Bagci, H.; Michielssen, E.; , " A FMM-FFT Accelerated Hybrid Volume Surface Integral Equation Solver for Electromagnetic Analysis of Re-Entry Space Vehicles," Antennas and Propagation Society International Symposium (APSURSI), July 2014

[10] Gomez, L.; Yucel, A. C.; Hernandez, L.; Taylor, S.; Michielssen, E.; , " Sensitivity of TMS-Induced Electric Fields to the Uncertainty in Coil Placement and Brain Anatomy," Antennas and Propagation Society International Symposium (APSURSI), July 2014

APPENDIX A
Internally Combined Volume-Surface Integral Equation for Plasma Scatterers

A.1 Introduction

Plasmas exhibit electromagnetic (EM) properties that lend themselves to applications ranging from microelectronic device manufacturing to lighting and military stealth systems. Plasmas encountered in many real-world applications are highly heterogeneous and have negative permittivity [126, 127]. To facilitate the development of new technologies that leverage plasmas, fast and accurate EM solvers are called for. Unfortunately, the application of standard differential and volume integral equation (VIE) techniques to the electromagnetic analysis of media with negative permittivities results in ill-conditioned systems of equations that converge slowly [128]. Here we propose the use of an Internally combined volume-surface integral equation (ICVSIE) technique to alleviate this problem [129, 130].

Previously, a ray tracing solver was used to analyze radiation from antennas on plasma-engulfed re-entry vehicles [126, 127]. Although this solver was shown to be effective for analyzing scattering by plasmas with interfaces between positive and negative permittivity media, it does not allow modeling of plasmas with rapid spatial permittivity variations, thereby restricting its usefulness to the analysis of non-turbulent plasmas.

Recently, it was shown that the application of surface combined field integral equations (CFIEs) to the analysis of scattering by homogenous negative permittivity media residing in a positive permittivity background medium results in well-conditioned systems of equations [131]. Unfortunately, surface CFIEs are not suited for analyzing EM

scattering by highly heterogeneous media. While VIEs are better fit for this task, they are not effective when used to analyze scattering from objects containing interfaces between positive and negative permittivity media [132].

Here an ICVSIE approach is proposed for analyzing scattering by highly heterogeneous negative permittivity media. In the ICVSIE, regions with negative permittivities are wrapped into equivalent electric and magnetic surface currents, and surface equivalence principles are invoked to artificially change the sign of the permittivity of the "background medium" in which the volume polarization currents of the negative permittivity medium radiate. Next, the surface and volume currents are computed by solving a VSIE system composed of coupled surface CFIEs and new VIEs. The new VIEs are constructed by adding contributions due to the surface currents exterior to the scatterer and propagating in the "background medium". The proposed scheme leverages a Muller-CFIE [116], which is well-conditioned when applied to homogenous negative permittivity media and it is applied to the analysis of time-harmonic 2-D TE_z scattering phenomena. That said, its extension to 3-D is straightforward.

It's worthwhile to note here that standard VSIE schemes are well suited for analyizing scattering by negative permitivity media. However, VSIEs suffer from a low-frequency (LF) breakdown: when the mesh that discretizes the scatterer contains elements with dimensions that are much smaller than the wavelength, discretization of the VSIE again results in ill-conditioned systems of equations. Contrastingly, the ICVSIE does not suffer from a LF breakdown and our results show that it outperforms a Muller-VSIE for analyzing negative permitivity media. (Note: throughout this Letter, a time dependence $e^{j\omega t}$ is assumed and suppressed, where $\omega=2\pi f$, t denotes time, and f is the frequency of analysis)

A.2 Formulation

Details of the derivation of VSIEs, and the ICVSIE and definitions for the notation are included in section 5.2.1. The general ICVSIE system of equations is the following:

$$\begin{bmatrix} \frac{(\alpha_{ext}-\alpha_{int})}{2}\mathcal{I}-\hat{\mathbf{n}}\times(\alpha_{ext}\mathcal{K}_{\partial\Omega}^{(b)}+\alpha_{int}\mathcal{K}_{\partial\Omega}^{(eff)}) & \hat{\mathbf{n}}\times(\alpha_{ext}\eta_b\mathcal{L}_{\partial\Omega}^{(b)}+\alpha_{int}\eta_{eff}\mathcal{L}_{\partial\Omega}^{(eff)}) & -\hat{\mathbf{n}}\times\alpha_{int}\mathcal{L}_{\Omega}^{(eff)}\chi_E^{(eff)} \\ \hat{\mathbf{n}}\times(\frac{\beta_{ext}}{\eta_b}\mathcal{L}_{\partial\Omega}^{(b)}+\frac{\beta_{int}}{\eta_{eff}}\mathcal{L}_{\partial\Omega}^{(eff)}) & \frac{(\beta_{int}-\beta_{ext})}{2}\mathcal{I}+\hat{\mathbf{n}}\times(\beta_{ext}\mathcal{K}_{\partial\Omega}^{(b)}+\beta_{int}\mathcal{K}_{\partial\Omega}^{(eff)}) & -\hat{\mathbf{n}}\times\beta_{int}\mathcal{K}_{\Omega}^{(eff)}\chi_E^{(eff)} \\ -(\xi_{ext}\mathcal{K}_{\partial\Omega}^{(b)}+\xi_{int}\mathcal{K}_{\partial\Omega}^{(eff)}) & (\xi_{ext}\eta_b\mathcal{L}_{\partial\Omega}^{(b)}+\xi_{int}\eta_{eff}\mathcal{L}_{\partial\Omega}^{(eff)}) & \xi_{int}(\frac{\mathcal{I}}{\varepsilon}-\mathcal{L}_{\Omega}^{(eff)}\chi_D^{(eff)}) \end{bmatrix} \begin{bmatrix} \mathbf{M}^S \\ \mathbf{J}^S \\ \mathbf{D} \end{bmatrix}(\boldsymbol{\rho})=\begin{bmatrix} -\alpha_{ext}\hat{\mathbf{n}}\times\mathbf{E}^{\text{inc}} \\ -\beta_{ext}\hat{\mathbf{n}}\times\mathbf{H}^{\text{inc}} \\ -\xi_{ext}\mathbf{E}^{\text{inc}} \end{bmatrix}(\boldsymbol{\rho}) \quad \text{, (A.1)}$$

where $\alpha_{int}=\varepsilon_{eff}$, $\beta_{int}=\mu_b$, $\alpha_{ext}=-\varepsilon_b$, $\beta_{ext}=-\mu_b$, $\xi_{int}=\varepsilon_{eff}$ and $\xi_{ext}=-\varepsilon_b$. Here ε_{eff} is chosen to match the sign of the permittivity of the scatterer. All of the ICVSIE results are compared with results obtained via a VIE and a Muller VSIE-D (i.e. (A.1) with $\alpha_{int}=\varepsilon_{eff}$, $\beta_{int}=\mu_b$, $\alpha_{ext}=-\varepsilon_b$, $\beta_{ext}=-\mu_b$, $\xi_{int}=\varepsilon_{eff}$ and $\xi_{ext}=0$).

To solve the ICVSIE, VIE and the Muller VSIE-D, Ω is approximated with a mesh of triangles. The surface electric and magnetic currents $\mathbf{J}^S(\boldsymbol{\rho})$ and $\mathbf{M}^S(\boldsymbol{\rho})$, and the electric flux $\mathbf{D}(\boldsymbol{\rho})$ are approximated using triangle $t(\boldsymbol{\rho})$, $\hat{\mathbf{n}}\times t(\boldsymbol{\rho})$, and Rao-Wilton-Glisson $RWG(\boldsymbol{\rho})$ basis functions, respectively. The solutions are obtained using a transpose-free quasi-minimal residual (TFQMR) iterative solver. Matrix-vector multiplications at each iteration of TFQMR are accelerated via the adaptive integral method (AIM) [133].

A.3 Results and Discussions

This section presents numerical results that demonstrate the effectiveness of the proposed ICVSIE when analyzing scattering from heterogeneous cylinders with negative permittivity that reside in free-space with permittivity $\varepsilon_b=\varepsilon_0$ and permeability $\mu_b=\mu_0$. In all examples considered, a circular cylinder with diameter d is illuminated by a TE_z plane-wave propagating along the $+\hat{\mathbf{x}}$ direction. Unless noted otherwise, the cylinder consists of four homogenous concentric layers with diameters $d/4$, $d/2$, $3d/4$, and d,

and permittivities $(-1+i10^{-5})\varepsilon_0$, $(-2+i10^{-5})\varepsilon_0$, $(-4+i10^{-5})\varepsilon_0$, and $(-3+i10^{-5})\varepsilon_0$, respectively. The quantities $\mathbf{J}^s$, $\mathbf{M}^s$, and $\mathbf{D}$ are obtained by iteratively solving the ICVSIE and the Muller VSIE-D with $\epsilon_{eff} = (-2+i10^{-5})\varepsilon_0$, as well as the VIE. L^2 error norms of the obtained quantities are computed using the Bessel series solution as a reference.

First, the accuracy and convergence of the ICVSIE, Muller VSIE-D and VIE solutions are investigated for increasing mesh densities. For this purpose, the cylinder with $d = \lambda_0 / 2$ is discretized using five uniform meshes with N_t = 310, 1240, 4960, 19840, and 79360 triangles corresponding to maximum edge lengths of $0.03\lambda_0$, $0.015\lambda_0$, $0.0075\lambda_0$, and $0.00375\lambda_0$, and $0.001875\lambda_0$, respectively. The L^2 norm errors of $\mathbf{J}^s$, $\mathbf{M}^s$, and $\mathbf{D}$ obtained by the proposed ICVSIE formulation are listed in Table A.1. As expected, all L^2 error norms decrease with increasing mesh density. The number of iterations required for the relative residual error (RRE) of the ICVSIE, Muller VSIE-D and VIE solutions to reach to 10^{-3} and 10^{-8} are tabulated and shown in Table A.2 and Fig. A.1 respectively. As the mesh density changes from low to high, the number of iterations required to reach an RRE of 10^{-3} changes from 33 to 48 and from 60 to 276 for the ICVSIE and the Muller VSIE-D, respectively. For meshes comprising more than 4960 triangles, the iterative solution of the VIE failed to converge to an RRE of 10^{-3} in 10,000 iterations. Furthermore, the number of iterations increases with N_t for the Muller VSIE-D and VIE systems' solutions. On the other hand, while N_t increases, the number of iterations for the ICVSIE changes only negligibly.

N_t / Quantity	310	1240	4960	19840	79360
$\mathbf{M}^s$	0.0877	0. 0449	0. 0230	0. 0125	0.0081
$\mathbf{J}^s$	0.0526	0. 0268	0. 0133	0. 0066	0.0044
$\mathbf{D}$	0.1251	0.0613	0.0309	0. 0169	0.0111

Table A.1 L^2 Norm errors of quantities obtained by ICVSIE system

N_t / System	310	1240	4960	19840	79360
ICVSIE	33	38	39	42	48
Muller VSIE-D	60	86	111	169	276
VIE	250	884	5468	>10,000	>10,000

Table A.2 Number of iterations required for RRE of systems' solution to reach to 10^{-3} while the mesh density changes

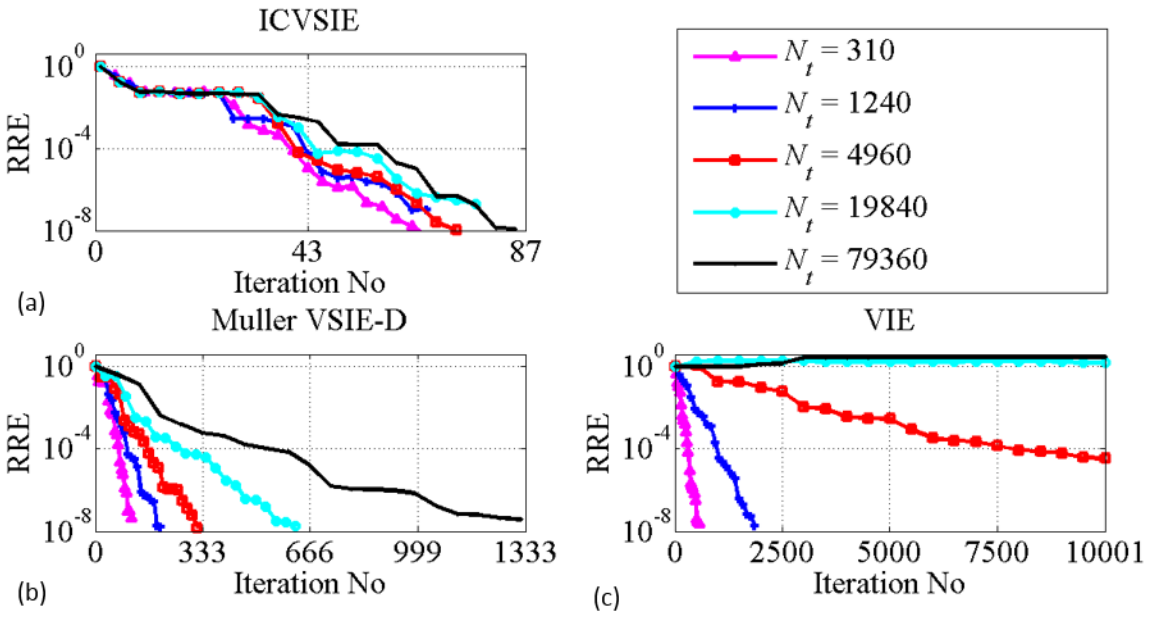

Figure A.1 Analysis with different mesh densities. Number of iterations versus RREs of (a) ICVSIE, (b) Muller VSIE-D, and (c) VIE systems' solutions to reach to 10^{-8}.

Next, the convergence of the ICVSIE, Muller VSIE-D and VIE solutions are investigated for increasing scatterer size. To this end, the diameter of the cylinder is increased from $d = \lambda_0 / 4$ to $d = 4\lambda_0$ by a factor of 2 for a total of five times. Each cylinder is discretized such that the maximum edge length is around $0.06\lambda_0$. The resulting five meshes consist of N_t = 310 ($d = \lambda_0 / 4$), 1240, 4960, 19840, and 79360 ($d = 4\lambda_0$) triangles. The number of iterations required for the RRE of the ICVSIE, Muller VSIE-D and VIE solutions to reach to 10^{-3} and 10^{-8} are tabulated and shown in Table A.3 and Fig. A.2, respectively. As the cylinder diameter changes from $\lambda_0 / 4$ to $4\lambda_0$, the number of iterations required to reach an RRE of 10^{-3} changes from 22 to 389 and from 51 to 1355 for the ICVSIE, Muller VSIE-D, respectively. For cylinders with diameters larger than λ_0, the iterative solution of the VIE system failed to converge to an RRE of 10^{-3} after 10,000 iterations. As the diameter of the cylinder increases, the number of iteration increases for both the ICVSIE and Muller VSIE-D systems' solutions, yet the number of iterations

required to reach to RRE of 10^{-8} for the solution of ICVSIE system is five times less than that for the solution of Muller VSIE-D system.

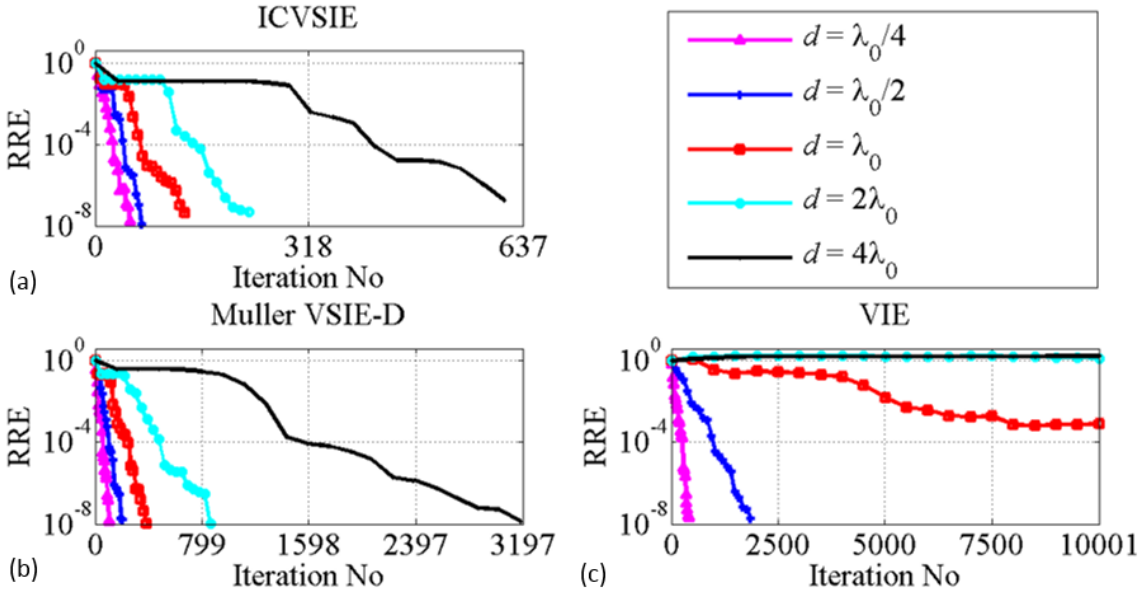

Figure A.2 Analysis with different cylinder diameters. Number of iterations versus RREs of (a) ICVSIE, (b) Muller VSIE-D, and (c) VIE systems' solutions.

Diameter / System	$\lambda_0/4$	$\lambda_0/2$	λ_0	$2\lambda_0$	$4\lambda_0$
ICVSIE	22	39	59	120	389
Muller VSIE-D	51	86	158	424	1355
VIE	186	884	7727	>10,000	>10,000

Table A.3 Number of iterations required for RRE of systems' solution to reach to 10^{-3} while the diameter of cylinder changes

Moreover, the bistatic radar cross sections (RCSs) of cylinders obtained by iteratively solving the ICVSIE, Muller VSIE-D and the VIE systems and compared with the exact ones computed by the Bessel series solution [Fig. A.3]; the numerical results are in good agreement with the analytical solution. Note that RCSs obtained by VIE scheme for the cylinders with diameters larger than λ_0 were not included in Fig. A.4(d) and (e) as the solution of VIE system failed to converge to RRE of 10^{-3} for those cylinders.

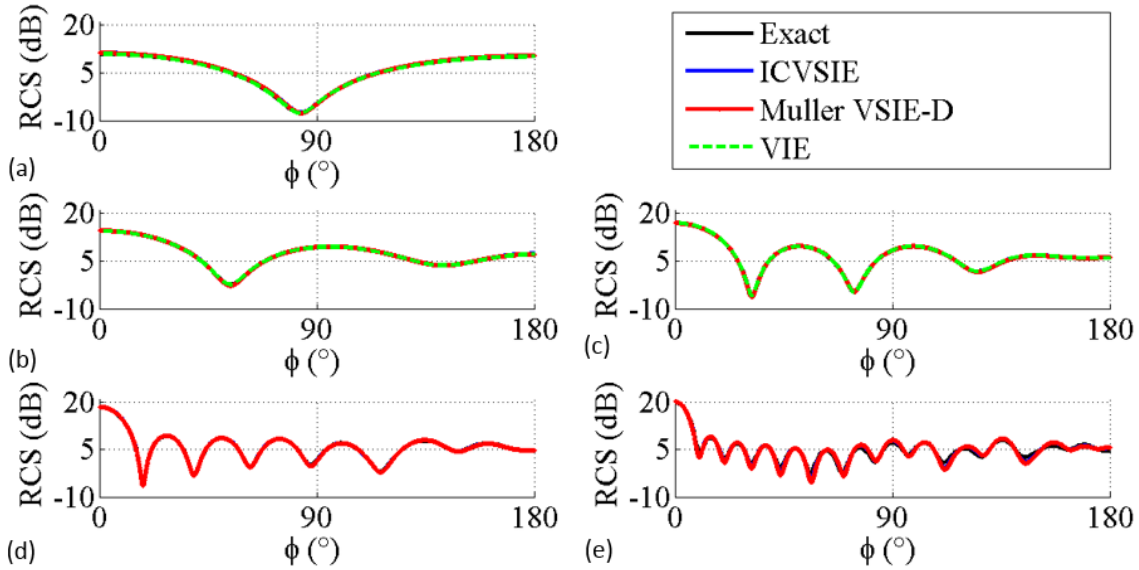

Figure A.3 Analysis with different cylinder diameters. The bistatic RCS of the cylinder with (a) $d=\lambda_0/4$, (b) $d=\lambda_0/2$, (c) $d=\lambda_0$, (d) $d=2\lambda_0$, and (e) $d=4\lambda_0$ obtained by Bessel series (Exact) solution, ICVSIE, Muller VSIE-D, and VIE systems' solutions.

Finally, the convergence of the iterative solutions of the ICVSIE, Muller VSIE-D and VIE solutions is examined as the number of cylinder layers is increased from two to sixteen by a factor of two for a total of four times. The total cylinder diameter is kept constant at $d=\lambda_0/2$. Each cylinder consists of N_{layer} layers with thickness d/N_{layer} and is meshed such that the maximum edge length and total number of triangles are $0.0075\lambda_0$ and 18,240, respectively. For each cylinder, the permittivities of the layers from innermost to outermost are $(-1+10^{-5}i)\varepsilon_0$ (innermost layer),…,$(-N_{\text{layer}}+10^{-5}i)\varepsilon_0$ (outermost layer). The number of iterations required for the RRE of the ICVSIE, Muller VISE-D and VIE solutions to reach to 10^{-3} and 10^{-8} are tabulated and shown in Table A.4 and Fig. A.4 respectively. As the number of layers increases, the number of iterations required to reach an RRE of 10^{-3} changes from 35 to 72 and from 35 to 885 for the ICVSIE and Muller-VSIE-D, respectively. The VIE solution failed to converge to an RRE of 10^{-3} in 10,000 iterations for cylinders with two to eight layers and it converges after 9,748 for cylinders with sixteen layers. As the number of layers increases, the number of iterations increases for both the ICVSIE and Muller VSIE-D. That said, the number of iterations required for the solution of ICVSIE system is smaller than that for solving the Muller VSIE-D.

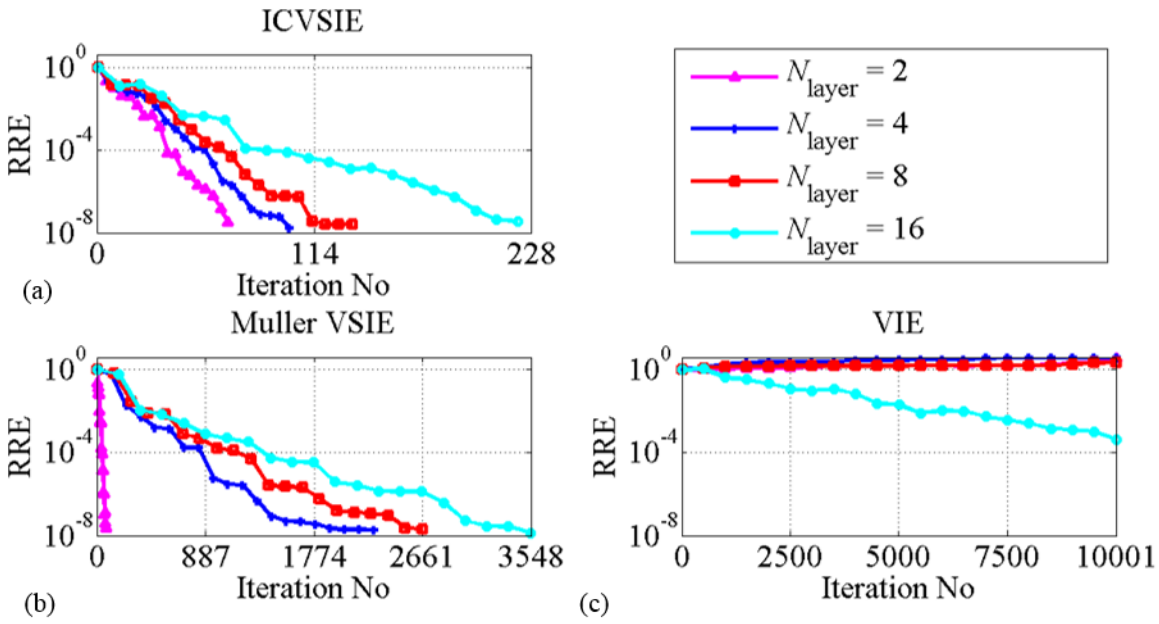

Figure A.4 Analysis with different numbers of layers. Number of iterations versus RREs of (a) ICVSIE, (b) Muller VSIE-D, and (c) VIE systems' solutions.

Number of layers / System	2	4	8	16
ICVSIE	35	42	52	72
Muller VSIE-D	35	628	687	885
VIE	>>10,000	>>10,000	>>10,000	99,748

Table A.4 Number of iterations required for RRE of systems' solution to reach to 10^{-3} while the number of layers changes

A.4 Conclusions

A well-conditioned ICVSIE formulation for analyzing scattering from highly-heterogeneous and negative permittivity plasmas was proposed. The numerical results showed the accuracy and rapid convergence of the proposed ICVSIE scheme.

REFERENCES

[1] B. J. Roth, "Mechanisms for electrical stimulation of excitable tissue," *Critical reviews in biomedical engineering,* vol. 22, p. 253, 1994.

[2] P. J. Maccabee, V. E. Amassian, L. P. Eberle, and R. Q. Cracco, "Magnetic coil stimulation of straight and bent amphibian and mammalian peripheral nerve in vitro: locus of excitation," *The Journal of Physiology,* vol. 460, pp. 201-219, January 1, 1993 1993.

[3] S. Ueno, T. Tashiro, and K. Harada, "Localized stimulation of neural tissues in the brain by means of a paired configuration of time-varying magnetic fields," *Journal of Applied Physics,* vol. 64, pp. 5862-5864, 1988.

[4] L. G. Cohen, B. J. Roth, J. Nilsson, N. Dang, M. Panizza, S. Bandinelli, *et al.*, "Effects of coil design on delivery of focal magnetic stimulation. Technical considerations," *Electroencephalography and Clinical Neurophysiology,* vol. 75, pp. 350-357, 4// 1990.

[5] J. A. Nyenhuis, G. A. Mouchawar, J. D. Bourland, and L. A. Geddes, "Energy considerations in the magnetic (eddy-current) stimulation of tissues," *Magnetics, IEEE Transactions on,* vol. 27, pp. 680-687, 1991.

[6] B. J. Roth, J. M. Saypol, M. Hallett, and L. G. Cohen, "A theoretical calculation of the electric field induced in the cortex during magnetic stimulation," *Electroencephalography and Clinical Neurophysiology/Evoked Potentials Section,* vol. 81, pp. 47-56, 2// 1991.

[7] S. Rossi, M. Hallett, P. M. Rossini, and A. Pascual-Leone, "Safety, ethical considerations, and application guidelines for the use of transcranial magnetic stimulation in clinical practice and research," *Clinical Neurophysiology,* vol. 120, pp. 2008-2039, 2009.

[8] Y. Roth, A. Zangen, and M. Hallett, "A Coil Design for Transcranial Magnetic Stimulation of Deep Brain Regions," *Journal of Clinical Neurophysiology,* vol. 19, pp. 361-370, 2002.

[9] R. Chunye, P. P. Tarjan, and D. B. Popovic, "A novel electric design for electromagnetic stimulation-the Slinky coil," *Biomedical Engineering, IEEE Transactions on,* vol. 42, pp. 918-925, 1995.

[10] H. Kai-Hsiung and D. M. Durand, "A 3-D differential coil design for localized magnetic stimulation," *Biomedical Engineering, IEEE Transactions on,* vol. 48, pp. 1162-1168, 2001.

[11] K. R. Davey and M. Riehl, "Suppressing the surface field during transcranial magnetic stimulation," *Biomedical Engineering, IEEE Transactions on,* vol. 53, pp. 190-194, 2006.
[12] K. Dong-Hun, G. E. Georghiou, and C. Won, "Improved field localization in transcranial magnetic stimulation of the brain with the utilization of a conductive shield plate in the stimulator," *Biomedical Engineering, IEEE Transactions on,* vol. 53, pp. 720-725, 2006.
[13] M. Lu, "Calculating the electric field in real human head by transcranial magnetic stimulation with shield plate," *J. Appl. Phys.*, vol. 105, p. 07B322, 2009.
[14] L. Hernandez-Garcia, T. Hall, L. Gomez, and E. Michielssen, "A numerically optimized active shield for improved transcranial magnetic stimulation targeting," *Brain Stimulation,* vol. 3, pp. 218-225, 2010.
[15] L. Gomez, L. Hernandez, A. Grbic, and E. Michielssen, "A simulation of focal brain stimulation using metamaterial lenses," in *Antennas and Propagation Society International Symposium (APSURSI), 2010 IEEE*, 2010, pp. 1-4.
[16] U. Herwig, F. Padberg, J. Unger, M. Spitzer, and C. Schönfeldt-Lecuona, "Transcranial magnetic stimulation in therapy studies: examination of the reliability of "standard" coil positioning by neuronavigation," *Biological Psychiatry,* vol. 50, pp. 58-61, 7/1/ 2001.
[17] A. T. Sack, R. C. Kadosh, T. Schuhmann, M. Moerel, V. Walsh, and R. Goebel, "Optimizing functional accuracy of TMS in cognitive studies: a comparison of methods," *Journal of Cognitive Neuroscience,* vol. 21, pp. 207-221, 2009.
[18] F. Salinas, J. Lancaster, and P. Fox, "3D modeling of the total electric field induced by transcranial magnetic stimulation using the boundary element method," *Physics in medicine and biology,* vol. 54, p. 3631, 2009.
[19] S. Diekhoff, K. Uludağ, R. Sparing, M. Tittgemeyer, M. Cavuşoğlu, D. Y. von Cramon, *et al.*, "Functional localization in the human brain: Gradient-echo, spin-echo, and arterial spin-labeling fMRI compared with neuronavigated TMS," *Human brain mapping,* vol. 32, pp. 341-357, 2011.
[20] A. Thielscher, A. Opitz, and M. Windhoff, "Impact of the gyral geometry on the electric field induced by transcranial magnetic stimulation," *Neuroimage,* vol. 54, pp. 234-243, 2011.
[21] Y. Zhu and A. C. Cangellaris, *Multigrid finite element methods for electromagnetic field modeling* vol. 28: John Wiley & Sons, 2006.
[22] G. H. Golub and C. F. Van Loan, *Matrix computations* vol. 3: JHU Press, 2012.
[23] R. H. Pletcher, D. A. Anderson, and J. C. Tannehill, *Computational fluid mechanics and heat transfer*: CRC Press, 2012.
[24] A. F. Peterson, "Analysis of heterogeneous electromagnetic scatterers: research progress of the past decade," *Proc. of the IEEE,* vol. 79, pp. 1431-1441, 1991.
[25] L. J. Gomez, L. Hernandez-Garcia, A. Grbic, and E. Michielssen, "Single-source multi-coil transcranial magnetic stimulators for deep and focused stimulation of the human brain," in *Radio Science Meeting (Joint with AP-S Symposium), 2013 USNC-URSI*, 2013, pp. 8-8.
[26] R. Jalinous, "Technical and Practical Aspects of Magnetic Nerve Stimulation," *Journal of Clinical Neurophysiology,* vol. 8, pp. 10-25, 1991.

[27] A. Barker, I. Freeston, R. Jalinous, P. Merton, and H. Morton, "Magnetic stimulation of the human brain," *J Physiol,* vol. 369, 1985.
[28] J. Ruohonen and R. Ilmoniemi, "Focusing and targeting of magnetic brain stimulation using multiple coils," *Medical and Biological Engineering and Computing,* vol. 36, pp. 297-301, 1998.
[29] S. L. Ho, X. Guizhi, W. N. Fu, Y. Qingxin, H. Huijuan, and Y. Weili, "Optimization of Array Magnetic Coil Design for Functional Magnetic Stimulation Based on Improved Genetic Algorithm," *Magnetics, IEEE Transactions on,* vol. 45, pp. 4849-4852, 2009.
[30] I. Chang-Hwan and L. Chany, "Computer-Aided Performance Evaluation of a Multichannel Transcranial Magnetic Stimulation System," *Magnetics, IEEE Transactions on,* vol. 42, pp. 3803-3808, 2006.
[31] B. H. Han, I. K. Chun, S. C. Lee, and S. Y. Lee, "Multichannel magnetic stimulation system design considering mutual couplings among the stimulation coils," *Biomedical Engineering, IEEE Transactions on,* vol. 51, pp. 812-817, 2004.
[32] S. S. Nagarajan, D. M. Durand, and E. N. Warman, "Effects of induced electric fields on finite neuronal structures: a simulation study," *Biomedical Engineering, IEEE Transactions on,* vol. 40, pp. 1175-1188, 1993.
[33] *MATLAB: Genetic Algorthm (GA) Toolbox (Version 7.10.0 (R2010a))*. Natick, Massachusetts: The MathWorks Inc. , 2010.
[34] D. Goldberg, *Genetic Algorithms in Search, Optimization, and Machine Learning*: Addison-Wesley Professional, 1989.
[35] A. T. Barker, "An introduction to the basic principles of magnetic nerve stimulation," *Journal of clinical neurophysiology: official publication of the American Electroencephalographic Society,* vol. 8, p. 26, 1991.
[36] G. Cerri, R. De Leo, F. Moglie, and A. Schiavoni, "An accurate 3-D model for magnetic stimulation of the brain cortex," *Journal of medical engineering & technology,* vol. 19, pp. 7-16, 1995.
[37] C. C. Paige and M. A. Saunders, "LSQR: An algorithm for sparse linear equations and sparse least squares," *ACM Transactions on Mathematical Software (TOMS),* vol. 8, pp. 43-71, 1982.
[38] S. Rush and D. A. Driscoll, "EEG electrode sensitivity-an application of reciprocity," *Biomedical Engineering, IEEE Transactions on,* pp. 15-22, 1969.
[39] A. Thielscher and T. Kammer, "Linking physics with physiology in TMS: a sphere field model to determine the cortical stimulation site in TMS," *Neuroimage,* vol. 17, pp. 1117-1130, 2002.
[40] K. Yunokuchi and D. Cohen, "Developing a more focal magnetic stimulator. Part II: Fabricating coils and measuring induced current distributions," *Journal of clinical neurophysiology : official publication of the American Electroencephalographic Society,* vol. 8, pp. 112-120, 1991.
[41] "Guideline for the clinical application, documentation and analysis of clinical studies for regional deep hyperthermia," *Strahlentherapie und Onkologie,* vol. 188, p. 198, 2012.
[42] H. Ford and J. M. Alexander, *Advanced mechanics of materials*: Longmans London, 1963.

[43] J. R. Davis and A. I. H. Committee, *Copper and Copper Alloys*: Asm International, 2001.
[44] F. S. Salinas, J. L. Lancaster, and P. T. Fox, "3D modeling of the total electric field induced by transcranial magnetic stimulation using the boundary element method," *Physics in Medicine and Biology,* pp. 3631-3647, 2009.
[45] A. Thielscher and T. Kammer, "Electric field properties of two commercial figure-8 coils in TMS: calculation of focality and efficiency," *Clinical Neurophysiology,* vol. 115, pp. 1697-1708, 2004.
[46] M. S. George, E. M. Wassermann, W. A. Williams, A. Callahan, T. A. Ketter, P. Basser, *et al.*, "Daily repetitive transcranial magnetic stimulation (rTMS) improves mood in depression," *NeuroReport,* vol. 6, pp. 1853-1856, // 1995.
[47] A. Pascual-Leone, B. Rubio, F. Pallardó, and M. D. Catalá, "Rapid-rate transcranial magnetic stimulation of left dorsolateral prefrontal cortex in drug-resistant depression," *Lancet,* vol. 348, pp. 233-237, // 1996.
[48] H. H. Jasper, "The ten twenty electrode system of the international federation," *Electroencephalography and clinical neurophysiology,* vol. 10, pp. 371-375, 1958.
[49] U. Herwig, P. Satrapi, and C. Schönfeldt-Lecuona, "Using the International 10-20 EEG System for Positioning of Transcranial Magnetic Stimulation," *Brain Topography,* vol. 16, pp. 95-99, 2003/12/01 2003.
[50] R. Sparing, D. Buelte, I. G. Meister, T. Pauš, and G. R. Fink, "Transcranial magnetic stimulation and the challenge of coil placement: A comparison of conventional and stereotaxic neuronavigational strategies," *Human Brain Mapping,* vol. 29, pp. 82-96, 2008.
[51] R. Ahdab, S. S. Ayache, P. Brugières, C. Goujon, and J. P. Lefaucheur, "Comparison of “standard” and “navigated” procedures of TMS coil positioning over motor, premotor and prefrontal targets in patients with chronic pain and depression," *Neurophysiologie Clinique/Clinical Neurophysiology,* vol. 40, pp. 27-36, 3// 2010.
[52] T. Kammer, M. Vorwerg, and B. Herrnberger, "Anisotropy in the visual cortex investigated by neuronavigated transcranial magnetic stimulation," *Neuroimage,* vol. 36, pp. 313-321, 2007.
[53] P. T. Fox, S. Narayana, N. Tandon, H. Sandoval, S. P. Fox, P. Kochunov, *et al.*, "Column-based model of electric field excitation of cerebral cortex," *Human Brain Mapping,* vol. 22, pp. 1-14, 2004.
[54] L. Richter, P. Trillenberg, A. Schweikard, and A. Schlaefer, "Stimulus intensity for hand held and robotic transcranial magnetic stimulation," *Brain Stimulation*.
[55] S. Knecht, J. Sommer, M. Deppe, and O. Steinsträter, "Scalp position and efficacy of transcranial magnetic stimulation," *Clinical neurophysiology,* vol. 116, pp. 1988-1993, 2005.
[56] N. Toschi, M. E. Keck, T. Welt, and M. Guerrisi, "Quantifying uncertainty in Transcranial Magnetic Stimulation-A high resolution simulation study in ICBM space," in *Engineering in Medicine and Biology Society (EMBC), 2012 Annual International Conference of the IEEE*, 2012, pp. 1218-1221.

[57] E. R. Sowell, B. S. Peterson, E. Kan, R. P. Woods, J. Yoshii, R. Bansal, *et al.*, "Sex differences in cortical thickness mapped in 176 healthy individuals between 7 and 87 years of age," *Cerebral Cortex*, vol. 17, pp. 1550-1560, 2007.

[58] J. Sommer, O. Steinstrater, C. Breitenstein, A. Jansen, C. Konrad, M. Deppe, *et al.*, "Interindividual variability in the cortex-to-scalp distance," *Neuroimage*, vol. 19, p. S47, 2003.

[59] M. G. Stokes, C. D. Chambers, I. C. Gould, T. R. Henderson, N. E. Janko, N. B. Allen, *et al.*, "Simple metric for scaling motor threshold based on scalp-cortex distance: application to studies using transcranial magnetic stimulation," *Journal of Neurophysiology*, vol. 94, pp. 4520-4527, 2005.

[60] S. Gabriel, R. Lau, and C. Gabriel, "The dielectric properties of biological tissues: II. Measurements in the frequency range 10 Hz to 20 GHz," *Physics in medicine and biology*, vol. 41, p. 2251, 1996.

[61] G. S. Fishman, *Monte Carlo: Concepts, algorithms, and applications*. Berlin, Germany: Springer-Verlag, 1995.

[62] H. Bagci, C. Yavuz, A. C. Yucel, J. S. Hesthaven, and E. Michielssen, "A fast and parallel stroud-based stochastic collocation method for statistical EMI/EMC analysis," in *Proc. IEEE Int. Symp. EMC*, Detroit, MI, 2008, pp. 1-5.

[63] H. Bagci, A. C. Yucel, J. S. Hesthaven, and E. Michielssen, "A fast Stroud-based collocation method for statistically characterizing EMI/EMC phenomena on complex platforms," *IEEE Trans. Electromagn. Compat.*, vol. 51, pp. 301-311, 2009.

[64] A. C. Yucel, H. Bagci, and E. Michielssen, "Fast probability density function estimation for statistical EMC/EMI characterization," presented at the USNC/URSI Nat. Radio Sci. Meet., Charleston, SC, 2009.

[65] A. C. Yucel, Y. Liu, H. Bagci, and E. Michielssen, "Statistical characterization of electromagnetic wave propagation in mine environments " *IEEE Antennas Wireless Propag. Lett.*, vol. 12, pp. 1602-1605, 2013.

[66] O. Bakir, A. C. Yucel, E. Michielssen, and H. Bagci, "Statistical characterization of wave propagation in mine environments," in *Proc IEEE AP-S. Int. Symp.*, 2012, pp. 1-2.

[67] O. Bakir, A. C. Yucel, H. Bagci, and E. Michielssen., "Stochastic characterization of wave propagation in mine environments," presented at the CNC-USNC/URSI National Radio Sci. Meet., Toronto, ON, 2010.

[68] A. C. M. Austin, N. Sood, J. Siu, and C. D. Sarris, "Application of polynomial chaos to quantify uncertainty in deterministic channel models," *IEEE Trans. Antennas Propag.*, 2013, to be published.

[69] J. S. Ochoa and A. C. Cangellaris, "Expedient electromagnetic analysis of the impact of statistical disorder in periodic waveguides," *IEEE Trans. Microw. Theory Techn.*, vol. 60, pp. 3919-3926, 2012.

[70] O. Aiouaz, D. Lautru, M.-F. Wong, E. Conil, A. Gati, J. Wiart, *et al.*, "Uncertainty analysis of the specific absorption rate induced in a phantom using a stochastic spectral collocation method," *Ann. Telecommun.*, vol. 60, pp. 409-418, 2011.

[71] D. Xiu, "Fast numerical methods for stochastic computations: A review," *Commun. Comput. Phys.*, vol. 5, pp. 242-272, 2009.

[72] J. Foo, X. Wan, and G. E. Karniadakis, "The multi-element probabilistic collocation method (ME-PCM): Error analysis and applications," *J. Comput. Phys.*, vol. 227, pp. 9572-9595, 2008.
[73] J. Foo and G. E. Karniadakis, "Multi-element probabilistic collocation method in high dimensions," *J. Comput. Phys.*, vol. 229, pp. 1536-1557, 2010.
[74] H. Rabitz, Ö. F. Alis, J. Shorter, and K. Shim, "Efficient input-output model representations," *Comput. Phys. Commun.*, vol. 117, pp. 11-20, 1999.
[75] X. Ma and N. Zabaras, "An adaptive high-dimensional stochastic model representation technique for the solution of stochastic partial differential equations," *J. Comput. Phys.*, vol. 229, pp. 3884-3915, 2010.
[76] A. C. Yucel, H. Bagci, and E. Michielssen, "Efficient stochastic EMC/EMI analysis using HDMR-generated surrogate models," in *Proc. XXXth URSI General Assembly and Sci. Symp.*, Istanbul, Turkey, 2011, pp. 1-4.
[77] A. C. Yucel and E. Michielssen, "GA-based electromagnetic optimization using HDMR-generated surrogate models," presented at the CNC-USNC/URSI Nat. Radio Sci. Meet., Spokane, WA, 2011.
[78] L. J. Gomez, A. C. Yucel, L. Hernandez-Garcia, S. F. Taylor, and E. Michielssen, "Sensitivity of TMS-induced electric fields to the uncertainty in coil placement and brain anatomy," in *Proc IEEE Int. Symp. Antennas Propagat.*, 2014, pp. 1-2.
[79] A. C. Yucel, "Uncertainty quantification for electromagnetic analysis via efficient collocation methods," Ph.D. dissertation, Univ. Michigan, Ann Arbor, MI, USA, , 2013.
[80] A. C. Yucel and E. Michielssen, "Efficient GA-based electromagnetic optimization using HDMR-generated surrogate models," presented at the Proc. IEEE Int. Symp. Antennas Propagat., 2012.
[81] A. C. Yucel, H. Bağcı, and E. Michielssen, "Stochastic electromagnetic analysis via high dimensional model representation," presented at the Proc. CNC-USNC/URSI National Radio Sci. Meet., 2010.
[82] L. J. Gomez, A. C. Yucel, L. Hernandez-Garcia, and E. Michielssen, "Uncertainty quantification in transcranial magnetic stimulation," presented at the Proc. CNC-USNC/URSI National Radio Sci. Meet., 2013.
[83] L. J. Gomez, A. C. Yucel, L. Hernandez-Garcia, S. F. Taylor, and E. Michielssen, "Uncertainty quantification in transcranial magnetic stimulation via high dimensional model representation," *IEEE Trans. Biomedical Engineering*, 2014 - early access.
[84] A. C. Yucel, H. Bagci, and E. Michielssen, "An adaptive multi-element probabilistic collocation method for statistical EMC/EMI characterization," *IEEE Trans. Electromagn. Compat.*, vol. 55, pp. 1154-1168, 2013.
[85] A. C. Yucel, H. Bagci, and E. Michielssen, "An h-adaptive stochastic collocation method for stochastic EMC/EMI analysis," in *Proc. IEEE Int. Symp. Antennas Propagat.*, 2010, pp. 1-4.
[86] J. Talairach and P. Tournoux, *Co-planar stereotaxic atlas of the human brain. 3-Dimensional proportional system: an approach to cerebral imaging*. Stuttgart: Geroge Thieme, 1988.
[87] S. Neggers, T. Langerak, D. Schutter, R. Mandl, N. Ramsey, P. Lemmens, *et al.*, "A stereotactic method for image-guided transcranial magnetic stimulation

validated with fMRI and motor-evoked potentials," *Neuroimage,* vol. 21, pp. 1805-1817, 2004.

[88] L. Gomez, F. Cajko, L. Hernandez-Garcia, A. Grbic, and E. Michielssen, "Numerical Analysis and Design of Single-Source Multi-Coil TMS for Deep and Focused Brain Stimulation," 2013.

[89] F. M. Cajko, E.; Gomez, L.; Martinsson, P.G.; Hernandez, L.; , "A Fast Direct Solver for Transcranial Magnetic Stimulation Analysis,," presented at the Antennas and Propagation Society International Symposium (APSURSI), 2010.

[90] F. M. Cajko, E.; Gomez, L.; Martinsson, P.G.; Hernandez, L.; , "A fast direct solver for TMS analysis and design in 3D," presented at the Antennas and Propagation Society International Symposium (APSURSI).

[91] T. Wagner, F. Fregni, U. Eden, C. Ramos-Estebanez, A. Grodzinsky, M. Zahn, *et al.*, "Transcranial magnetic stimulation and stroke: a computer-based human model study," *Neuroimage,* vol. 30, pp. 857-870, 2006.

[92] I. S. Duff and J. K. Reid, "The multifrontal solution of indefinite sparse symmetric linear," *ACM Transactions on Mathematical Software (TOMS),* vol. 9, pp. 302-325, 1983.

[93] W. Hackbusch, "A Sparse Matrix Arithmetic Based on\ Cal H-Matrices. Part I: Introduction to {\ Cal H}-Matrices," *Computing,* vol. 62, pp. 89-108, 1999.

[94] J. Xia, S. Chandrasekaran, M. Gu, and X. S. Li, "Superfast multifrontal method for large structured linear systems of equations," *SIAM Journal on Matrix Analysis and Applications,* vol. 31, pp. 1382-1411, 2009.

[95] S. Wang, M. V. de Hoop, and J. Xia, "On 3D modeling of seismic wave propagation via a structured parallel multifrontal direct Helmholtz solver," *Geophysical Prospecting,* vol. 59, pp. 857-873, 2011.

[96] P. G. Schmitz and L. Ying, "A fast direct solver for elliptic problems on Cartesian meshes in 3D," ed.

[97] L. Grasedyck, R. Kriemann, and S. Le Borne, "Domain decomposition based {\ mathcal H}-LU preconditioning," *Numerische Mathematik,* vol. 112, pp. 565-600, 2009.

[98] R. Plonsey and D. B. Heppner, "Considerations of quasi-stationarity in electrophysiological systems," *The Bulletin of mathematical biophysics,* vol. 29, pp. 657-664, 1967.

[99] N. Toschi, T. Welt, M. Guerrisi, and M. E. Keck, "A reconstruction of the conductive phenomena elicited by transcranial magnetic stimulation in heterogeneous brain tissue," *Physica Medica,* vol. 24, pp. 80-86, 2008.

[100] H. Cheng, Z. Gimbutas, P.-G. Martinsson, and V. Rokhlin, "On the compression of low rank matrices," *SIAM Journal on Scientific Computing,* vol. 26, pp. 1389-1404, 2005.

[101] S. Chandrasekaran, M. Gu, and T. Pals, "A fast ULV decomposition solver for hierarchically semiseparable representations," *SIAM Journal on Matrix Analysis and Applications,* vol. 28, pp. 603-622, 2006.

[102] M. Bebendorf and T. Fischer, "A Purely Algebraic Approach to Preconditioning Based on Hierarchical LU Factorizations," in *Numerical Mathematics and Advanced Applications*, ed: Springer, 2008, pp. 135-142.

[103] M. Bebendorf and J. Ostrowski, "Parallel hierarchical matrix preconditioners for the curl-curl operator," *J. Comput. Math,* vol. 27, pp. 624-641, 2009.
[104] P.-G. Martinsson, "A fast direct solver for a class of elliptic partial differential equations," *Journal of Scientific Computing,* vol. 38, pp. 316-330, 2009.
[105] S. Börm, "Approximation of solution operators of elliptic partial differential equations by {\ mathcal {H}}-and {\ mathcal {H}^ 2}-matrices," *Numerische Mathematik,* vol. 115, pp. 165-193, 2010.
[106] W. Hackbusch, B. N. Khoromskij, and R. Kriemann, "Hierarchical matrices based on a weak admissibility criterion," *Computing,* vol. 73, pp. 207-243, 2004.
[107] W. Hackbusch and S. Börm, "Data-sparse Approximation by Adaptive $\mathcal{H}2$-Matrices," *Computing,* vol. 69, pp. 1-35, 2002.
[108] M. Intel, "Intel Math Kernel Library," ed, 2007.
[109] B. J. Roth, L. G. Cohen, and M. Hallett, "The electric field induced during magnetic stimulation," *Electroencephalography and clinical neurophysiology. Supplement,* vol. 43, p. 268, 1991.
[110] P. R. Amestoy, I. S. Duff, and C. Vömel, "Task scheduling in an asynchronous distributed memory multifrontal solver," *SIAM Journal on Matrix Analysis and Applications,* vol. 26, pp. 544-565, 2004.
[111] D. H. Schaubert, D. R. Wilton, and A. W. Glisson, "A tetrahedral modeling method for electromagnetic scattering by arbitrarily shaped inhomogeneous dielectric bodies," *IEEE Trans. Antennas Propagat.,* vol. 32, pp. 77-85, 1984.
[112] B. C. Usner, K. Sertel, M. A. Carr, and J. L. Volakis, "Generalized volume-surface integral equation for modeling inhomogeneities within high contrast composite structures," *IEEE Trans. Antennas Propagat.,* vol. 54, pp. 68-75, 2006.
[113] L. J. Gomez and E. Michielssen, "A well-conditioned volume-surface field integral equation (VSCFIE) for inhomogeneous cylindrical scatterers with high-electrical contrasts," in *Radio Science Meeting (Joint with AP-S Symposium), 2013 USNC-URSI*, 2013, pp. 156-156.
[114] L. J. Gomez, A. C. Yucel, and E. Michielssen, "Low-frequency stable internally combined volume-surface integral equation for high-contrast scatterers," *IEEE Antennas Wireless Propag. Lett. (under review),* 2014.
[115] A. J. Poggio and E. K. Miller, "Integral equation solutions of three-dimensional scattering problems," *Computer techniques for electromagnetics,* pp. 159-264, 1973.
[116] C. Müller, *Foundations of the mathematical theory of electromagnetic waves*: Springer Berlin, 1969.
[117] P. Yla-Oijala and M. Taskinen, "Well-conditioned Muller formulation for electromagnetic scattering by dielectric objects," *IEEE Trans. Antennas Propagat.,* vol. 53, pp. 3316-3323, 2005.
[118] K. Cools, F. P. Andriulli, and E. Michielssen, "A Calderon Multiplicative Preconditioner for the PMCHWT Integral Equation," *IEEE Trans. Antennas Propagat.,* vol. 59, pp. 4579-4587, 2011.
[119] A. F. Peterson, S. L. Ray, R. Mittra, I. Antennas, and P. Society, *Computational Methods for Electromagnetics*: IEEE Press, 1998.

[120] S. Rao, D. Wilton, and A. Glisson, "Electromagnetic scattering by surfaces of arbitrary shape," *Antennas and Propagation, IEEE Transactions on,* vol. 30, pp. 409-418, 1982.
[121] D. Wilton, S. Rao, A. Glisson, D. Schaubert, O. Al-Bundak, and C. Butler, "Potential integrals for uniform and linear source distributions on polygonal and polyhedral domains," *Antennas and Propagation, IEEE Transactions on,* vol. 32, pp. 276-281, 1984.
[122] R. W. Freund, "A transpose-free quasi-minimal residual algorithm for non-Hermitian linear systems," *SIAM J. Sci. Comput.,* vol. 14, pp. 470-482, 1993.
[123] J. Jin, *The finite element method in electromagnetics*: John Wiley & Sons, 2014.
[124] M. F. Cátedra, R. P. Torres, J. Basterrechea, and E. Gago, *The CG-FFT method: Application of signal processing techniques to electromagnetics*: Artech House Boston, 1995.
[125] L. Hernandez-Garcia, V. Bhatia, K. Prem-Kumar, and M. Ulfarsson, "Magnetic resonance imaging of time-varying magnetic fields from therapeutic devices," *NMR in Biomedicine,* vol. 26, pp. 718-724, 2013.
[126] G. Vecchi, M. Sabbadini, R. Maggiora, and A. Siciliano, "Modelling of antenna radiation pattern of a re-entry vehicle in presence of plasma," in *in Proc. IEEE Int. Symp. Antennas Propag.*, 2004, pp. 181-184.
[127] M. Visintin, F. Vipiana, J. A. Tobon Vasquez, and G. Vecchi, "Reentry vehicles: evaluation of plasma effects on RF propagation," in *6th Int. Workshop on Tracking, Telemetry and Command Systems for Space Applications*, 2013.
[128] A. C. Yucel, L. J. Gomez, Y. Liu, H. Bağcı, and E. Michielssen, "A FMM-FFT accelerated hybrid volume surface integral equation solver for electromagnetic analysis of re-entry space vehicles," in *Proc CNC-USNC/URSI National Radio Sci. Meet.*, 2014.
[129] L. J. Gomez, A. C. Yucel, and E. Michielssen, "Well-conditioned volume surface combined field integral equation (VSCFIE) for inhomogeneous scatterers with negative permittivities," in *Proc CNC-USNC/URSI National Radio Sci. Meet.*, 2014.
[130] L. J. Gomez, A. C. Yucel, and E. Michielssen, "Volume-surface combined field integral equation for plasma scatterers," *IEEE Antennas Wireless Propag. Lett. (under review)*, 2014.
[131] Y. Liu and W. Chew, "Stability of surface integral equation for left-handed materials," *IET microwaves, Antennas & propag.*, vol. 1, pp. 84-88, 2007.
[132] G. Zouros and N. Budko, "Transverse Electric Scattering on Inhomogeneous Objects: Spectrum of Integral Operator and Preconditioning," *SIAM Journal on Scientific Computing*, vol. 34, pp. B226-B246, 2012.
[133] E. Bleszynski, M. Bleszynski, and T. Jaroszewicz, "AIM: Adaptive integral method for solving large-scale electromagnetic scattering and radiation problems," *Radio Science,* vol. 31, pp. 1225-1251, 1996.